Naval Research Laboratory
Washington, DC 20375-5320

NRL/7350/MR—2023/1

Estimating Surface Currents across Fronts Using Synthetic Aperture Radar

CHRISTOPHER WACKERMAN

Seafloor Sciences Branch
Ocean Sciences Division

July 7, 2023

REPORT DOCUMENTATION PAGE

Form Approved
OMB No. 0704-0188

1. REPORT DATE *(DD-MM-YYYY)*	**2. REPORT TYPE**	**3. DATES COVERED** *(From - To)*
07-07-2023	NRL Memorandum Report	01-04-2022 – 31-12-2022

4. TITLE AND SUBTITLE

Estimating Surface Currents Across Fronts Using Synthetic Aperture Radar

5a. CONTRACT NUMBER

5b. GRANT NUMBER

5c. PROGRAM ELEMENT NUMBER
0602435N

6. AUTHOR(S)

Christopher Wackerman

5d. PROJECT NUMBER

5e. TASK NUMBER

5f. WORK UNIT NUMBER
1M20

7. PERFORMING ORGANIZATION NAME(S) AND ADDRESS(ES)

Naval Research Laboratory
1005 Balch Blvd.
Stennis Space Center, MS 39529-5004

8. PERFORMING ORGANIZATION REPORT NUMBER

NRL/7350/MR--2023/1

9. SPONSORING / MONITORING AGENCY NAME(S) AND ADDRESS(ES)

Office of Naval Research
One Liberty Center
875 N. Randolph Street
Arlington, VA 22203-1995

10. SPONSOR / MONITOR'S ACRONYM(S)

ONR

11. SPONSOR / MONITOR'S REPORT NUMBER(S)

12. DISTRIBUTION / AVAILABILITY STATEMENT

DISTRIBUTION STATEMENT A: Approved for public release; distribution is unlimited.

13. SUPPLEMENTARY NOTES

14. ABSTRACT

Description of a forward model for predicting radar cross section modulations across a tidal current front consisting of published components for: (1) surface currents across a tidal current front; (2) solving the wave action balance equation to determine modulations in wave spectra across the front; and (3) generation of RCS from the modulated wave spectra. The model is applied to Synthetic Aperture Radar imagery collected during the ONR Mobile Bay experiment and compared to hydrodynamic model results provided by Woods Hole Oceanographic Institute.

15. SUBJECT TERMS

Synthetic aperture radar
Tidal current fronts
Radar cross section modulations

16. SECURITY CLASSIFICATION OF:			**17. LIMITATION OF ABSTRACT**	**18. NUMBER OF PAGES**	**19a. NAME OF RESPONSIBLE PERSON**
					Christopher Wackerman
a. REPORT	**b. ABSTRACT**	**c. THIS PAGE**	U	76	**19b. TELEPHONE NUMBER** *(include area code)*
U	U	U			(228) 688-5354

Standard Form 298 (Rev. 8-98)
Prescribed by ANSI Std. Z39.18

This page intentionally left blank.

Estimating Surface Currents Across Fronts Using Synthetic Aperture Radar

1.0 Summary

This report details the tools that were developed to estimate surface currents across a frontal signature in SAR imagery. Two main tools were developed. The first tool estimated radar cross section (RCS) from a two-dimensional wave height spectrum via a two-scale model that used the large-scale waves to generate slope variances and then used the short-scale waves to generate Bragg-scattering RCS that incorporated tilting of the small-scale facets by the large-scale waves (via the slope variances), modulation of the short-scale waves by the surface currents induced by the passage of the large-scale waves (the so-called hydrodynamic modulation), scattering from specular facets, and scattering from breaking waves. This tool is discussed in detail in Section 3. The second tool generates a spatial grid of wave height spectra for waves propagating across a current front via solution of the wave action balance differential equations using a ray-trace formulism. This tool is discussed in detail in Section 4. Given a surface current from a specified current front, the second tool generates a spatial grid of two-dimensional wave height spectrum and the first tool generates RCS values for each wave spectrum. This gives us a spatial plot of RCS across the current front that we can compare to the SAR image observations. We then change the surface current front parameters until the model and SAR image match.

The first tool was validated by comparing to published *in situ* observations of RCS from various experiments and to the CMOD6 model which is an empirical fit to large amounts of observational data and provides "ground truth" of RCS values across a full range of wind speeds, wind directions, and incidence angles (see Section 3). Figure S1 shows the *in situ* observations that were used for validation. All the observational data was taken at a 45 degree incidence angle, at VV polarization, a mixture of X- and C-band, and averaged over wind direction so that they become just a function of wind speed. The top plot shows the individual data sets and where they are from. The bottom plot shows the same data (all as blue dots) with a fit to the data (see Eq. (35)) shown as a black line with ±2.5 dB around this fit line that encompassing almost all of the data points. The red line is the CMOD6 result for a 45 degree incidence angle averaged over wind direction, and it lies almost on top of the data model and through the middle of the data points, indicating that at least for this data the CMOD6 model is a good surrogate for observational data. Figure S2 shows the validation results. The upper, left plot shows the model RCS (y-axis) compared to the CMOD6 results (x-axis). Root-mean-squared errors (RMSE) are shown for upwind, crosswind, and downwind RCS value in dB; the model can reproduce CMOD6 results for upwind / downwind with less than 1 dB RMSE, and crosswind with less than 2 dB over the full range of wind speeds, wind directions, and incidence angle. The bottom, left plot shows the two-scale model result for a 45 degree incidence angle averaged over wind direction (red line) compared to the data fit from Figure S-1 (black line) and the CMOD6 result (blue line). The two-scale model is a good match to the data and CMOD6 results, and well within the ±2.5dB lines. Finally, the upper, right plot compares the upwind / downwind asymmetry in the RCS value between CMOD6 (orange diamonds) and the two-scale model (blue dots). The mean values (~-0.5dB) are equivalent. Overall, the RCS model can reproduce the data observations and CMOD6 results to within 1-2 dB, and can generate the correct upwind/downwind ratio.

Manuscript approved July 5, 2023.

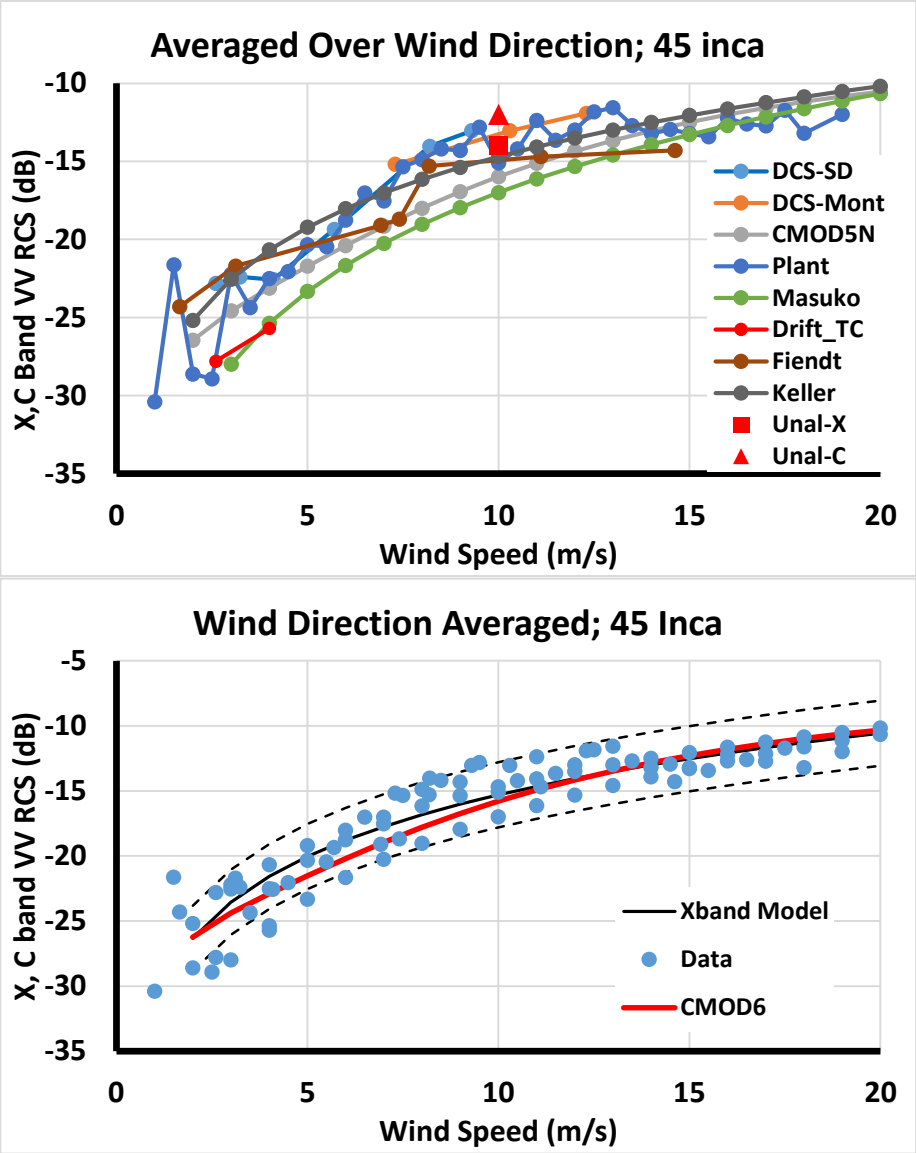

Figure S1: RCS data observations that were used to validate the tool for estimating RCS from two-dimensional wave height spectra. Top plot shows the RCS data from the range of sources. All the of data is for a 45 degree incidence angle, VV polarization, a mix of X- and C-band, and averaged over wind direction so that it is only a function of wind speed. Bottom plot shows the same data as blue dots, a model fit to the data (black line), and the CMOD6 model results for VV, 45 degree incidence angle, averaged over wind direction.

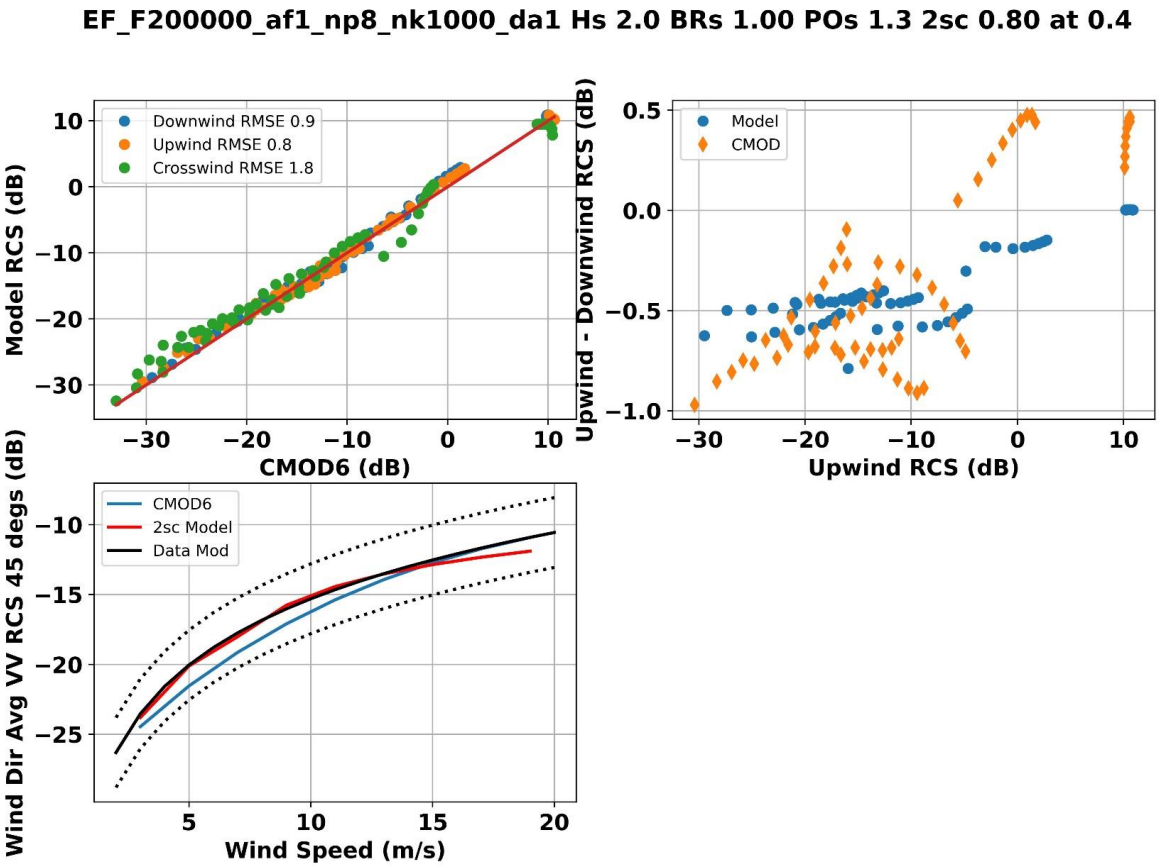

Figure S2: Validation results for the RCS model compared to CMOD6 and data observations. Upper, left plot compares model RCS values (y-axis) to CMOD6 values (x-axis). Root-mean-squared errors (RMSE) for the downwind, upwind, and crosswind RCS values are shown in the plot. Bottom, left plot compares model results (red line) to the data observations model in Figure S1 (black line) and the CMOD6 results (blue line) for 45 degree incidence angle, averaged over wind direction, VV polarization. Upper, right plot compares upwind/downwind ratio (in dB) between CMOD6 (orange diamonds) and the RCS model (blue dots) showing the same mean value (~-0.5 dB).

The second tool was validated by comparing to historical data of SAR observations of internal wave signatures (see Section 5). For these data the surface current was known and the SAR RCS modulations over that current field were archived. We generated a surface current field equivalent to the observations, ran the wave action balance equation solver to generate a spatial grid of wind-wave spectra across this current field, then ran the validated RCS model on each output wave spectrum to generate a plot of RCS modulations across the surface current. Figure S3 shows the resulting RCS model modulations for two sets of wave action balance equations (blue and orange lines) compared to the recorded range of RCS modulations over multiple SAR images (green dashed line). The model was able to generate RCS modulations right in the middle of the observed range using these combined tools.

Finally, we applied the tools to SAR imagery collected during the Mobile Bay, AL, experiment performed May-June 2021 (see Section 6 for details). We chose two images (collected on 09 June and 10 June 2021), generated cuts of RCS modulations across frontal features, then used the tools to find current front parameters that could reproduce the SAR image RCS modulations. Figure S4 shows the results for six cuts where the blue lines are the RCS model results and the orange lines are SAR image data (see Section 6 for details as to where the image cuts came from). Overall we were able to generate good comparisons in both peak modulation and width of the modulation function between the model and the data using current fronts that had a 0.10 – 0.20 m/s change across the front over a full-width distance of 50 – 100 meters. We compared this to surface current model results from David Ralston (WHOI) which showed a 0.10 – 0.20 m/s change across the fronts (so the range of our SAR-derived gradients and the WHOI model gradients are exactly the same) but had much larger frontal widths of 300 – 400 meters. However, Ralston's model was run with a very coarse resolution which most probably limited the size of the frontal width it could generate.

For three cases where we could reasonable relate the SAR image location to a model location, Figure S5 shows the WHOI model currents (solid black line is the u-velocity defined as the current orthogonal to the front orientation, solid red line is the v-velocity defined as the current along the front orientation) compared to the SAR-derived currents (black and red dashed lines). Since it is the current change across the front that determines the RCS modulation, for the bottom plot we added a bias of 0.20 m/s to the u-velocity. Our frontal current model assumes that the v-velocity is zero everywhere, so this is only a comparison to the u-velocity gradient (and a validation of our v-velocity assumption). For these cases the u-velocity gradient matches very well; generally within 0.05 m/s. Though as mentioned above, the frontal width is much smaller for the SAR-derived currents.

In summary, we have developed validated tools that allow us to determine the surface currents across a frontal signature in SAR imagery by finding the current parameters that generate RCS modulations consistent between the tools and the SAR image. The components of the tool have been individually validated, and the end-to-end tool has generated the same current gradients as a WHOI current model for the component orthogonal to the front. Thus we now have a tool that we could apply to other SAR images in regions where we have limited *in situ* observations to provide current gradient estimates across frontal signature that could constrain model parameters.

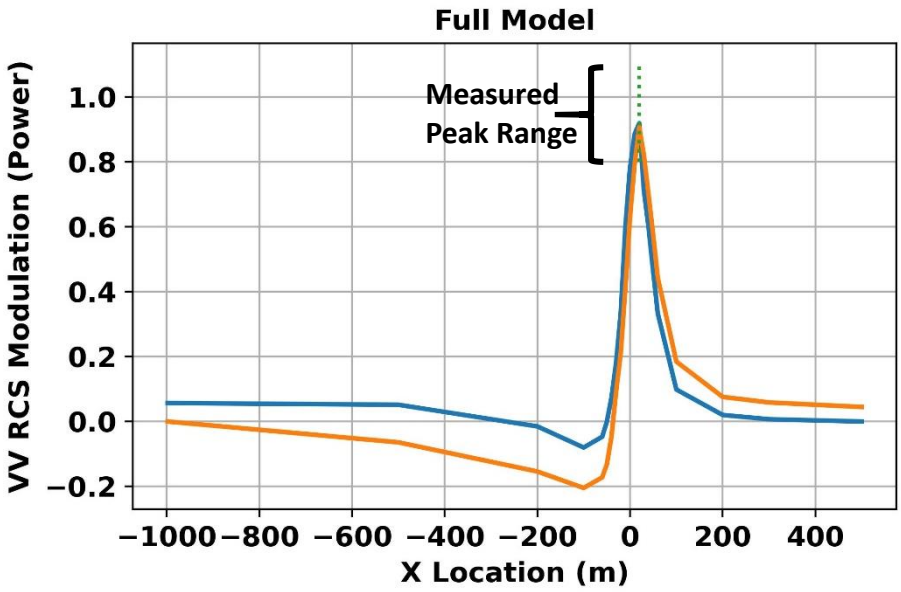

Figure S3: Validation of the wave action balance equation ray-trace solver. Historical internal wave signature data was used where SAR image RCS modulations were recorded over a known surface current field. Blue and orange lines are the RCS model results from having run the wave action balance equation solver over the surface current field to generate a spatial grid of wave spectra, then running the RCS model on the individual wave spectra to generate a spatial plot of RCS modulations across the surface current field. Green dashed lines are the archived RCS modulation peaks observed in the SAR imagery from multiple collections over the internal wave signature. RCS model generates the mean modulation value from the published data.

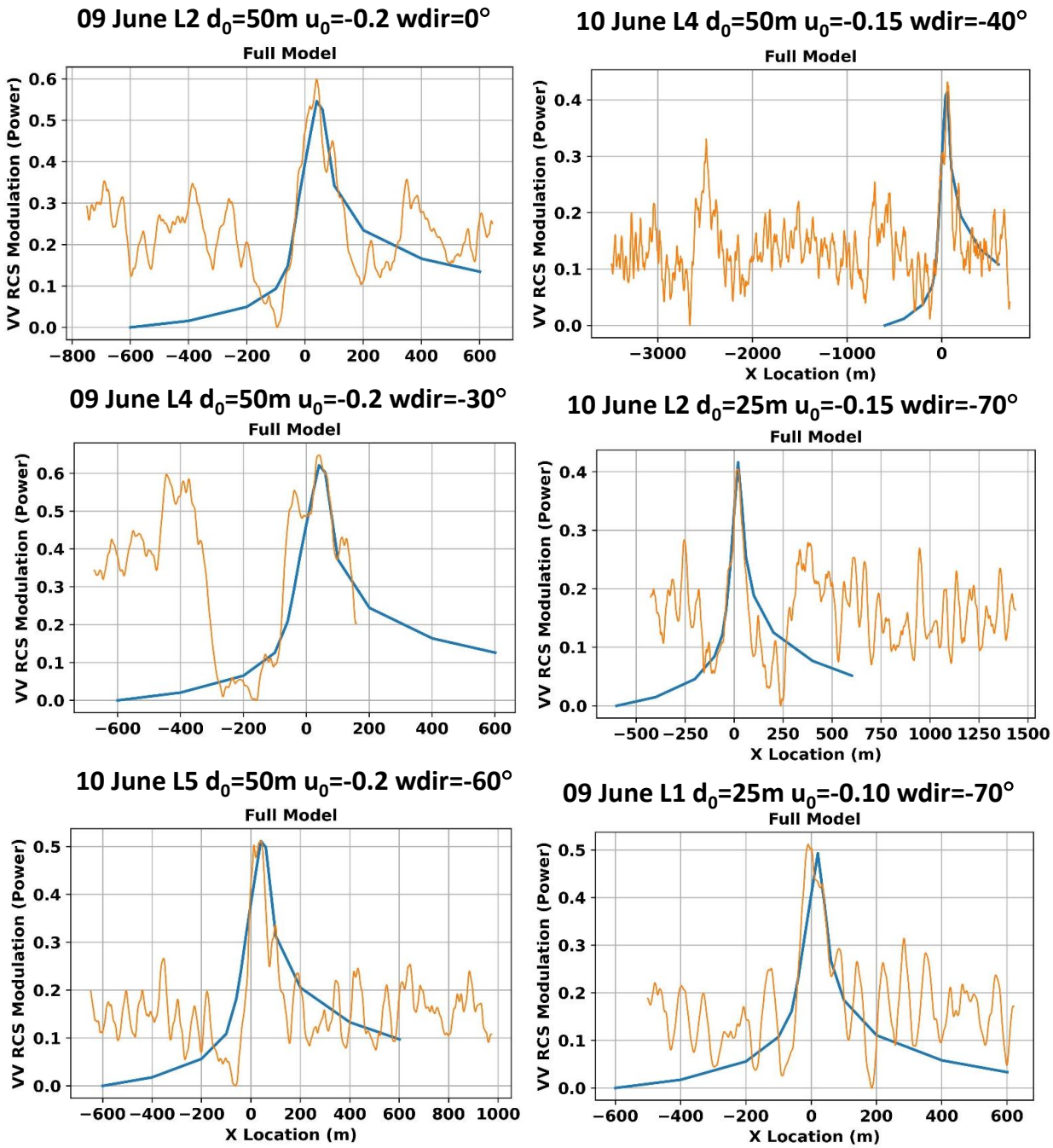

Figure S4: Comparison of model-generated RCS modulations (blue lines) to cuts from the SAR imagery (orange lines) for six different cuts. The current frontal parameters that generated the model result are indicated in the plot title. The image/location of the cut is also indicated in the title.

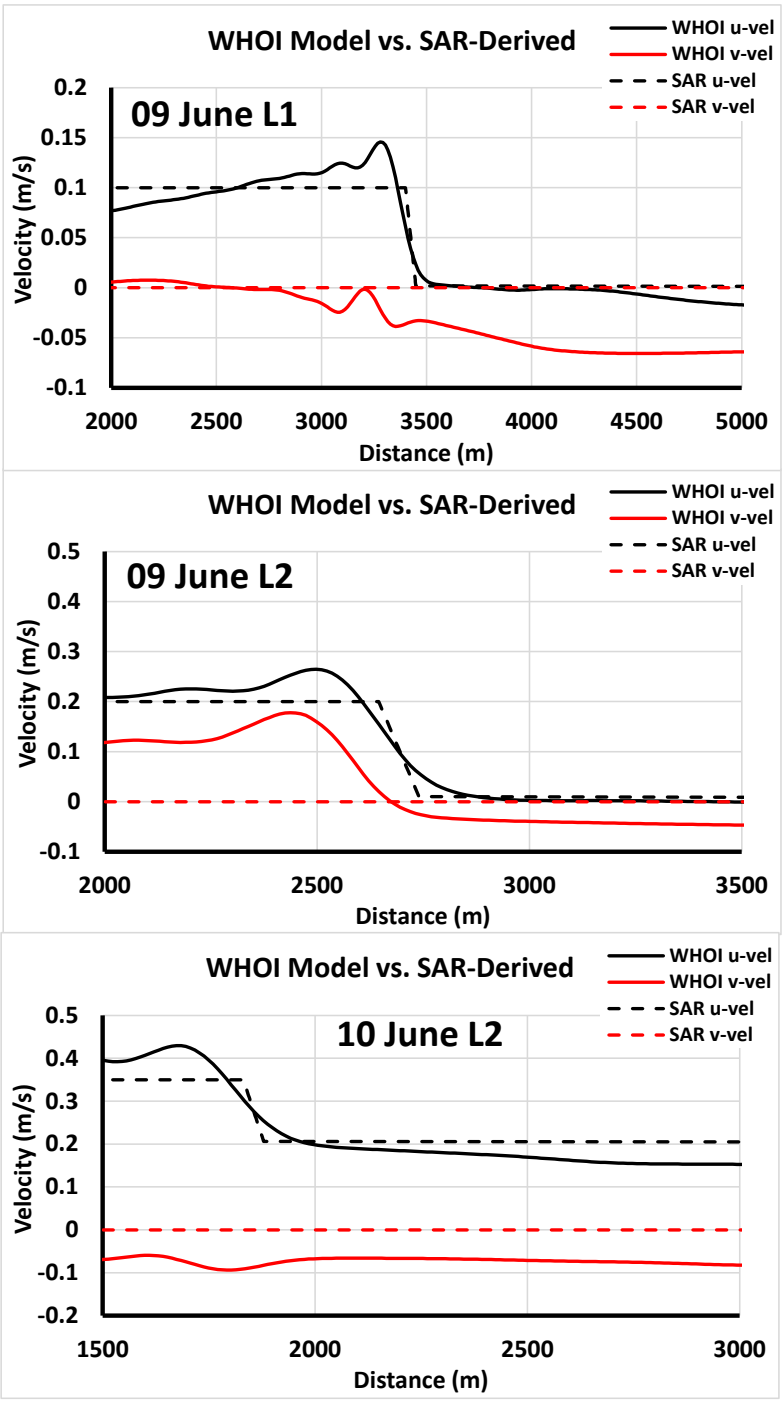

Figure S5: For three cases were we could reasonable match the SAR frontal signature to a model frontal signature, a comparison of the WHOI model currents (black and red solid lines) to the SAR-derived currents (black and red dashed line). The SAR current model has the v-velocity set to zero and is independent of a constant velocity bias, so this is a comparison of the u-velocity gradients. They agree to within 0.05 m/s.

2.0 Introduction

As part of the ONR UnderSea Remote Sensing (USRS) DRI satellite Synthetic Aperture Radar (SAR) imagery was collected during a subset of the experiments with the dual purpose of: (1) providing a global view of ocean surface features during the *in situ* experiments; and (2) to understand what satellite-based remote sensing can provide that would help generate full 3D+time model predictions for region where there are limited to no *in situ* data available. The latter study falls into two broad categories:

- What can SAR imagery provide as initial conditions for model runs, and is that sufficient to adequately constrain the models for useful predictions; and

- What can SAR imagery provide as "truth" within the space/time of the model outputs that could be used to tweak model parameters to provide more accurate predictions.

For the second category, ocean features that seemed promising to use for this were frontal signatures. Such signatures are readily observable in SAR imagery, and thus the satellite data can provide relatively accurate estimates of the spatial location of the front at a given date/time. Model prediction of frontal signature locations are driven mainly by wind and currents, so space/time offsets between model predictions and SAR estimates can be used to tweak wind/currents within the model run. In addition, if surface currents could be estimated from the SAR imagery, then current gradient strengths could be compared between the SAR and model results which could allow tweaking of water column properties to get them to match. This report summarizes the work on the development of an algorithm to estimate surface currents from the SAR imagery of frontal signatures.

One USRS experiment that was very successful in capturing frontal signatures in SAR imagery was conducted in Mobile Bay, AL during May-July of 2021. SAR data was collected daily over the course of the experiment, and during ebb tide conditions the imagery contained multiple signatures of fronts moving from the Bay out to sea. Figure 1 shows a typical example. This image was collected on 27 May 2021 at 23:47:04 GMT which was very close to mid-ebb tide. The two peninsulas that mark the end of the Bay can be seen in the upper portion of the image with the Bay at the top of the image and the Gulf of Mexico at the bottom. The bright or dark lines that can be seen throughout the image are mainly signatures across changes in the surface current from either (as indicated in the figure): (1) bottom sand waves that cause sinusoidal surface signatures; (2) current changes along the edges of the shipping channel; (3) outflow from deep cuts in the bathymetry along the southern shoals; and (4) tidal fronts propagating out of the Bay. Overall the image is rich in frontal signatures, and if each could be turned into a surface current estimate than we would have a spatially dense set of current gradients to compare to model estimates. The Mobile Bay experiment generated many such examples of SAR frontal signatures.

If we initially ignore motion effects, then SAR imagery can provide estimates of radar cross section (RCS) modulations across surface current fields. To model these modulations we had to develop two tools.

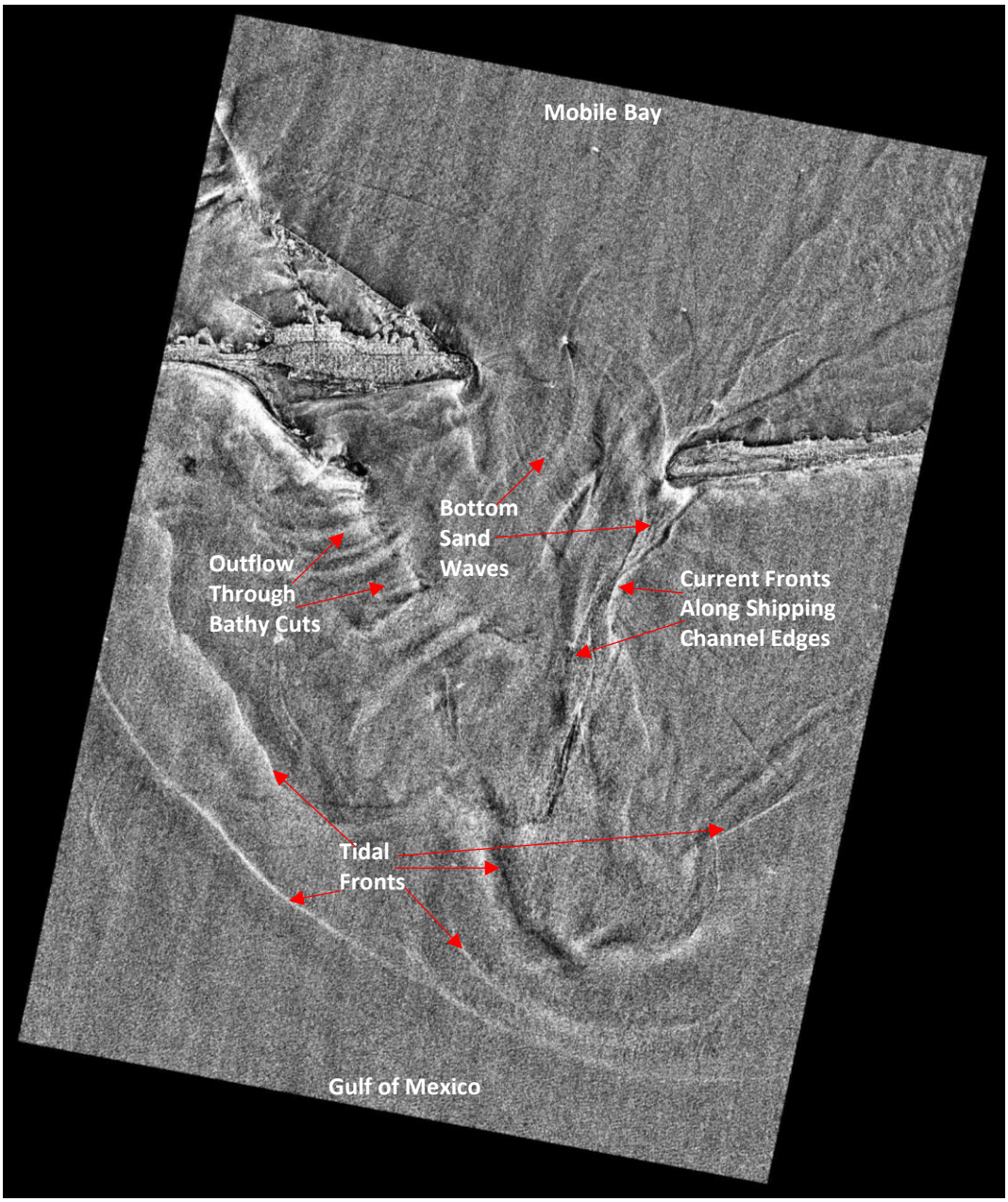

Figure 1: Example of a SAR image collected during the Mobile Bay, AL, 2021 ONR experiment. Image signatures of current fronts are indicated in the image. This image was collected on 27 May 2021 at 23:47:04 GMT. At the time of collection, we were in the middle of an ebb tide, the wind speed was 8.4 m/s, the wind direction was 193° from North, and the tide height was 0.13 m. The SAR look direction was 279° from North and the image was collected at an incidence angle of 19°. The image is in map coordinates with North up and East to the right.

(1) A tool to generate RCS from a two-dimensional wave height spectrum. This is discussed in Section 3 where we develop what is called a two-scale model to generate RCS which includes tilting, hydrodynamic, specular scattering, and breaking wave effects and validate it with in situ RCS observations..

(2) A tool to generate perturbed two-dimensional wave height spectra as the waves propagate through a changing surface current field (and potentially also a changing bathymetry). This is discussed in Section 4 where we develop a ray-trace solver for the wave action balance equation.

With these two tools in place, we can generate a proposed surface current field (with changing bathymetry if appropriate), run the second tool to generate a spatial grid of two-dimensional wave spectrum across the field, then run the first tool on each wave spectra to generate a RCS value. The final step will be a plot of RCS modulations across the current field.

In Section 5 we validate these tools by comparing to previous ONR experiments that collected data on internal waves. These are some of the few historical data where we have some combination of *in situ* surface currents and RCS data derived from SAR imagery. In Section 6 we apply these tools to two SAR images collected during the USRS Mobile Bay experiment for which we have model surface currents and make a comparison. Finally, Section 7 presents a discussion and next steps.

3.0 Estimating Radar Cross Section From Wave Spectra

This section describes the tool we developed to estimate radar cross section (RCS) from a two-dimensional wave spectrum. We first present some background on the history of this body of work, then we describe our specific implementation of the models. Finally, we validate the model by comparing to measured RCS data.

Background

The modeling of microwave radar cross section (RCS) modulations across a changing ocean surface current has been ongoing for decades, ever since it was observed that linear features can be observed in radar images over frontal signatures (Larson et al., 1976; Mattie et al., 1980; Hayes 1981; Vesecky and Stewart 1982; Fu and Holt 1983; Hasselmann et al., 1985; Alpers, 1985; Johannessen et al., 1991; Johannessen et al., 1996). Initially it was assumed that the RCS signature could be modelled as a change in small-scale surface roughness as the small-scale ocean surface waves interacted with the changing surface current. However it was realized early on that the RCS modulates due only to small-scale wave roughness changes were too small compared to observations, particularly at X-band, and so the modulations of the longer-waves had to be incorporated (Plant, 1986; Lyzenga and Bennett, 1988; Thompson 1988; Kasischke et al., 1988, Lyzenga, 1991, Romeiser et al., 1997; Plant, 2002; Wackerman et al., 2002). This was done by using a so-called two-scale model that divides the ocean surface into two scales; small facets that are the scale of the radar wavelength, and large-scale ocean surface waves. The RCS is modelled as small perturbation Bragg scattering so that the RCS is proportional to the amplitude of the small-scale ocean surface wave that is resonant with the radar electromagnetic wave. However the large-scale waves come into play in two ways: (1) as the large-scale waves

move pass the small-scale facets, they induce surface currents that modulate the amplitude of the small-scale waves; and (2) as the large-scale waves move pass the small-scale facets, they tilt the facets back-and-forth which changes the resonant wavelength and thus the amplitude of that wavelength. The scattering from tilted small-scale facets has been developed (Wright, 1968; Valenzuela, 1978) and the interaction of waves with surface currents is well modelled by assuming that wave action is conserved, which generates the wave action balance equation that can be solved to determine the changes in wave spectra due to current interactions (Phillips, 1984; Plant, 1986; Lyzenga and Bennet, 1988; Lyzenga, 1991; Lyzenga, 2004; Lyzenga, 2010) which are in all the standard wave models such as SWAN and WAM. These two components are then put together to form a final model for RCS from ocean waves in one of two general approaches:

(1) Generate an expression for RCS from tilted surfaces using either tilted Bragg scattering or approximations to the Kirchhoff integral and take derivatives of the expression with respect to large-scale surface slopes and currents (Thompson, 1988; Romeiser et al., 1997; Plant 2002). These approaches have the advantage that they can be continuous in scale (so one does not have to introduce an artificial cut-off between small- and large-scale waves) and can handle RCS modulations due to changes in currents and tilts analytically. However they tend to be computationally intensive.

(2) Calculate slope variance over a pre-defined large-scale range of waves, and under the assumption that wave slopes are Gaussian distributed with zero mean calculate the expected value of tilted Bragg scattering over all possible large-scale slopes (Lyzenga and Bennett, 1988; Wackerman et al., 2002; Lyzenga 2004). The hydrodynamic, or surface currents, effect is handled by modifying the Gaussian density by terms that convert the currents effects onto the correspond slopes of the long-scale waves. These approaches have the advantage of being computationally fast, but they do require an artificial division of wave lengths into two scales, and the hydrodynamic effects are approximated instead of analytically incorporated.

There has also been discussion that these approaches are still not sufficient under all circumstances, and that non-linear wave-wave interactions also have to be taken into account (Lyzenga, 2010). This is essentially incorporating the transfer of energy between wave spectral components, and dominantly the cascade of energy for low to high wavenumbers, when solving the wave action balance equation. So far we have not incorporated these effects into the model since the validations discussed in future sections show that we can achieve observed RCS modulations without this component.

Model for RCS from Wave Spectrum

We incorporated the latter general approach discussed above; the two-scale model that divides the ocean surface into Bragg waves and long-scale waves and incorporates tilting and hydrodynamic modulations of the Bragg waves. We will also add specular scattering and scattering from breaking waves. We will first discuss the two-scale model incorporating only tilt modulations, then add hydrodynamic modulations, then add the other components.

Incorporating Tilt Modulation

This standard two-scale model with tilt modulation can be represented as (Wright 1968; Romeiser et al., 1997)

$$\sigma_o = \int\int \sigma_b(s_u, s_c)\rho(s_u, s_c)ds_u ds_c \quad (1)$$

where s_u is the upwind slope of the facet, s_c is the crosswind slope, $\sigma_b(s_u,s_c)$ is the Bragg normalized radar cross section for a facet with slopes s_u and s_c, and $\rho(s_u,s_c)$ is the probability density function for the slopes which can be written as

$$\rho(s_u, s_c) = \frac{1}{\sqrt{2\pi\sigma_u^2\sigma_c^2}} \exp\left[-\frac{s_u^2}{2\langle s_u^2\rangle} - \frac{s_c^2}{2\langle s_c^2\rangle}\right] \quad (2)$$

where $\langle s_u^2\rangle$ and $\langle s_c^2\rangle$ are the variances of the upwind and crosswind slopes, respectively. These variances can be calculated from the ocean surface wave spectrum as

$$\langle s_u^2\rangle = \int_0^{2\pi}\int_0^{k_c} k^2 \cos^2(\phi - \phi_w)\Psi(k,\phi)kdkd\phi \quad (3)$$

And

$$\langle s_c^2\rangle = \int_0^{2\pi}\int_0^{k_c} k^2 \sin^2(\phi - \phi_w)\Psi(k,\phi)kdkd\phi \quad (4)$$

where $\Psi(k,\phi)$ is the wave spectrum in polar coordinates, ϕ_w is the direction that the wind is blowing toward, and (k,ϕ) are the polar coordinates of wavenumber and angle, respectively, in spectral space. The upper limit for the wavenumber integration, k_c, constrains the slope variances to come only from the long waves and not from the entire wave spectrum. This makes the variances consistent with the two-scale model. Typically, $k_c = k_e/3$ where k_e is the wavenumber of the SAR electromagnetic radiation defined as $(2\pi)/\lambda$ and λ is the SAR wavelength, although often the Bragg wavenumber (i.e. the wavenumber of the wave that is resonant with the radar wavelength for a flat ocean – $2*\sin(\theta_i)*kc$ where θ_i is the radar incidence angle) is used. Note however that the value for this cutoff is rather arbitrary, and this arbitrariness is the main disadvantage of the two-scale model. The wave spectrum in Eqs. (3) and (4) is the so-called one-sided spectrum defined so that

$$\eta(x,y) = \mathrm{RE}\left\{\int_{-\infty}^{\infty}\int_{-\infty}^{\infty} F_\eta(k_x,k_y)\exp[i(k_x x + k_y y)]dk_x dk_y\right\} \quad (5)$$

and

$$\Psi(k_x,k_y) = \left|F_\eta(k_x,k_y)\right|^2 \quad (6)$$

where RE{} is the real part of what is in the brackets, $\eta(x,y)$ represents wave height, $F_\eta(k_x,k_y)$ is the Fourier transform of the wave height, and (k_x,k_y) are the Cartesian coordinates in spectral space. The spectrum is normalized so that

$$\int\int \eta^2(x,y)dxdy = \int\int \Psi(k_x,k_y)dk_x dk_y. \quad (7)$$

The Bragg normalized radar cross section in Eq. (1) can be calculated as (Valenzuela, 1978; Romeiser et al., 1997)

$$\sigma_b(s_u,s_c) = |G(\theta_i)|^2 8\pi k_e^4 \cos^4(\theta_i)[\Psi(k_b,\phi_b) + \Psi(k_b,\phi_b + 180°)] \quad (8)$$

where θ_i is the local incidence angle for the facet with slopes s_u and s_c, $G(\theta_i)$ are the first-order scattering coefficients that depend on polarization and incidence angle (see, for example, Ulaby et al. (1982) for specifications of these coefficients), (k_b,ϕ_b) is the Bragg wave wavenumber and direction (i.e. the range direction) for the facet, and k_e is the wavenumber of the SAR electromagnetic radiation. The local incidence and Bragg wave spectral location can be represented as (Valenzuela, 1978; Romeiser et al., 1997)

$$\theta_i = \cos^{-1}\left[\cos\left(\theta_o + \tan^{-1}\{s_r\}\right)\cos\left(\tan^{-1}\{s_a\}\right)\right], \quad (9)$$

$$k_b = \frac{4\pi}{\lambda}\sqrt{\sin^2\left[\theta_o + \tan^{-1}\{s_r\}\right] + \cos^2\left[\theta_o + \tan^{-1}\{s_r\}\right]\sin^2\left[\tan^{-1}\{s_a\}\right]} \quad (10)$$

and

$$\phi_b = \phi_s + \tan^{-1}\left[\frac{\cos\left(\theta_o + \tan^{-1}\{s_r\}\right)\sin\left(\tan^{-1}\{s_a\}\right)}{\sin\left(\theta_o + \tan^{-1}\{s_r\}\right)}\right] \quad (11)$$

where θ_o is the reference incidence angle (i.e., the incidence angle for a flat sea), ϕ_s is the look direction of the SAR (in the same coordinate system as the wave spectrum is defined), s_r is the slope of the facet in the range direction, and s_a is the slope in the azimuth direction. The range and azimuth slopes can be calculated from the upwind and crosswind slope, s_u and s_c, as

$$s_r = s_u\cos(\phi_s - \phi_w + 180°) + s_c\sin(\phi_s - \phi_w + 180°) \quad (12)$$

and

$$s_a = -s_u\sin(\phi_s - \phi_w + 180°) + s_c\cos(\phi_s - \phi_w + 180°). \quad (13)$$

The conventions used for Eqs. (9) through (13) are that a positive slope in the range direction tilts the facet away from the SAR (i.e., increases the local incidence angle) and that a positive upwind slope means that we are on the back of the wave (i.e., the wave is propagating toward the

positive upwind direction). This means that when the SAR is looking into the wind (i.e., looking at the back of the wave) a positive upwind slope needs to be changed to a negative range slope. This is the reason for the 180 degrees offset in Eqs. (12) and (13).

To implement the standard model, we first chose a form for the two-dimensional wave spectrum, $\Psi(k,\phi)$ and use Eqs. (3) and (4) to calculate the upwind and crosswind slope variances. We then perform the integration in Eq. (1), where for each value of the upwind and crosswind slopes the probability density function is given by Eq. (2) and the Bragg backscatter term is calculated using Eqs. (8) through (13).

Incorporating Hydrodynamic Effects

The modulation of the Bragg wave amplitudes by the long-scale wave orbital velocities, often called the hydrodynamic effect, is usually modeled using a transfer function that changes the Fourier transform of the wave height into the Fourier transform of the hydrodynamic modulation. This transfer function is usually written as

$$\Delta h(x,y) = \mathrm{RE}\left\{ \int_{-\infty}^{\infty}\int_{-\infty}^{\infty} kM_h\left(k_x,k_y\right)F_\eta\left(k_x,k_y\right)\exp\left[-i\left(k_x x + k_y y\right)\right]dk_x\,dk_y \right\} \qquad (14)$$

where $\Delta h(x,y)$ is the normalized modulation of the Bragg backscatter (defined as $\Delta\sigma_b/\sigma_b$) at a given spatial location and $M_h(k_x,k_y)$ is the hydrodynamic transfer function. One standard analytical form for M_h is (Alpers et al., 1981; Monaldo and Lyzenga, 1986)

$$M_h\left(k_x,k_y\right) = 4.5\cos^2\left(\phi-\phi_s\right) \qquad (15)$$

which is derived by solving the wave action balance equation for the interaction of the Bragg waves with the long-wave currents assuming a k^{-4} fall-off for the wave spectrum near the Bragg spectral location and assuming the relaxation rate for the Bragg waves is zero. The wave spectra we will use will not exhibit a k^{-4} fall-off, so we will not use Eq. (15) directly, but we will utilize the analytical $\cos^2$ angular dependence. Many attempts have been made to measure the real aperture radar transfer function and in particular the hydrodynamic transfer function component. An empirical fit to a large body of observations that we will utilize in this paper is (Zurk and Plant, 1996)

$$M_h\left(k_x,k_y\right) = m_h\sqrt{\frac{g}{u\omega}}\left|\cos\left(\phi-\phi_s\right)\right| \qquad (16)$$

where u is wind speed, ω is wave frequency and m_h is a constant equal to 7.5 for VV-polarization and 12.6 for HH-polarization. Eq. (16) is actually considered to be a "residual" transfer function that includes all sources of modulation seen in the empirical data after the tilt modulation has been removed, particularly because the dependence on polarization is difficult to explain using only hydrodynamic modulation. The angular dependence in Eq. (16) is very uncertain. Theory would predict a dependence on the square of this term, as in Eq. (15), but the

empirical evidence is not sufficient to differentiate between a square term or the absolute value term that is in Eq. (16). The square-root term in Eq. (16) is a dimensionless variable which is close to one for the dominant wave and provides a wind speed dependence for M_h that is missing from Eq. (15).

Eq. (14) indicates that the spatial map of modulations due to hydrodynamic interactions can be generated by taking each spectral component of the wave height, scaling by the (potentially complex-valued) transfer function, and performing an inverse Fourier Transform. Since Eqs. (15) and (16) are real-valued, these forms imply that the peak of the hydrodynamic modulation is located at the peak of the wave height spectral component (since the phase of the wave height spectral component is not modified). There has been much discussion of this in the literature referenced above, and measurements of the phase of the hydrodynamic transfer function can vary significantly depending on a range of environmental parameters. To model this it is standard to include a phase term in the transfer function. If we include this phase term, and combine the theoretical angular dependence of Eq. (15) with the empirical wind speed dependence in Eq. (16), we generate the form that we will use in the model

$$M_h\left(k_x, k_y\right) = m_h e^{-i\phi_h} \sqrt{\frac{g}{u\omega}} \cos^2\left(\phi - \phi_s\right) \qquad (17)$$

where ϕ_h is the hydrodynamic modulation phase term that determines the offset between the wave peak and the modulation peak. A positive value for this phase term in Eq. (17) indicates a shift toward the forward face of the wave.

Eq. (14) generates a spatial map of the hydrodynamic modulation. In order to incorporate this effect into the two-scale model we need to form the average, over multiple long-wave wavelengths, of Eq. (14) over all (x,y) locations with the same upwind and crosswind slopes. If we specify this spatial average as $h(s_u,s_c)$, we can re-write the two-scale model in Eq. (1) as

$$\sigma_o = \int\int \sigma_b\left(s_u, s_c\right)\left[1 + h\left(s_u, s_c\right)\right]\rho\left(s_u, s_c\right) ds_u ds_c . \qquad (18)$$

It is important to note that $h(s_u,s_c)$ is not the value of the hydrodynamic modulation for a given upwind and crosswind slope, but rather the average of the modulation over all spatial locations with the specific upwind and crosswind slopes. Thus we are not attempting to recast Eq. (14) in terms of wave slopes, but rather we are realizing that for a given upwind and crosswind slope, the hydrodynamic modulation will in general take on a range of values. The average of this range will be $h(s_u,s_c)$.

Functional Form For $h(s_u,s_c)$

We now need to assume a functional form for the hydrodynamic scale function $h(s_u,s_c)$. We can get a sense for an appropriate form by calculating it directly from a simulation. If we assume an

analytical form for the wave spectrum, we can generate a realization of the ocean surface wave field by letting the Fourier phases be independent and uniformly distributed between $[0,2\pi]$ and by performing an inverse Fourier transform. From this surface simulation we can calculate the upwind and crosswind slopes at each spatial location and calculate $\Delta h(x,y)$ using Eq. (14). Finally, we can then calculate $h(s_u,s_c)$ from the simulated data by averaging $\Delta h(x,y)$ over the spatial locations with the same upwind and crosswind slopes. Because the simulations represent a given realization of the ocean surface, we average the resulting values of $h(s_u,s_c)$ with a small window in s_u,s_c space to decrease the point-by-point noise in the realization.

Figure 2 (taken from (Wackerman et al., 2002)) shows the result of this procedure when the SAR is looking at an angle of 45 degrees with respect to the wind and we have assumed a phase for M_h in Eq. (17) of 40 degrees. The top image in Figure 2 shows $h(s_u,s_c)$ as a function of upwind and crosswind slopes, and the bottom plots show cuts through $h(s_u,s_c)$ at $s_u = 0$ and $s_c = 0$ respectively. The bottom plot of Figure 2 shows that $h(s_u,s_c)$ is essentially linear with s_u and s_c. Similar results were generated for different SAR look angles and different assumed phases for M_h, all of which indicated that $h(s_u,s_c)$ is linear with respect to upwind and crosswind slopes. The orientation of the plane (defined as the direction of maximum slope) is the SAR look direction. The slope in that direction is dominated by the value of the M_h phase; larger phase values increase the slope.

Based on the simulation results, we will assume that $h(s_u,s_c)$ is a linear function of s_u and s_c. We can find the least-squared error coefficients for a linear expansion of $h(s_u,s_c)$ to generate

$$\sigma_o = \int\int \sigma_b(s_u,s_c)\left[1+\left(\frac{c_{uh}}{\langle s_u^2\rangle}\right)s_u+\left(\frac{c_{ch}}{\langle s_c^2\rangle}\right)s_c\right]\rho(s_u,s_c)\,ds_u\,ds_c \qquad (19)$$

where c_{uh} and c_{ch} are the correlation coefficients between the upwind and crosswind slopes and the hydrodynamic modulation, which can be calculated as

$$c_{uh} = \mathrm{RE}\left\{m_h e^{-i\phi_h}\int_{-\infty}^{\infty}\int_{-\infty}^{\infty} k^2\cos(\phi-\phi_w)\cos^2(\phi-\phi_s)\sqrt{\frac{g}{u\omega}}\Psi(k,\phi)k\,dk\,d\phi\right\} \qquad (20)$$

and

$$c_{ch} = \mathrm{RE}\left\{m_h e^{-i\phi_h}\int_{-\infty}^{\infty}\int_{-\infty}^{\infty} k^2\sin(\phi-\phi_w)\cos^2(\phi-\phi_s)\sqrt{\frac{g}{u\omega}}\Psi(k,\phi)k\,dk\,d\phi\right\}. \qquad (21)$$

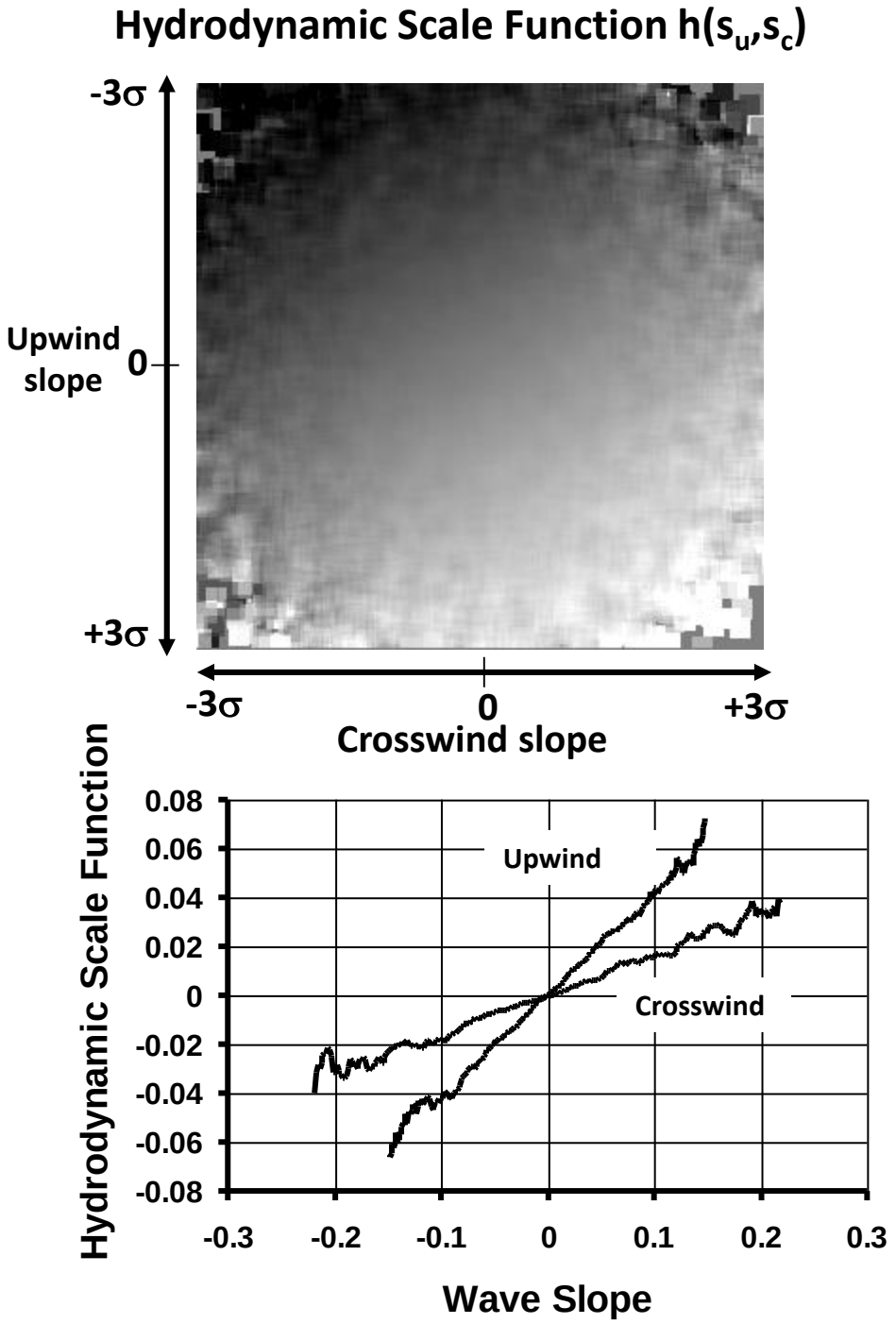

Figure 2: (Taken from (Wackerman et al., 2002)). Top image shows the mean hydrodynamic scale function as a function of upwind and crosswind slopes, averaged over simulated image samples with the same slope values. Bottom plot shows cuts through the top image at vertical and horizontal slices. Both results indicate that the function is approximately linear in slope.

Since the integrals in Eqs. (20) and (21) are real-valued, we can re-write these as

$$c_{uh} = [m_h \sin(-\phi_h)] \int_{-\infty}^{\infty}\int_{-\infty}^{\infty} k^2 \cos(\phi-\phi_w)\cos^2(\phi-\phi_s)\sqrt{\frac{g}{u\omega}}\Psi(k,\phi)kdkd\phi \qquad (22)$$

and

$$c_{ch} = [m_h \sin(-\phi_h)] \int_{-\infty}^{\infty}\int_{-\infty}^{\infty} k^2 \sin(\phi-\phi_w)\cos^2(\phi-\phi_s)\sqrt{\frac{g}{u\omega}}\Psi(k,\phi)kdkd\phi\,. \qquad (23)$$

Note that under our assumptions so far, if the phase of the hydrodynamic modulation transfer function, ϕ_h, is zero (i.e., the hydrodynamic modulation peaks at the same location as the wave height peaks), then $c_{uh} = c_{ch} = 0$ and there is no effect on the two-scale model from hydrodynamic modulations. This is because the function $h(s_u,s_c)$ is the average of the hydrodynamic modulation over locations with the same surface slopes, and if the transfer function phase is zero then there are equal magnitude positive and negative modulations at locations with the same slope, causing the average to be zero. As the phase term moves the hydrodynamic modulation peak off of the wave height peak, the locations of the positive/negative peaks move off of regions with the same slope, increasing the values of $h(s_u,s_c)$.

In general the upwind coefficient $c_{uh}/\langle s_u^2\rangle$ is much greater than the cross-wind coefficient $c_{ch}/\langle s_c^2\rangle$ so that the middle term in Eq. (19) which represents the hydrodynamic modulation effect can be written as $[1+a*s_u]$ where a is the imaginary part of the hydrodynamic modulation function. Note that this is what is done in (Lyzenga, 2010). In this form we can see the major impact of including this term is that it generates an upwind/downwind asymmetry in the output RCS values, which is seen in actual data, since the upwind ocean wave slopes, s_u, change sign as the radar switches from upwind to downwind. Without the hydrodynamic term, and thus with only the tilt term, the model would generate the same RCS values for upwind and downwind looks.

Physical Optics Approximation

The next component of the model will handle the specular scattering off ocean facets oriented orthogonal to the radar line of sight direction. For that situation Bragg scattering does not apply and one has to use the physical optics approximation (Lyzenga and Bennett, 1988)

$$\sigma_{po} = \frac{\pi|R(0)|^2}{\cos^4(\theta_o)}\rho(\tan(\theta_o)\cos(\Delta\Phi),\tan(\theta_o)\sin(\Delta\Phi))\exp\left[-4k_e^2\sigma_h^2\right] \qquad (24)$$

where R(0) is the complex-valued Fresnel reflection coefficient for an incidence angle of zero degrees, θ_o is the reference incidence angle (i.e., the incidence angle for the flat sea), ρ is the slope probability distribution function in Eq. (2) which is evaluated for a range slope of $\tan(\theta_o)$ and an azimuth slope of 0 (which represents the specular scattering situation), $\Delta\Phi$ is the angle

between the wind direction and the SAR look direction (which transforms range/azimuth slopes into upwind/crosswind slopes), k_e is the wavenumber of the electromagnetic radiation, and σ_h^2 is the variance of wave height calculated only over waves whose lengths are smaller than the size of the facet. The parameter σ_h^2 is a measure of the roughness of the water surface within the facet and is generated by integrating the wave spectrum over wavenumbers greater than k_c. The exponent at the end of Eq. (24) adjusts the specular response for the roughness of the facet. The physical optics approximation in Eq. (24) is added to the Bragg scattering model in Eq. (19)

Scattering From Breaking Waves

The final model component is scattering from breaking waves. Breaking water is much rougher on lengths scales of Bragg waves than non-breaking water, thus it generates a much higher RCS. It also has a significantly larger range of motions of the small-scale waves as they are formed from plunging water and/or slide down the front face of a spilling breaker. To model the RCS from breaking waves we will need to two components: a model for the RCS per unit area (often referred to as sigma-0) of breaking water, and a model to predict the spatial extent of breaking water, or what is often referred to as the breaking fraction, from the wave spectrum.

The RCS of breaking water has been measured in the surf zone at 44 and 59 degrees incidence for X-band VV (Haller and Lyzenga, 2003) and in wave tanks where stationary breaking waves are created at 45 degrees incidence for X-band VV and HH (Ericson et al., 1999). The stationary wave experiment also measure the small-scale surface spectrum of the breaking regions (Ericson et al., 1999) from which we could develop two models: (1) an empirical fit to an electro-magnetic scattering model from realizations of the small-scale surfaces (this will be referred to as Model 1); or (2) apply the two-scale model discussed above but using the spectra derived from the stationary breaking wave experiments (this will be referred to as Model 2). In addition, in (Kudryavtsev et al., 2003) they derive a parameter-based RCS breaking wave model from the physics of breaking waves following (Phillips,1988) and then empirically fit the parameters to observations, including (Ericson et al., 1999). All the observations and models have isotropic scattering for breaking waves such that it is independent of look angle and only depends on incidence angle. Figure 3 compares these models with the observational data. The red dots labelled "L&H" come from (Haller and Lyzenga, 2003) and represent the range of XVV RCS they measured at the two different incidence angles. The green dots labelled "E" are from (Ericson et al., 1999) and are the mean values for XVV (upper dot) and XHH (lower dot). The black line is the model from (Kudryavtsev et al., 2003). The top plot has Model 1 for the blue (XVV) and red (XHH) lines while the middle plot has Model 2 for the same lines. Around 45 degrees incidence angle, everything agrees to within approximately 4dB; though Haller & Lyzenga were less certain about these measurements than the ones at 59 degrees. The Haller & Lyzenga data appear pretty constant within 40 to 60 degrees incidence angles and both the Kudryavtsev model and the XVV Model 2 agree with that. The Kudryavtsev model goes right through the two Erickson data points, but that data was used to set the parameters so that is probably by construction. At smaller incidence angles Model 1 both XVV and XHH agree pretty well with the Kudryavtsev model but are much lower at larger incidence angles. In contrast, XVV Model 2 agrees with Kudryavtsev at the higher incidence angles but is way high at the lower ones. So overall, the Kudryavtsev model appears to be a good compromise between Model 1 and Model 2. However it agrees very well with the Ericson data but is around 3db

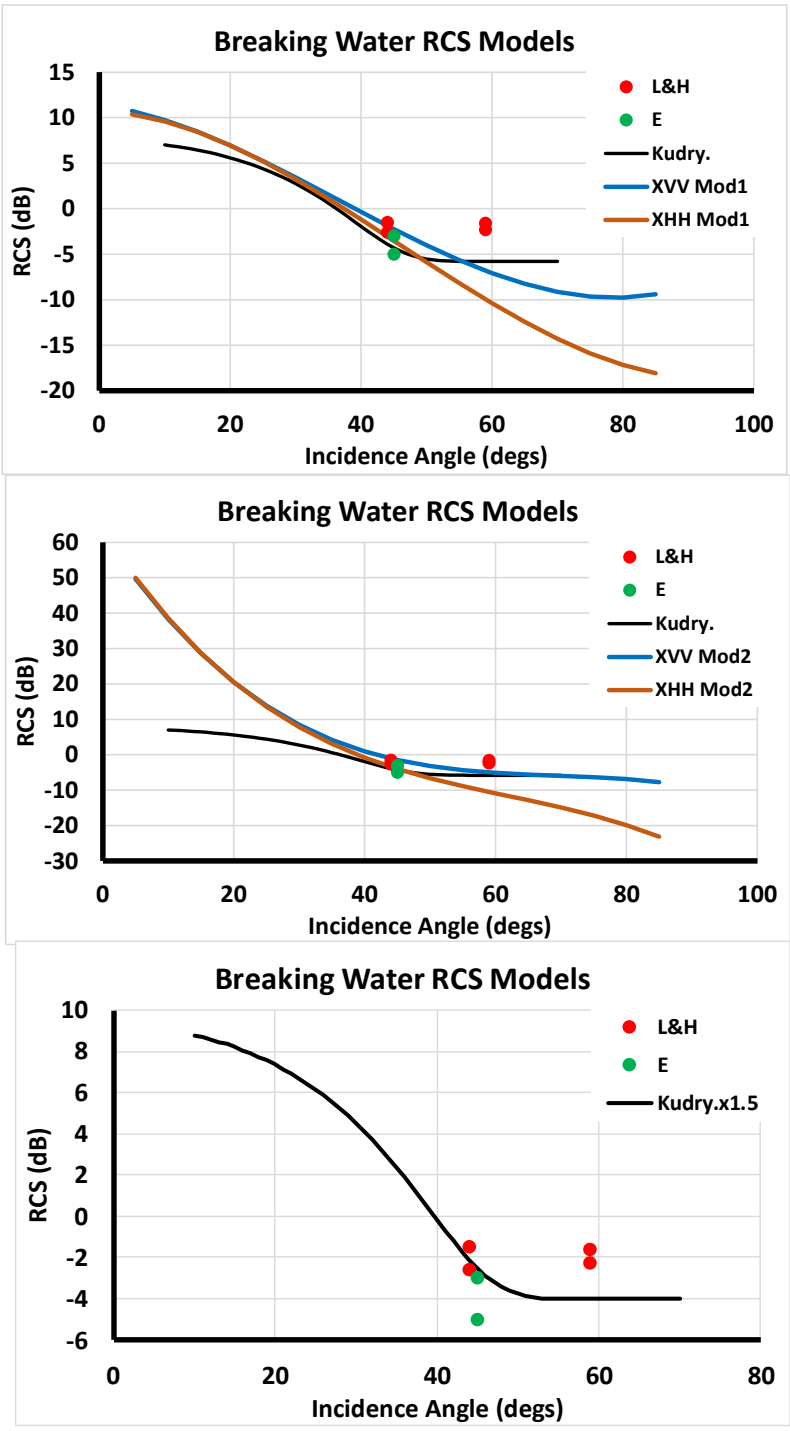

Figure 3: Comparison of different models for breaking water RCS. Green and red dots are published data from indicated sources. Black line is the model from Kudryavtsev et al., 2003; top and middle plot show the model, bottom plot shows the model scaled by 1.5. Blue and orange lines in the top plot are a model from an empirical fit to EM scattering from rough surfaces, and in middle plot are a two-scale model using surface wave spectra from experiments.

lower than the Haller & Lyzenga data. If we multiply the Kudryavtsev model by 1.5 (so a 1.8 dB shift in the plots) it agrees better with all the XVV data at 45 degrees; this is shown in the bottom plot in Figure 3 and represent the final model for breaking water RCS. Using Eq. (60) from (Kudryavtsev et al., 2003) with an additional scale factor gives:

$$\sigma_o^{br} = \left(\frac{\sec(\theta_i)^4}{s_{wb}^2}\exp\left[-\frac{\tan(\theta_i)^2}{s_{wb}^2}\right] + \frac{\varepsilon_{wb}}{s_{wb}^2}\right)\alpha_{wb} \quad (25)$$

where $s_{wb}^2 = 0.19$, $\varepsilon_{wb} = 0.005$ and $\alpha_{wb} = 1.5$.

To derive a model for the breaking fraction, i.e. the fraction of the ocean surface that is breaking, we can start from the derivatives in (Phillips, 1988) and (Kudryavtsev et al., 2003) that from a physics-based analysis the breaking fraction is proportional to the energy dissipated by breaking. (Philips, 1988) also shows that the breaking fraction should be proportional to the wind speed cubed. We then need a model for the energy dissipated by breaking. There are many of them in the literature, and the SWAN wave model has three separate ones one can chose between (see the SWAN Technical Documentation by the SWAN Team at Delft University of Technology, (SWAN Team, 2007)). Future work should examine a larger range of energy dissipation models, but for this analysis we used the pulse-based whitecapping model in SWAN (Komen et al., 1984)

$$E_D = \left(\frac{\tilde{w}}{\tilde{k}}\right)\iint \Gamma\, k\psi(k,\phi)\,dk\,d\phi \quad (26)$$

Where $\tilde{w}$ and $\tilde{k}$ are the mean frequency and wavenumber, respectively, defined as

$$\tilde{w} = \left(E_{TOT}^{-1}\iint \frac{1}{w}\psi(k,\phi)\,dk\,d\phi\right)^{-1} \quad (27)$$

$$\tilde{k} = \left(E_{TOT}^{-1}\iint \frac{1}{\sqrt{k}}\psi(k,\phi)\,dk\,d\phi\right)^{-2} \quad (28)$$

$$E_{TOT} = \iint \psi(k,\phi)\,dk\,d\phi \quad (29)$$

and $\Psi(k,\phi)$ is the two-dimensional wave height spectrum. Γ depends on overall wave steepness as:

$$\Gamma = C_{ds}\left((1-\delta) + \delta\frac{k}{\tilde{k}}\right)\left(\frac{s}{s_{PM}}\right)^p \quad (30)$$

Where

$$s = \tilde{k}\sqrt{E_{TOT}} \quad (31)$$

$s_{PM} = \text{sqrt}(3.02\text{x}10^{-3})$ and there are two possible sets of parameters for the other ones: $C_{ds} = 2.36\text{x}10^{-5}$, δ=0, p=4 or $C_{ds} = 4.10\text{x}10^{-5}$, δ=0.5, p=4. We use the first set in this analysis. We also implemented the SWAN saturation-based whitecapping model, but found that its results were essentially equivalent to the pulse-based model.

There is another approach we can use to estimate breaking fraction. We assuming that breaking results when the vertical acceleration of a piece of water below some negative threshold. That is, when the piece is water is dropping at a rate larger than the threshold. Assuming that the mean vertical acceleration over the entire wave height field is zero, we can calculate the variance of the vertical acceleration over the entire wave height field, σ_v^2, by integrating the wave spectrum multiplied by k^2w^4. We then make the assumption that the vertical acceleration is Gaussian distributed over the wave height field, so that the breaking fraction becomes the probability that a Gaussian random variable with zero mean and standard deviation σ_v is below the negative threshold. Typically this threshold is set to -0.4g, where g is the gravitational constant, based on an analysis of what rate of falling caused breaking water. We will use both of these models in the validations that follow.

Summary of Final Model

So the final model can be written as

$$\sigma_O = (T + s_H H) s_{Br} + s_{PO} PO + s_{wb} E_D \sigma_O^{br} \quad or$$
$$\sigma_O = (T + s_H H) s_{Br} + s_{PO} PO + P_G \sigma_O^{br} \tag{32}$$

where T is the contribution to the normalized radar cross section from the tilting of the long waves (this is equivalent to Eq. (1), but repeated here for convenience),

$$T = \iint \sigma_b(s_u, s_c)\rho(s_u, s_c)\, ds_u\, ds_c, \tag{33}$$

H is the contribution from the currents induced by the long waves,

$$H = \iint \sigma_b(s_u, s_c)\left[\frac{c_{uh}}{\sigma_u^2} s_u + \frac{c_{ch}}{\sigma_c^2} s_c\right]\rho(s_u, s_c)\, ds_u\, ds_c \tag{34}$$

PO is the physical optics approximation in Eq. (24), σ_O^{br} is the RCS from breaking in Eq. (25), E_D is the energy dissipated by breaking in Eq. (26) (if we use the SWAN energy dissipation model for breaking fraction), P_G is the probability of a Gaussian-distributed vertical acceleration being below some threshold (if we used the vertical acceleration model for breaking fraction) and we have scale factors for

(1) the hydrodynamic modulation, s_H, that is determined by the imaginary part of the hydrodynamic transfer function,

(2) the physical optics term that adjusts the small-scale roughness correction, s_{PO},

(3) to convert the energy dissipated by breaking into a breaking fraction, s_{wb}, if we use the SWAN energy dissipation model, and

(4) we have added one more scale factor, s_{Br}, which scales the Bragg spectral component that is used to calculate both the tilt and hydrodynamic terms. This is added because we will see below

that the various wave height spectra that we will use in this model have different scaling in the Bragg spectral regime so this will allow us to re-scale that regime to fit the radar cross section data.

Validation With Observed Data and Estimating Scalar Values

We will validate this RCS model by comparison to data collected in the field with *in situ* wind observations. First we need to determine what ocean wave spectrum model we will use in the RCS model. As is common we will assume that the ocean wave spectrum can be divided into a wavenumber term that only depends on wavenumber and an angular fall-off term that may depend on both angle and wavenumber, so that $\Psi(k,\phi)=S(k)F(k,\phi)$. To normalize the spectrum we will make the integration of the angular term over all angles equal to 1 for each wavenumber, so that the wavenumber term, S(k), can be used to calculate the variance of the ocean surface wave heights. We looked at five available wavenumber spectra.

(1) A spectrum developed by Pierson and Moskowitz (Pierson and Moskowitz, 1964) that is the grand-daddy of all the other models. This is a function only of wind speed and will be denoted by PM in the figures.
(2) The model developed by the Joint North Sea Wave Project (JONSWAP) (Hasselmann et al., 1973). This is a function of both wind speed and fetch, and will be denoted by JS.
(3) A model developed by Apel that was a modification of existing spectra to fit to RCS observations (Apel, 1994). This is only a function of wind speed and will be denoted by Apel.
(4) A model developed by Romeiser et al. that was a modification of spectra fit to RCS observations (Romeiser et al., 1997). This is only a function of wind speed and will be denoted by Rom.
(5) A model developed by Elfhouhailly et al. that was a re-calculation of the spectrum from first principles (Elfhouhailly et al., 1997). This is a function of both wind speed and fetch and will be denoted by Elf.

We also looked at four functional forms for the angular dependence $F(k,\phi)$.

(1) (cos[ϕ/2])**2n for a user input value of n. This is only a function of wave angle.
(2) A Gaussian function with a user input half-width. This is only a function of wave angle.
(3) A form developed in (Romeiser et al., 1997) that is a function of wavenumber, wave angle angle, and wind speed.
(4) A form developed in (Hauser and Caudal, 1996) that is a function of wavenumber, wave angle, and wind speed
(5) A form developed in (Elfhouhailly et al., 1997) that is also a function of wavenumber, wave angle, and wind speed.

For each of these spectrum angular models, as mentioned above in order to keep the final wave height spectrum scaled appropriately, we scale each function such that the integration over angle, for a given wavenumber, is always equal to one.

The Romeiser and Hauser-Caudal angular models are essentially equivalent, and the cosine and Gaussian functions can be made essentially equivalent, so we will be testing only three models: cosine, Romeiser, and Elfhouhailly.

Figure 4 shows the wave statistics that can be derived from the various spectra. The top set of four plots show the significant wave height from each spectrum as a function of wind speed for PM (upper, left), JS at different fetches (upper, right), Elf at different fetches (bottom, left) and the Apel and Rom models (bottom, right). Note that Elf gives much lower significant wave height versus the other models, with PM, Apel, Rom being similar and JS between these two. The bottom set of four plots in Figure 4 show the total slope variance derived from the spectra compared with the classic Cox & Munk model (Cox and Munk, 1954a; Cox and Munk 1954b) and a modification by (Wu, 1972; Wu, 1990). These results are more pertinent to the RCS model since the slope variance is what determines the tilt contribution to the RCS. Note that PM is much lower than the others, and that Elf is the highest, matches the models to about a 20 meters/second wind speed, and has a very small spread with respect to fetch (i.e. it does not significantly change with fetch). JS has a larger variation with fetch.

We will show below that when we derive a wave height field to correspond with *in situ* measured wave data we will need to have a wind-wave spectrum where we can change the significant wave height for a given wind speed. This means that we will need a spectrum model that has both wind speed and fetch as inputs so for a given wind speed we can change the fetch to make the significant wave height come out correct. Thus we are only really interested in the JS and Elf models, but we will show validation results for the Rom and Apel below to be complete.

All of these spectra models are essentially modifications of the original PM, which had a k^{-4} fall-off in the small-scale wave regime. Thus it is typical to show what is referred to as the saturation spectrum defined as $k^4*S(k)$. These are shown in top set of plots in Figure 5 for a wind speed of 10 meters/second. The PM model (upper, left) is flat, by construction, and we can see that the Apel and Rom models added a large peak in the very small wave length region. The JS model (upper, right) essentially keeps the flat PM portion whose height increases with decreasing fetch, but adds a peak in the long-scale waves whose location decreases with increasing fetch. The Elf model (lower, right) does not change that much with fetch (as we saw with the total slope variance plots), and the small-scale wave regime does not change at all with fetch. The Elf model also adds a large peak at the small wave length regime similar to Rom and Apel, but note that the peak is wider in the Elf models than in the Rom and Apel (this will be important when we compare against data below). The bottom set of plots in Figure 5 show the saturation spectra as a function of wind speed for a constant fetch of 200000 (for the JS and Elf models). Note that the PM model (upper, left) stays at the same height but just extends the low wavenumber cutoff as wind increases. The JS model is very similar, except the height changes slightly and it has the extra short-wavenumber peak. The Elf, Rom, and Apel models have a large peak in the small-scale wave regime (around the Bragg wave) that changes significantly with wind speed. This is important because it will cause a strong wind speed dependence on the RCS due to the Bragg scattering component. It is also these large peaks in the Bragg spectral regime that we will be scaling using the s_{Br} scale factor in the RCS model.

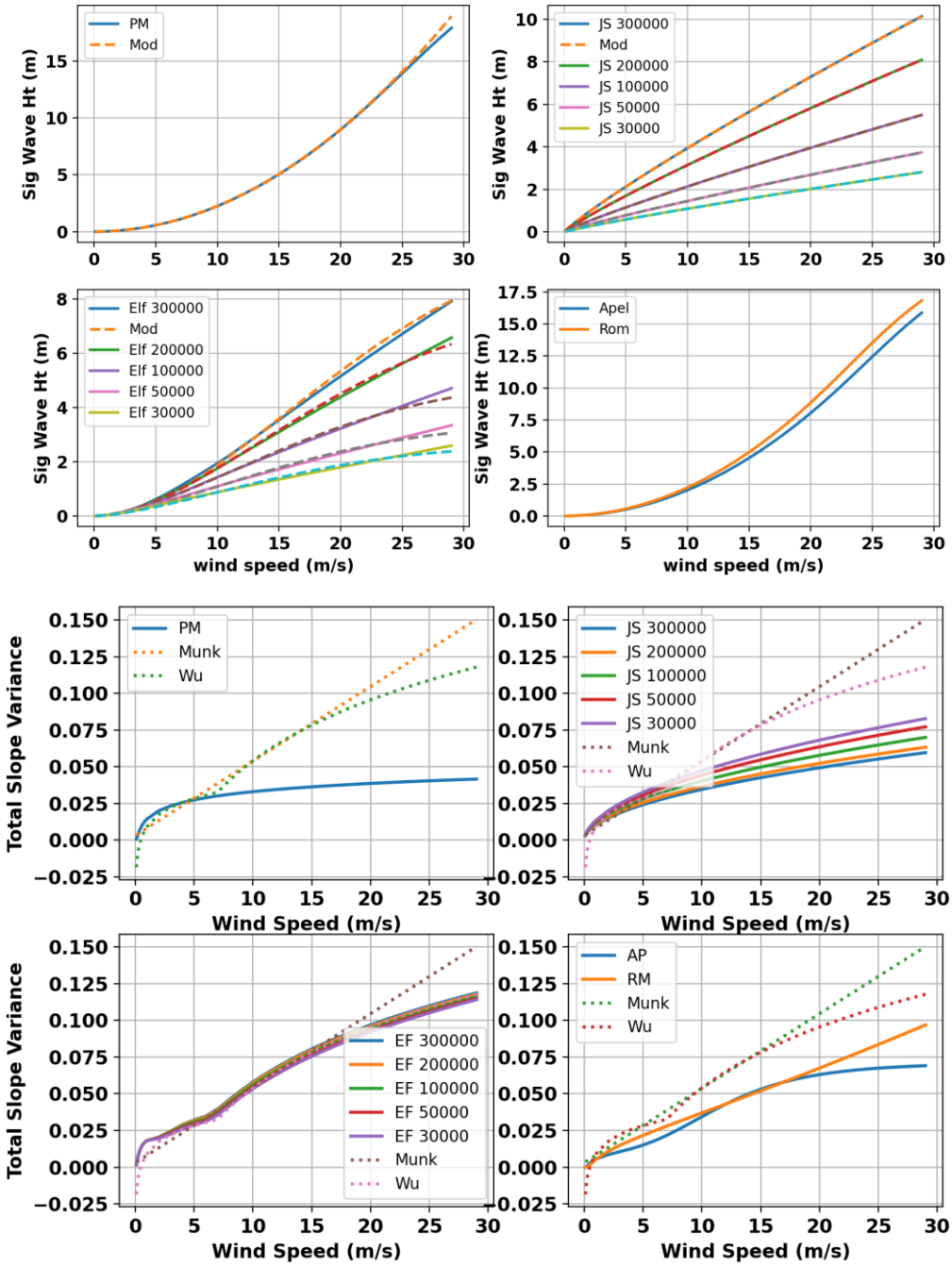

Figure 4: Spectral wave parameters (significant wave height (top) and total slope variance (bottom) derived from the various wind wave spectral models being considered in the text.

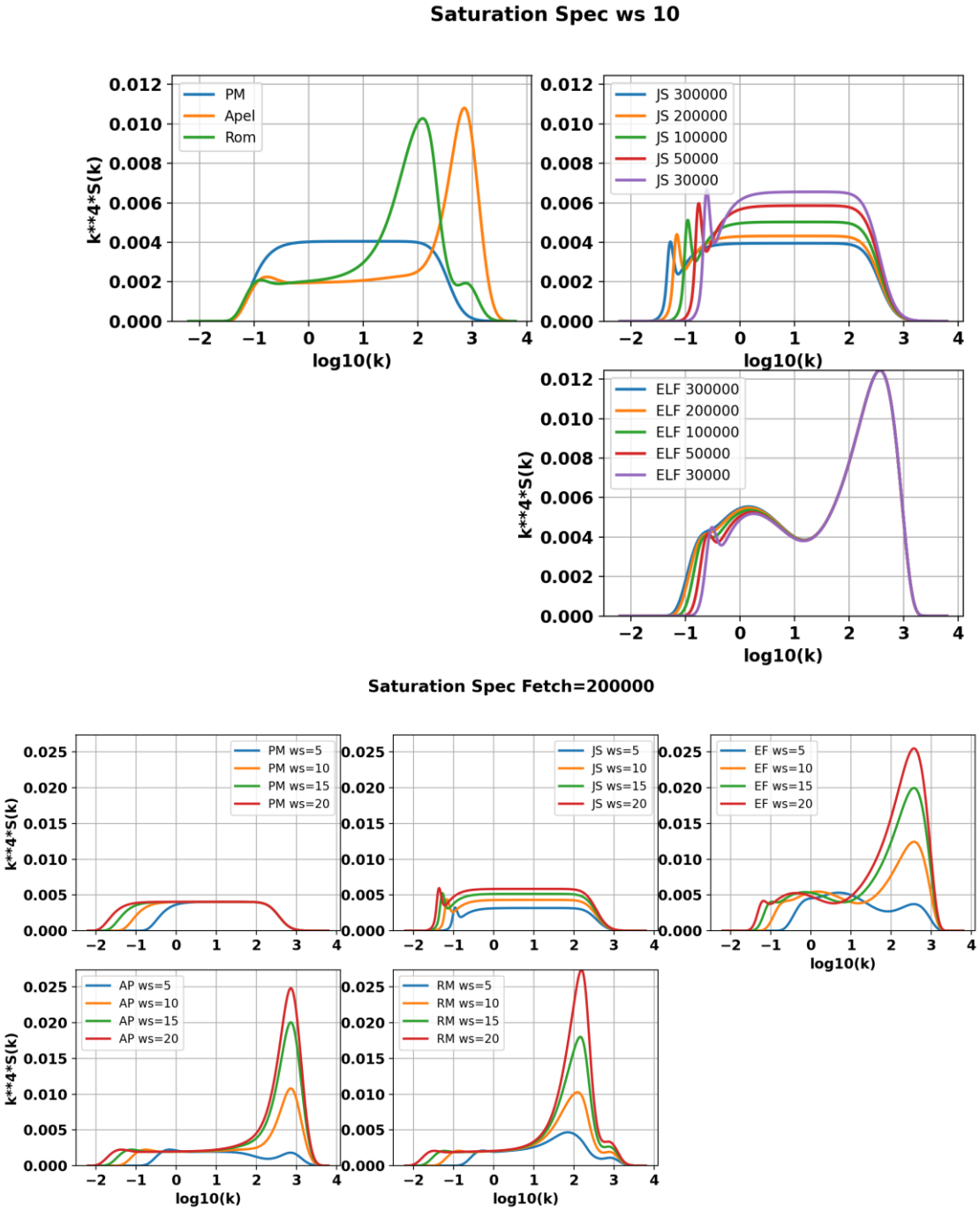

Figure 5: Saturation spectra for the various wind-wave spectral models being considered in the text. Top set of plots show the saturation spectra at a wind speed of 10 m/s for various fetch values (for the JONSWAP (JS) and Elfhoufailly (ELF) models). Bottom plots show the saturation spectra for different wind speeds (5, 10, 15, 20 m/s) for a constant fetch (200,000m) where appropriate.

Now we will evaluate the RCS two-scale model, with these various wind wave spectra models, compared against actual data. The data set that we could derive the most observational data for were for either X-band or C-band, collected at a 45 degrees incidence angle. We mixed X-band and C-band because they usually have very similar RCS values, and we will see that the variation between these bands is smaller than the variation between different data collections. The data were used were the following.

(1) Airborne scatterometer data collected at C-band (Fiendt et al., 1986).
(2) Airborne scatterometer data collected at X-band (Masuko et al., 1986).
(3) Tower-based scatterometer data collected at C-band (Keller et al., 1989).
(4) Airborne scatterometer data collected at C-band and X-band (Unal et al., 1991).
(5) Tower- and Bridge-based scatterometer data collected at X-band over a range of experiments by William Plant. Average RCS values over multiple experiments were generated and sent to me via personal communication.
(6) Airborne Synthetic Aperture Radar data where the sensor flew circle flights around a buoy measuring wind data at various incidence angles. The system was called the Digital Collection System (DCS) and collections were performed off the coast of San Diego (DCS-SD) and Monterey (DCS-Mont). This data was collected by my group in my previous, commercial, days and is part of that company's archive.
(7) CMOD5N and CMOD6. These are empirical fits to hundreds of thousands of C-band VV observations that are used as the standard model for the European satellite-SAR exploitation tools (Hersbach, 2003; Verhoef et al., 2008; Verspeek & Stofflen, 2015). CMOD6 is only a slight (0.5 dB) correction to CMOD5N so they are essentially equivalent. These are important because they are fit to actual data observations and they can provide "ground truth" RCS values for a large range of wind conditions, incidence angles, and look angles instead of being limited to the collection parameters of the other *in situ* data sets.

To combine all the data onto one plot, for each set of data we averaged over wind direction to generate VV RCS values (both X-band and C-band) at 45 degrees incidence angle as a function of wind speed. These data are shown in the top plot of Figure 6. There is about a 5dB scatter between all the different observations and the X-band and C-band appear inter-mixed. As is common, we lumped all the data observations (without the CMOD data) together and made a model fit of the form $RCS=Sw^p$ where w is wind speed in m/s. We perform the fit in dB space, so the final model becomes

$$RCS(dB) = 10*\log10(S)+p*10*\log10(w) = -31.05+1.575*(10*\log10(w)). \quad (35)$$

The bottom plot in Figure 6 shows all the data plotted together (blue dots) along with this model fit (black line) and ±2.5 dB around this fit line. Finally, the red line in the bottom plot are the CMOD6 results for an incidence angle of 45 degrees, averaged over wind direction, and plotted as a function of wind speed. Note that the CMOD6 model is essentially equivalent to the data fit. Also not that ±2.5dB around the model line includes almost all of the data observations.

Figure 7 shows the RCS model results compared to the data observations for the Elf spectrum model at large fetch (200,000 meters) and for out three of the angular models: the model in

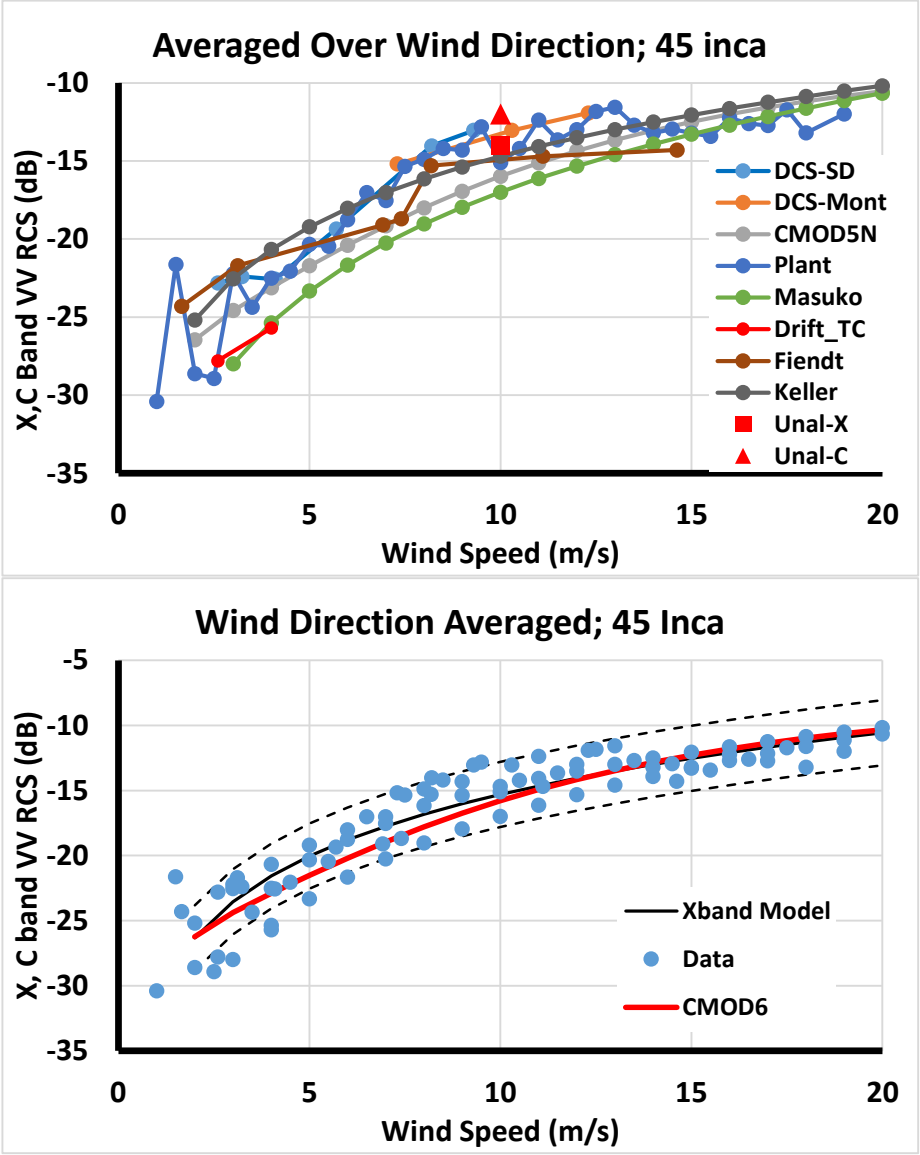

Figure 6: RCS data observations that were used to validate the tool for estimating RCS from two-dimensional wave height spectra. Top plot shows the RCS data from the range of sources. All the of data is for a 45 degree incidence angle, VV polarization, a mix of X- and C-band, and averaged over wind direction so that it is only a function of wind speed. Bottom plot shows the same data as blue dots, a model fit to the data (black line), and the CMOD6 model results for VV, 45 degree incidence angle, averaged over wind direction.

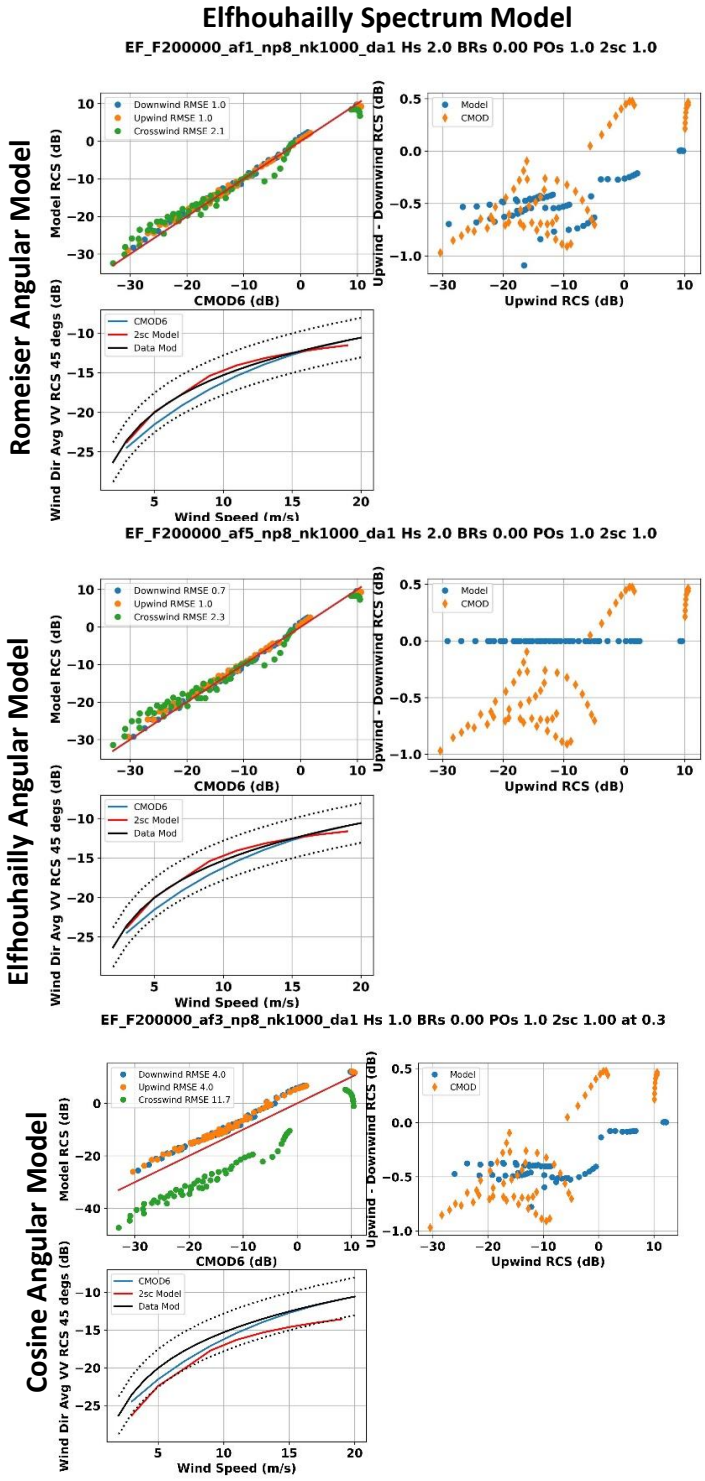

Figure 7: Comparison of RCS model to CMOD6 (upper, left in each set), observation data (lower, left in each set) and upwind/downwind ratio (upper, right in each set) for the Elfhouhailly wavenumber model with various angular models.

(Romeiser et al., 1997) (top plot); the model in (Elfhouhailly et al., 1997) (middle plot), and the cosine**2n model (bottom, plot). For these results we ran the RCS model with wind speeds from 3 to 19 meters/second every 2 meters/second, incidence angles from 10 to 70 degrees every 10 degrees, and look angles with respect to the wind direction of 0, 90, and 180 degrees. We used a breaking scale factor (s_{wb} in Eq. (32)) of 0.0 so there is no breaking water RCS in these results. We used a physical optics scale factor (s_{PO} in Eq. (32)) of 1.0 so there is no correction to the small-scale roughness coefficient. We did not scale the Bragg regime spectral values at all, so s_{BR} was set to 1.0. We used a fetch of 200,000 meters, so essentially infinite fetch.

For the hydrodynamic scale factor (s_H in Eq. (32)), as noted in (Wackerman et al., 2002) and mentioned above this component has very little impact on the final RCS values, but determines the ratio of upwind/downwind RCS. For these results we set the hydrodynamic scale factor to give the correct mean upwind/downwind ration for the Elf spectrum as discussed next.

For each spectrum model we show three plots. The upper, left is a cluster plot that compares the RCS model results for all wind speeds, incidence angles, and look angles to the corresponding RCS values from the CMOD6 model. The results root-mean-squared errors (RMSE) between the model and the CMOD6 RCS values for the downwind look (look angle = 0 degrees), crosswind look (look angle=90 degrees) and upwind look (look angle =180 degrees) are shown on the plot. Assuming that the CMOD6 results represent "ground truth" as discussed above, this is a measure of how good the model worked. The upper, right plot shows the upwind/downwind ratio (in dB so upwind(dB) – downwind(dB)) as a function of the upwind RCS for the model (blue dots) and CMOD6 (orange dots). This is a measure of how well the hydrodynamic term is capturing this ratio in that we want the model results to generally have the same mean as the CMOD6 results. We used this plot to manually set the hydrodynamic scale factor such that the model results went through the middle of the data results. Finally, the bottom, left plot in each set plots the wind direction averaged model result at 45 degrees incidence angle (red line, being the average of the 40 and 50 degrees data) to the CMOD6 result (blue line) and the data fit discussed above and shown in Figure 6 (black line with ±2.6 dB offsets). This is a measure of how well the model fits the data observations test set.

Figure 8 shows the same set of results, but for the JONSWAP wavenumber spectral model at large fetch (200,000 meters).

There are a number of conclusions we can draw from these results.

(1) the Elfhouhailly angular spectrum model does not work (see Figures 7 and 8, middle plots) – it never generates any upwind/downwind ratio by construction.
(2) The Elfhouhailly wavenumber spectrum model (Figure 7) is significantly better than the JONSWAP model (Figure 8), generating much lower RMSE values and a much tighter fit compared to the CMOD6 results.
(3) The cosine**2n angular model (Figures 7 and 8, bottom plots) does not work as well as the Romeiser et al. model (figures 7 and 8, top plots), particularly with the cross-wind results. This is not surprising since the Romeiser model has its wavenumber dependence on angular spread derived from RCS observations.

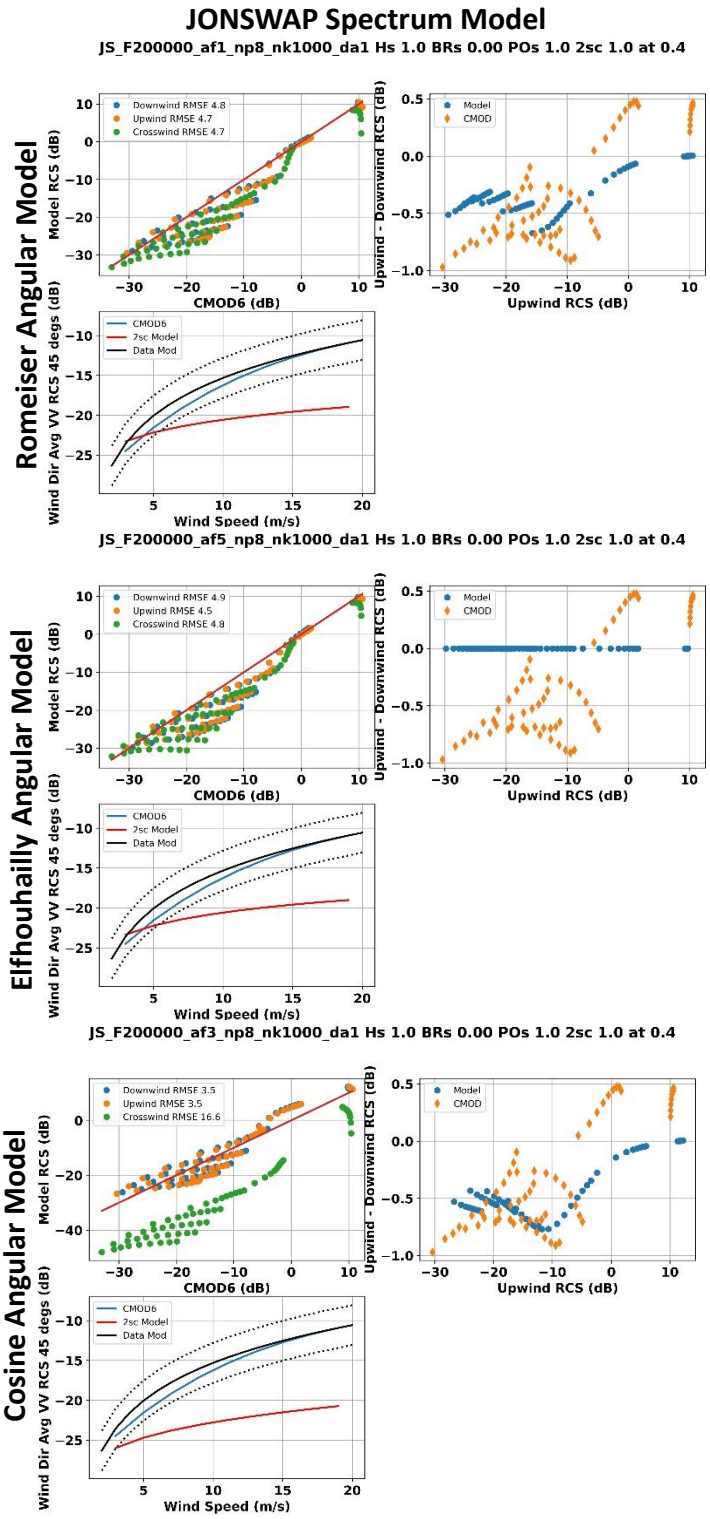

Figure 8: Same as Figure 7 but using the JONSWAP wavenumber model.

(4) The Elfhouhailly wavenumber spectral model with the Romeiser et al. angular spectrum function (top plot, Figure 7) is doing a very good job of reproducing the data observations. The RMSE values compared to CMOD6 for upwind/downwind geometries is 1dB, and for cross-wind is 2.1dB. The model results (red line) essentially lie on top of the data fit (black line) for the wind direction averaged 45 degree incidence angle data.
(5) For the Elfhouhailly spectrum model we need to set the hydrodynamic component scale factor, s_H, to 2 for the Romeiser et al. angular model and 1 for the cosine model in order to get the same mean upwind/crosswind ratio as predicted by CMOD6. For the JONSWAP spectrum model the scale factor is 1 for all angular models.

For completeness we also ran the RCS model for the Rom and Apel wavenumber spectral models. These results are shown in Figure 9 for Rom (upper plot) and Apel (bottom plot) spectral models using the Romeiser et al. angular model. Both of these generate RCS values that are generally too low compared to the Elf model, which is most probably due to the narrower width of the large small-scale peak in these models versus Elf (see Figure 5). Both of these could be adjusted to make better fits, but as mentioned above we will need a wind-wave spectral model that is a function of both wind speed and fetch, and these models are only a function of wind speed.

We now look at setting the other scale factors in the RCS model using the Elfhouhailly spectral model with the Romeiser et al. angular model. The only RCS values that are effected at all by the Physical Optics component of the model are the small group of the largest RCS values in the upper, right corner of the scatter plots. These are the RCS values that come from the smallest incidence angles, and thus are the only ones that have any specular scattering component. Note that they are separated from the main body of RCS values. Also note that it is interesting that the CMOD6 model also generates these larger RCS values for these smaller incidence angles, indicating that the data that went into forming CMOD6 included specular scattering at these incidence angles. Thus we can set the scale factor on the Physical Optics component, s_{PO}, by finding the value that makes this one group of large RCS points have a zero mean error for the upwind, downwind data points. This is achieved with a value of 1.3 (and actually is the same for all of the spectral models). For the Bragg regime scale factor, s_{Br}, we noted that for the Elf model (top plot, Figure 7) for RCS values less than about -15 dB the model RCS values are slightly too high. To give these values the correct mean we set s_{Br} to 0.8; note that this is essentially saying that the large spectral peak around the Bragg wave length is slightly too large.

Finally we have the breaking wave model. As mentioned above we have two possible models: one based on thresholding the vertical acceleration (we will refer to this as the V-Acc model) and one based on the SWAN pulse-based or saturation-based whitecaping (we will refer to this as the SWAN model). The parameters that we can adjust for each model are: (1) the threshold for the V-Acc model, which we will make a function of g so that the threshold is –Tg where T is typically set to 0.4; (2) scale factor, s_{wb}, to apply to the SWAN model to translate energy dissipation into breaking fraction (note that we just include this as the scale factor on the breaking RCS in Eq. (32) so that for the V-Acc model we need to set this to 1.0).

Figure 10 shows the final results for the model. The scale factors are set as described above. The left-column plots use the V-Acc breaking model and the right-column plots use the SWAN

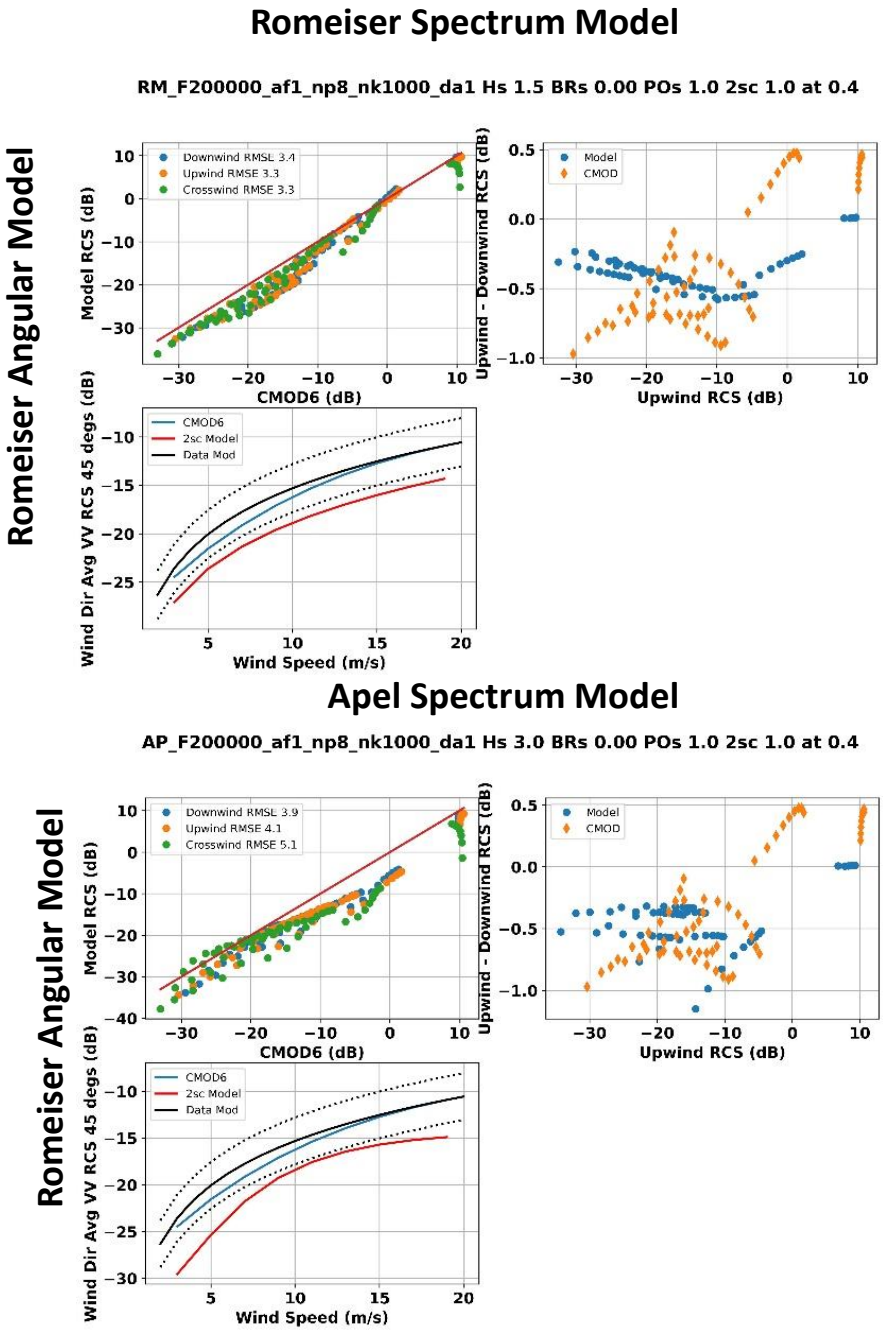

Figure 9: Validation results for the Romeiser wavenumber model (top set of plots) and the Apel wavenumber model (bottom set of plots) using the Romeiser angular model.

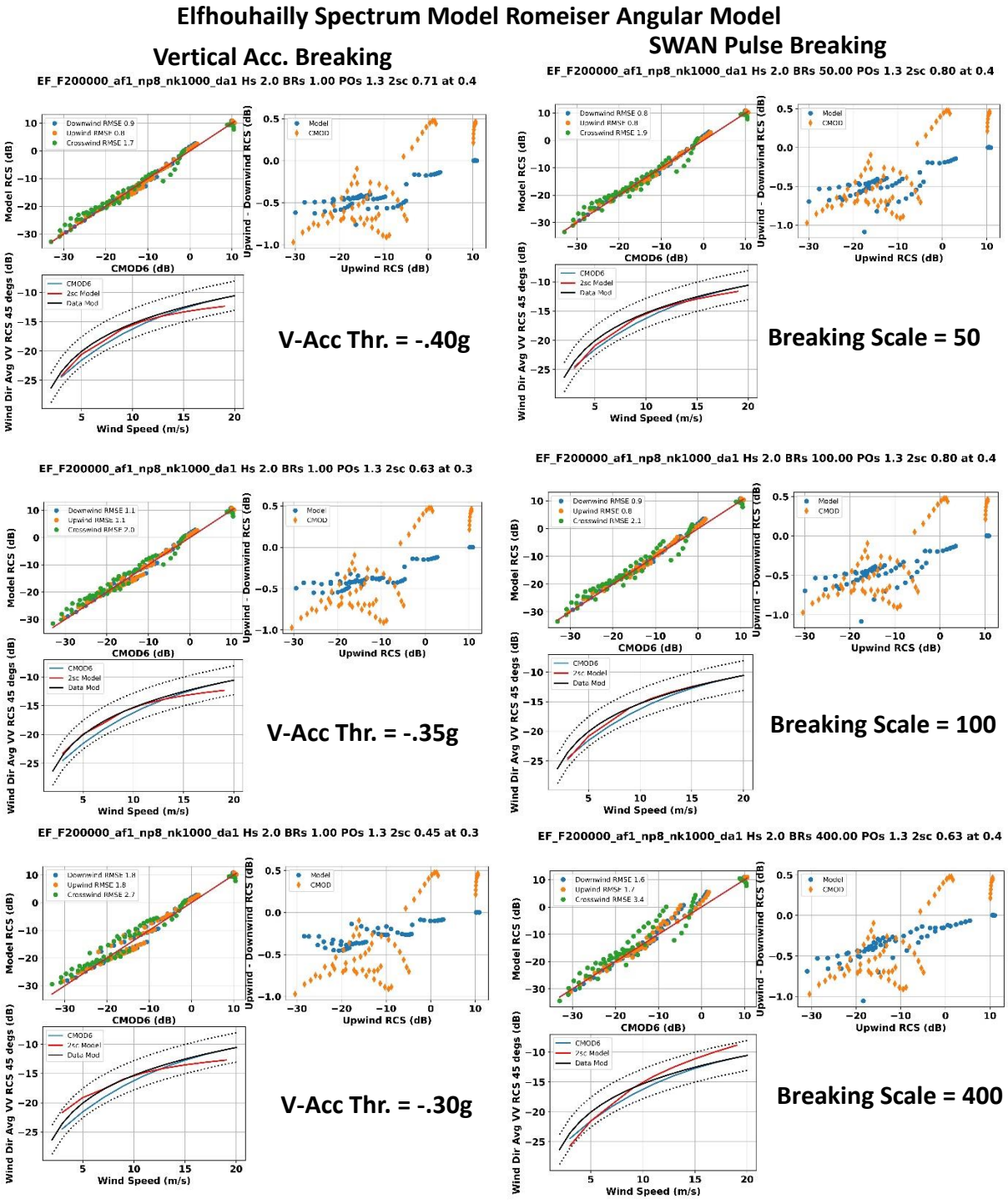

Figure 10: Final set of validation results using the vertical acceleration model (left column) and the SWAN model (right column) for breaking fraction. Lines are different breaking model parameters.

breaking model. The top sets of plots are for the "standard" models, where the threshold on vertical acceleration is set to -0.4g and the scale factor on the SWAN energy dissipation is set so that the model best matches the data fit (which turns out to be a scale factor of 50). However, this is not a very strong test for the breaking model (better tests will be discussed in the next two sections) since breaking is not effecting most of the RCS values that we are testing against. So we also looked at the range of breaking that we could still give results consistent with the validation data. The middle plots show a vertical acceleration threshold of -0.35g (left) and a SWAN scale of 100 (right). Both of these are essentially equivalent to the set above. The lower plots use a threshold of -3.0g (left) and a scale of 400 (right). At this range we are getting around a 2dB RMSE against CMOD6, but note that the model results is still within the noise range of the data model – though it hits the range at either end. So these last values set the end limit for the breaking fraction model.

There is one other validation test we can perform with these models by looking at predicted breaking fraction versus wind speed. For comparison, we can plot existing models for whitecapping versus wind speed that are in the literature. (Anguelova and Webster, 2006) has a nice summary of models that have been published. They all have the general form of Sw^p for some scale factor S and exponent p where w is wind speed in m/s. Generally p is around 3 (as noted above, in (Phillips, 1988) he shows that the physics indicates that breaking fraction should scale with wind raised to the 3rd power). However the models can vary significantly, and what is plotted in Figures 11 are two models at the low (orange line) and high (green line) ends of the model range. All the other models generally fall within these two. These are compared to the breaking fraction that our RCS model predicts (dots) for the V-Acc model (left-column) and the SWAN model (right-colum) using the three different sets of scale factors / thresholds from Figure 10. Both of the RCS models fall within the range of whitecapping models. The SWAN model increases faster than the V-Acc model. The range of results we showed in Figure 10 span from the low to high whitecap model for SWAN. For V-Acc, as we lower the threshold the breaking fraction increases, but not as fast as the SWAN model. Also note that the V-Acc model deviates from a wind to the 3rd power curve and essentially is a linear function of wind speed, whereas the SWAN model follows the 3rd power curves. Sections 4 and 5 will present some more stringent validation of the breaking fraction model.

In summary, our model for generating RCS values from a two-dimensional wave height spectrum using the Elfhouhailly et al. wavenumber model, the Romeiser et al. angular model, and scale factors of s_H=2.0, s_{PO}=1.3, s_{Br}=0.6-0.8, and either the V-Acc breaking model (with vertical acceleration threshold within [-0.3g, -0.4g]) or the SWAN breaking model (with s_{wb} in the range [50,400]), can generate RCS values that agree with the CMOD6 model to within approximately 1 dB for upwind/downwind geometries and 2 dB for crosswind geometries at the lower end of the breaking fraction parameters, and increases to 2 dB and 3 dB, respectively, as we increase the breaking fraction model. The model also agrees with the model derived from the collected set of *in situ* data observations at 45 degrees incidence angles, wind direction averaged, to within approximately ±0.5 dB for the lower breaking fractions and ±2dB at the higher end. It generates upwind/downwind ratios that agree with CMOD6 within approximately ±0.5 dB for all breaking fraction parameters. It generates a breaking fraction model versus wind speed that is consistent with the low and high published models for whitecapping, though the SWAN model obeys the wind speed to the 3rd power law whereas the V-Acc model is linear with wind speed.

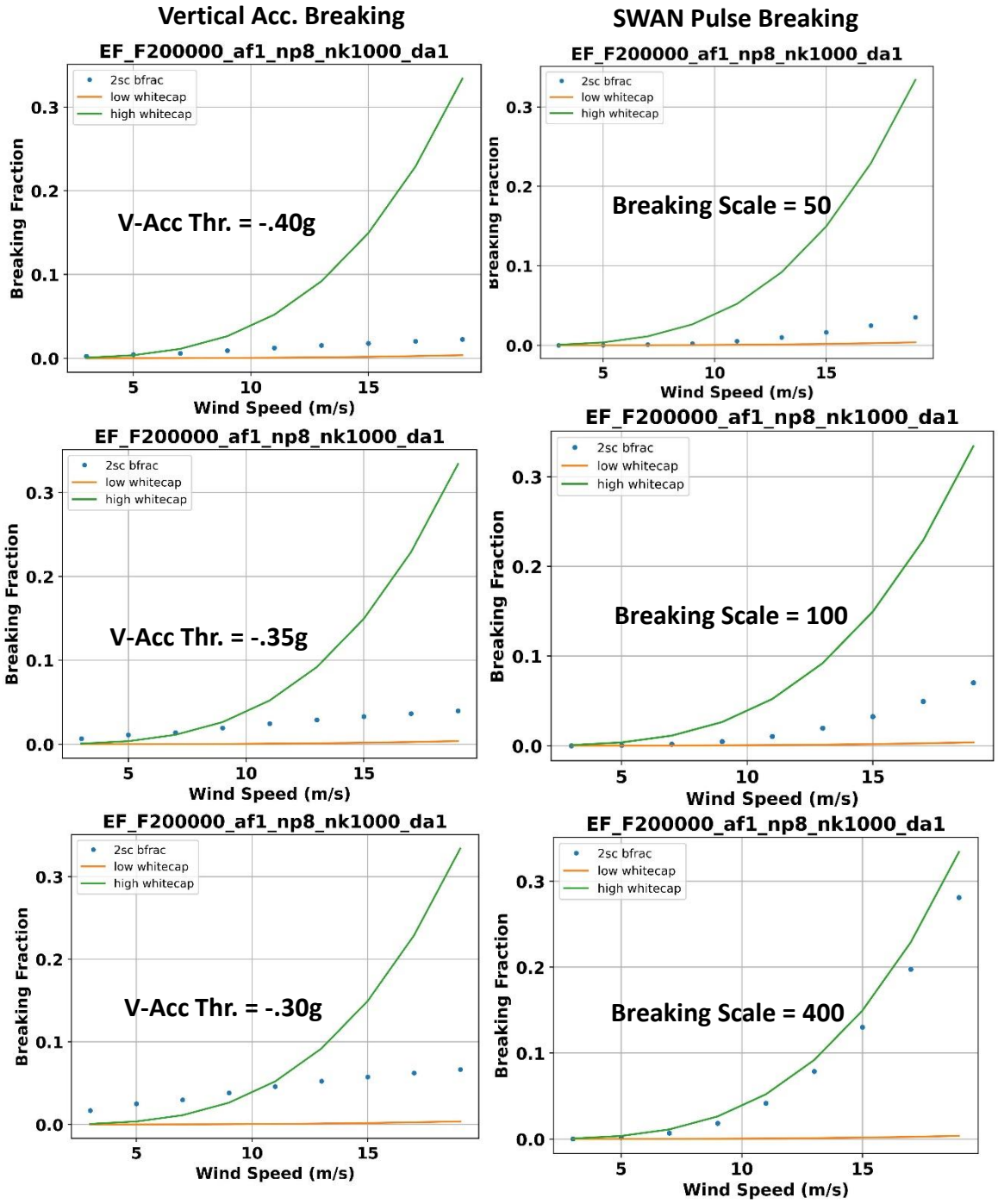

Figure 11: Breaking fraction from the RCS model (blue dots) versus published whitecapping models (green and orange lines) the span the range of model results. Left column uses the vertical acceleration model, right column uses the SWAM model. Lines are for the same parameters as in Figure 10.

4.0 Generating Wave Spectra Perturbed by Changes in Surface Current and Depth

The next tool required is one to generate a spatial grid of two-dimensional wave height spectra that have been perturbed by a changing surface current field and/or a changing water depth field. To do this we will use a solver for the wave action balance equation (WABE). The wave action balance equation is a well-used model for predicting the modulations of surface waves as these propagate through a surface current field and/or changing bathymetry (Phillips, 1984; Lyzenga and Bennett, 1988; Lyzenga, 1991; Kudryavtsev et al., 2003; Rascle et al., 2014, O'Dea et al., 2022). There are many way to solve these equations; we have implemented a ray-trace approach that in its most general formulation works as follows. We define an (x,y) grid over which we will be calculating wave spectra, and a (k_x,k_y) grid over which we will be calculating the wave spectrum values. Thus the output of the wave action balance equation will be a four-dimensional function of wave spectra: S(x,y,k_x,k_y). For each (x,y) location, and for each (k_x,k_y) spectral value at this location, we first determine the path that this wave took to get to this location. We do this by solving a subset of the wave action balance equation, the so-called ray-trace equations, that determine the time evolution of (x,y,k_x,k_y). We solve these backward in time until we reach the edges of the domain we are using. This gives us the starting location, starting (k_x,k_y), and starting time at which this wave entered the domain. We then give this wave an amplitude that is consistent with whatever source function we have implemented for the edges of the domain. For example this can come from a model for the wind-generated ambient wave field, or it can be *in situ* observations of shoaling waves in deep water. For our case in this study, it will be a combination of the Elfhouhailly wind-wave model with a swell wave whose parameters will come from *in situ* measurements (see Section 6 below). We then solve the same set of equations forward in time, with the addition of the equation that determines the changes in wave amplitude (or more correctly the wave action), until we reach our initial starting point. We then assign that (x,y) and (k_x,k_y) location the associated wave spectral value and move to the next location.

The other major method of solving the wave action balance equation is through finite difference algorithms. These generally calculate the wave spectral values over all (x,y,k_x,k_y) simultaneously using various iterative approaches. We have implemented the ray-trace approach because we have found that it can be significantly faster than finite difference algorithms (particularly when we want a well-sampled wave spectra), and it allows us to disconnect the accuracy of the solution from the grid we are solving it on. We have compared the ray-trace approach directly with SWAN (a standard finite difference code), where we have found the ray-trace approach to be almost 10 times faster for solving the shoaling wave problem. An additional advantage of the ray-trace approach is that it allows a spatial map of source functions to be defined, such that we can use those source functions for wave amplitudes only if the ray passes through them.

Thus in general we solve the wave action balance equation in the following form, where the partial differential equation has been put into the set of ordinary differential equations (Lyzenga and Bennett, 1988):

$$\frac{dx}{dt} = c_{gx} + u \qquad (36)$$

$$\frac{dy}{dt} = c_{gy} + v \tag{37}$$

$$\frac{dk_x}{dt} = -k_x \frac{\partial u}{\partial x} - k_y \frac{\partial v}{\partial x} - \frac{\partial w}{\partial x} \tag{38}$$

$$\frac{dk_y}{dt} = -k_x \frac{\partial u}{\partial y} - k_y \frac{\partial v}{\partial y} - \frac{\partial w}{\partial y} \tag{39}$$

$$\frac{dA}{dt} = F_S(A) \tag{40}$$

where u(x,y) is the current field in the x-direction, v(x,y) is the current field in the y-direction, c_{gx} is the group velocity in the x-direction, c_{gy} is the group velocity in the y-direction,

$$c_{gx} = \frac{k_x}{k} \frac{\left(\left[9.81k + \frac{T}{\rho}k^3\right]\mathrm{sech}^2\{kd\}d + \left[9.81 + 3\frac{T}{\rho}k^2\right]\tanh(kd)\right)}{2\omega} \tag{41}$$

$$c_{gy} = \frac{k_y}{k} \frac{\left(\left[9.81k + \frac{T}{\rho}k^3\right]\mathrm{sech}^2\{kd\}d + \left[9.81 + 3\frac{T}{\rho}k^2\right]\tanh(kd)\right)}{2\omega} \tag{42}$$

ω is the intrinsic frequency of the wave defined as

$$\omega^2 = \left(gk + \frac{T}{\rho}k^3\right)\tanh(kd) \tag{43}$$

with k being the wave number of the wave ($k^2=k_x^2+k_y^2$), g is the gravitational constant (9.81), T is the surface tension , ρ is density of water (T/p = 74 cm^3/s^2) and d is the water depth (which is a function of (x,y)). Finally, in Eq. (40) A is the action defined as A=S/ω where S is the wave spectral value and F_S is the equation that determines the sources and sinks of energy for the waves.. Eqs, (36) – (39) are the ray-trace equations which determine the time evolution of x,y,k_x,k_y. Note that these do not depend on the wave action (or spectral value); they just determine the path in (x,y,k_x,k_y) space that the wave takes as it propagates through the current field. Solving these four equations backward in time, for example, generates the path that the wave took to get to this location (i.e. the (x,y) values) and the changes in wavenumbers that were generated due to changing depths and/or changing surface currents (i.e. the in (k_x,k_y) values). Eq. (40) is then solved forward in time to generate the changes in wave height as the wave propagates to shore.

The expression for the changes in action with time in Eq. (40) is for the full two-dimensional spectrum of the ocean waves. One can also formulate the wave action balance action of a wave packet that has a single dominant spectral component. This would represent the situation of a quasi-monchromatic wave moving through a changing bathymetry or current field. Instead of a spectrum, S, we have the total energy in the wave packet, E. The action, A, is now E/ω and the energy of the packet is $E=(1/8)\rho g(H_{rms})^2$. For this case we need to add a term to the change in action that accounts for a change in the energy due to the change in the motion (or group velocity) of the wave. Therefore in this case Eq. (40) becomes

$$\frac{dA}{dt} = F_S(A) - A\left(\frac{\partial}{\partial x}\left[c_{gx} + u\right] + \frac{\partial}{\partial y}\left[c_{gy} + v\right]\right) \quad (44)$$

If we need to generate wave height estimates, the expression for source and sinks of the wave energy, F_S, is where all the action is – if you will pardon the pun. The functional forms and parameterizations of these forms vary widely throughout the literature. Everyone agrees that there has to be a wind growth term of the form βA, but the parameterization of β varies widely (see below). There is usually a viscous dissipation term of the form $-4\nu k^2$ (where ν is the kinematic viscosity, ν = 1.3e-6) and/or a friction dissipation term (if the waves feel the bottom). Everyone also agrees that there needs to be a dissipation term for wave breaking, but both the functional form and parameterization of this term vary widely. There is often some wave-wave interaction term (although when solving the wave action balance equation over short time scales this term is usually ignored) that transports energy between spectral locations. Finally, there is often a so-called Phillips growth term (which is a constant independent of action) that creates waves when all other sources are zero (this is usually attributed to changes in atmospheric pressures across the ocean surface) which in practice plays the role of re-growing waves when the current perturbations would wipe them out (and thus without any other source term they would stay at zero amplitude from then on).

Very generally speaking these various approaches for F_S fall into two camps. One camp creates a term for each source/sink based on some physics model and then adds them together (see, for example, Collins, 1972; Komen et al., 1984; Battjes and Stive, 1985; SWAN Technical Documentation, 2007). In general the resulting terms have the form of the wave spectrum multiplied by some function of spectral measures (such as wave steepness or significant wave height). This approach has the advantage of directly incorporating the physics. However it has a disadvantage in the fact the in the absence of currents and bathymetric changes the wave spectrum does not necessarily relax back to the initial wave field (i.e. solving the wave action balance equation for F_S=0 should generate the original, unperturbed spectrum). These formulations are most appropriate when modeling shoaling waves, since they should never actually relax back to the original, deep water, value

.

The standard form for the sources/sinks of action for these approaches is

$$F_S(A) = \beta A - \frac{D_b}{\omega}\left(\frac{S}{\iint S}\right) - \frac{D_f}{\omega}\left(\frac{S}{\iint S}\right) \quad (45)$$

for the full spectrum model and

$$F_S(A) = \beta A - \frac{D_b}{\omega} - \frac{D_f}{\omega} \quad (46)$$

for the wave packet case where βA is the wind growth term, D_b is the energy dissipated by breaking, D_f is the energy dissipated by friction, and as mentioned above S is the wave height spectrum and S/ω is the action A for the spectral case.

One friction dissipation term comes from (Thorton & Guza, 1983)

$$D_f = c_f \frac{\rho}{6\pi}\left(\frac{\omega}{\sinh[kd]}\right)^3 H_{rms}^3 \quad (47a)$$

where c_f is a constant (around 0.01) and H_{rms} is the root-mean-squared wave height. A second model comes from (SWAN Technical Documentation, 2007)

$$D_f = c_f \frac{1}{8}\rho g\left(\frac{\omega H_{rms}}{g\sinh[kd]}\right)^2 \quad (47b)$$

where cf=0.067 for a fully developed waves in shallow water and cf=0.038 from the JONSWAP model for swell waves in shallow water.

There are many models for the breaking dissipation term. The three main ones that we have implemented for breaking from wave shoaling are (note that all of these should be multiplied by (1/8)ρg to give the correct units, but in our implementation we have normalized this factor out of everything):

$$D_b = \frac{\omega}{\pi}\exp\left[-\frac{H_S^2}{H_{rms}^2}\right][H_S^2 + H_{rms}^2] = \frac{\omega}{\pi} f_b [H_S^2 + H_{rms}^2] \text{ (Disconnected Flow)} \quad (48)$$

$$D_b = \frac{\omega}{\pi} Q_b H_S^2 \text{ (SWAN Model: SWAN Technical Documentation, 2007)} \quad (49)$$

$$D_b = 0.15\gamma H_{rms}^2 \left(\frac{c_{gx}}{H_S}\right)\exp\left[-\frac{H_S^2}{H_{rms}^2}\right] \text{ (Stable Wave: Dally et al., 1985)} \quad (50)$$

where f_b is the breaking fraction for the Disconnected Flow model (the first equation in Eq. (48) shows what it is equal to), Q_b is the breaking fraction in the SWAN model which is 0 for $R \leq 0.2$, 1 for $R \geq 1.0$, and

$$Q_b = Q_0 - R^2 \frac{Q_0 - \exp\left(\frac{Q_0 - 1}{R^2}\right)}{R^2 - \exp\left(\frac{Q_0 - 1}{R^2}\right)} \quad (51)$$

for $0.2 < R < 1$ where $R = H_{rms}/H_S$, $Q_0 = 0$ for $R \leq 0.5$ and

$$Q_0 = (2R - 1)^2 \text{ , } R > 0.5 \quad (52)$$

Throughout Eqs. (48) - (52) H_S is the stable wave height which is the wave height above which breaking starts to occur. There are many models for this, with three that are often used being:

$$H_S = \gamma d \quad \text{(McCowan, 1891)} \quad (53)$$

$$H_S = \frac{\gamma}{k}\tanh[kd] \qquad \text{(Miche, 1954)} \tag{54}$$

$$H_S = \frac{.88}{k}\tanh\left[\frac{\gamma kd}{.88}\right] \qquad \text{(Battjes and Janssen, 1978)} \tag{55}$$

where γ is a parameter that can vary from a constant (usually in the range from 0.4 to 0.8) or a function of either the incoming wave steepness, $H^0_{rms}k^0$

$$\gamma = .5 + .4\tanh\left[33\frac{H^0_{rms}k^0}{2\pi}\right] \quad \text{(Battjes and Stive, 1985)} \tag{56}$$

$$\gamma = .39 + .56\tanh\left[33\frac{H^0_{rms}k^0}{2\pi}\right] \qquad \text{(Baldock et al., 1998)} \tag{57}$$

or the beach slope, s,

$$\gamma = 3.2\tanh[s] + .3 \tag{58}$$

We should note the following. For the stable wave dissipation model in Eq. (50) the original Dally et al. formulation has $\gamma = 0.4$ (a constant) and uses the stable wave height expression in Eq. (54) (with $\gamma = 0.4$). Our implementation is an attempt to generalize this for difference models of γ and of the stable wave height. However we have also encoded the original Dally et al. formulation as an option for D_b.

Note that all of these breaking terms assume that the waves are feeling the bottom (i.e. they represent the breaking of shoaling waves). There are also wave breaking terms for deep water breaking (or whitecapping) that were discussed above. The pulse-based whitecapping energy dissipation term is implemented using Eqs. (26)-(31) above, where E_D in Eq. (26) is the same term as D_b in Eq.s (45) and (46). There are other whitecapping models available; we refer the reader to (SWAN Technical Documentation, 2007) for the details of how to implement these other dissipation terms.

The second camp starts from the assumption that for F_S=0 the solution of the wave action balance equation should be the original equilibrium spectra and essentially builds a perturbation model for the sources/sinks (see, for example, Lyzenga and Bennett, 1988; Lyzenga, 1991; Kudryavtsev and Makin, 2002). The advantage of this approach is that it builds in the right relaxation condition once the waves leave the perturbation field (usually in this case a current field). But the disadvantage is that it cannot in general include all the physics-based terms, and in particular the dissipation from either wave breaking and/or wave-wave interaction is usually lumped together into one empirical term.

The general expression for F_S in this camp is

$$F_S(A) = \left(\beta - 4\upsilon k^2\right)A + 4\upsilon k^2 A_o - \beta\frac{A^n}{A_o^{n-1}} + T \tag{59}$$

where β is the wind growth rate (the term mentioned above), $4\nu k^2$ is the viscous dissipation term (mentioned above), A_o is the equilibrium action (i.e. the action of the ambient surface waves) and T represents spectral transport terms (which must equal 0 for A_o). Note that by definition we have that $F_S(A_o)=0$. The middle term in Eq, (59) is the Phillips growth term (which has to be there to offset the dissipation term for the equilibrium action).

In equation (59) all the dissipation (other than viscous) is lumped into the non-linear term, and values for n can vary widely from n=2 (Lyzenga, 1991) to n being a function of wavenumber and goes from 2 to 6 (Kudryavtsev et al, 1999; Kudryavtsev and Makin, 2002). We have incorporated all the models for n that we have found in the literature as options in our solver. In this program we have ignored the spectral transport term (essentially the wave-wave interaction term) since we are solving the equation over relatively short time scales.

This form of the source/sink term is most appropriate for the case where the waves are moving through a surface current perturbation (usually in deep water so depth is not a parameter).
So even when we choose among all the options discussed above, we still need to choose a parameterization for the wind growth rate β. Many versions exist in the literature, and for completeness which have also incorporated all of them as options into the code. They are as follows.

$$\beta = .0003\omega\left[\frac{u}{c}-1\right] \text{ (Synder et al., 1981)} \tag{60}$$

$$\beta = .00019\omega\left[\frac{A}{c}-1\right] \text{ (Donelan and Pierson, 1987)} \tag{61}$$

$$\text{where } A = u + \frac{u_*}{\kappa}\ln\left[\frac{.1\pi}{k}\right]$$

The rest all have the following form

$$\beta = C_\beta\omega\left(\frac{\rho_a}{\rho_w}\right)\left(\frac{u_*}{c}\right)^2 \tag{62}$$

Where

$$C_\beta = 31.8 \text{ (Plant and Wright, 1977)} \tag{63}$$

$$C_\beta = 36\left(1-1.3\left(\frac{c}{u}\right)^5\right)\left(1-a_c f\right) \text{ (Makin and Kudryavtsev, 1999)} \tag{64}$$

where $a_c = 0.2 + 0.6\frac{u}{25}$ and f=1 for waves < 1m, 0 else

$$C_\beta = \left(\frac{1.2}{\kappa^2}\right)\Lambda \ln^4 \Lambda \quad \text{(Jassen, 1991)} \tag{65}$$

where $\Lambda = .0144\left(\frac{u_*}{c}\right)^2 \exp\left[\frac{\kappa c}{u_* \cos\theta}\right]$

$$C_\beta = 1.5\left(\frac{1}{\kappa}\ln\left[\frac{\pi}{kz_o}\right] - \frac{c}{u_*}\right) \quad \text{(Kudryavtsec et al., 2002)} \tag{66}$$

where $z_o = \frac{.0144u_*}{g}$

$$C_\beta = F(R_e) \quad \text{(Kukula and Hara, 2005)} \tag{67}$$

where $R_e = \frac{2\pi u_*}{\kappa\nu}$

For all of these equations, u is wind speed, w is wave intrinsic frequency, c is the wave phase speed, u* is the friction velocity, κ is the van Karmen constant and ν is the kinematic viscosity. If one plots these various beta terms, in general the Plant and Wright model, Eq. (63,) tends to have close to the highest value while the Kukula and Hara model, Eq. (67), tends to have close to the lowest value. In what follows we will use these two models to bracket the extremes of the effect that the wind growth term will have on the final values. The Plant and Wright model is probably the most widely used, and it is our default. However, we shall show below that the wind growth model we use can have a significant effect on the final RCS values, thus we will chose a model based on the one that best fits our validation data (discussed below).

We also need the angular dependence for the beta term. This is as unknown as the beta model, but there are three normally used forms: (1) $\cos(\Delta\phi/2)$; (2) $\cos^2(\Delta\phi/2)$; (3) $\text{abs}[\cos(\Delta\phi)]$, where $\Delta\phi$ is the angle between the wave propagation direction and the direction the wind is blowing to. Options (1) and (2) are designed to have no wind wave growth when we are 180 degrees away from the wind direction, with slightly different fall-offs in wind energy. Option (3) has the somewhat strange property of having the same wind growth rate both in the wind direction and at 180 degrees from the wind directions, with no wave growth at ±90 degrees from the wind direction. The default option is (1).

To solve the differential equations we have implemented a fifth-order Runga-Kutta scheme (see, for example, (Gellert et al., 1975, section 29.3: Numerical models for integration and

differentiation) for solving the ray-trace equations (36) through (39). This scheme uses five intermediate steps to approximate the next value of the numerical integration of the differential equations and has the advantage of dynamically changing the time step during the solution to maintain the accuracy of the resulting actions. The coefficients for the various steps come from the Cash-Karp embedded method.

Finally, for the case of waves moving through a changing current pattern we need to deal with trapped waves; i.e. waves that due to the perturbation from surface currents will never make it out to the edges of the domain. During the solution of the ray-trace equations we track how many times the wave changes its propagation direction by 180 degrees. If this happens four times, we called this a trapped wave and set its spectral value equal to its equilibrium value. Note that we cannot do this after one such rotation, since many waves actually can rotate around 1-3 times before eventually leaving the current field.

We can use Eq, (59) to calculate the relaxation rate, β_r, as (setting T=0 to ignore the spectral transport term)

$$\beta_r = -F_S'(A)\big|_{A=A_o} = (n-1)\beta + 4\upsilon k^2 \tag{68}$$

which is the rate at which that wave relaxes toward the action equilibrium value) for values of the action around the equilibrium value. The inverse of this is the time it takes to relax to equilibrium, and if this is significantly larger than the time it takes the wave to move across significant changes in the current pattern or depth changes, that means that the wave will relax to its equilibrium value before the currents/depths can have any impact on the spectrum. This means that the waves have no "memory" and are only responding to the instantaneous current field. In this case there is an analytical solution to the WABE (Lyzenga, 1991; Rascle et al.,2014; O'Dea et al., 2022)

$$\frac{N}{N_o} = \frac{1}{\beta_r}\left[\left(\frac{\partial u}{\partial x}\cos\varphi + \frac{\partial v}{\partial x}\sin\varphi\right)\left(m_k\cos\varphi - m_\varphi\sin\varphi\right) + \left(\frac{\partial u}{\partial y}\cos\varphi + \frac{\partial v}{\partial y}\sin\varphi\right)\left(m_k\sin\varphi + m_\varphi\cos\varphi\right)\right] \tag{69}$$

where

$$m_k = \frac{\partial \ln[N_O]}{\partial \ln[k]}, m_\varphi = \frac{\partial \ln[N_O]}{\partial \varphi} \quad , \tag{70}$$

N is the perturbed wave action, N_O is the equilibrium wave action, u(x,y) is the current in the x-direction, v(x,y) is the current in the y-direction, k is the wavenumber of the spectral location and φ is the angle of the spectral location. Eq. (69) is in polar coordinates for the action N(k, φ), its equivalent in rectangular coordinates, $N(k_x,k_y)$ is

$$\frac{N}{N_o} = \frac{1}{\beta_r}\left[\left(\frac{\partial u}{\partial x}\cos\varphi + \frac{\partial v}{\partial x}\sin\varphi\right)\frac{k}{N_O}\frac{\partial N_O}{\partial k_x} + \left(\frac{\partial u}{\partial y}\cos\varphi + \frac{\partial v}{\partial y}\sin\varphi\right)\frac{k}{N_O}\frac{\partial N_O}{\partial k_y}\right] \tag{71}$$

Eqs. (69) or (71) can be evaluated analytically for a given current field and thus there is no need to perform the ray-trace solution to the WABE. The large relaxation rates that allow this will be for the very small waves around the Bragg regime. If Bragg scattering was sufficient for calculating RCS, then we could just use these expressions directly and could generate an instantaneous result. Unfortunately, as discussed above, we need a two-scale model to accurate calculate RCS, which means we need the wave spectral component for all waves, including the longer waves which are contributing to the slope variances, so we need to run the full ray-trace solver for these rays. However, we can use these equations to significantly speed up the calculations by only running WABE for the longer-scale waves and using Eqs. (69) – (71) to determine the spectral values for the short-scaled waves. In our implementation we use a wavenumber cut=off of $2\pi/(2.5*\lambda)$ where λ is the radar wavelength. We have tested this cut-off by running our WABE solver for these same waves and comparing to the analytical results from Eqs. (69) – (71) and they have matched.

5. Validation of the End-to-End Model Using Historical Internal Wave Experimental Data

In section 3 we presented validation of the RCS model by comparison to *in situ* data observations of RCS as a function of wind conditions and imaging geometry. To validate the perturbed wave spectra model in Section 4, we would ideally need *in situ* observations of two-dimensional wave height spectrum across an *in situ* measured surface current field. Such data are not readily available, so the next best thing would be to use experimental data where *in situ* surface currents were measured with coincident RCS modulations across the current field. This tests the full end-to-end model (using WABE to calculate the perturbed wave spectra, then using the RCS model to calculate RCS modulations), but assuming that we have adequately validated the RCS model this can then be used to validate the spectra perturbation model. Such data was measured during a previous ONR experiment called the Synthetic Aperture Radar (SAR) Internal Wave Signature Experiment (SARSEX) conducted in 1984 in the New York Bight region of the Atlantic Ocean. The purpose of the experiment was to collect *in situ* data sufficient for developing and testing models for predicting the SAR signature of internal waves. As part of the experiment, surface currents induced by internal waves were measured and compared with airborne measurements of RCS values across the internal wave. A document of these values is in (Kasischke et al., 1988) which has the peak/background for the SAR modulation (in dB) as a function of the SAR collection geometries and surface currents. The SAR imagery was collected mainly looking either in the direction of the internal wave propagation or 180 degrees from that direction (there are a few points collected at 90 and 45 degrees from the internal wave propagation), over a number of different internal waves. The wind speed varied between 4 and 6 m/s and generally blew in the same direction (approximately -135 degrees with respect to the internal wave propagation direction). Thus we can consider the wind essentially constant so that the dominant parameters of interest are the SAR incidence angle (which we know has a significant impact on RCS) and the strength of the internal wave surface current. We parameterize the latter by assuming the current to be a sech**2 function based on basic two-layer theory for internal waves and using the peak current gradient defined as $du_{PEAK} = 2*(\text{peak current})/w$, where w is the width parameter in the current profile $u(x) = u_0 \text{sech}^2(x/w)$, u_0 is the peak current, and $w=d/(2*0.88)$ where d is the full width at the half-peak location; u_0 and d are documented in the reference. The top plot in Figure 12 shows the peak/background SAR modulations (in dB) from (Kasischke et al., 1988) as a function of incidence angle where each colored line comes from a different value

of du_{PEAK} (i.e. a different internal wave), the value of which is indicated in the plot. The slope of the SAR modulations as a function of incidence angle goes from -0.14 to -0.27 without any trend with respect to du_{PEAK} so using the average of these we will correct the SAR modulations back to a constant incidence angle of 45 degrees. The bottom plot in Figure 12 shows the SAR modulations normalized to a 45 degree incidence angle as a function of du_{PEAK}. There is a slight trend, but it is not very pronounced. The dotted line is the least-squared linear fit and the dashed lines are ±1.5 dB around the fit. Overall, for these internal waves the SAR modulations go from 2 to 4 dB, which means the modulations in power go from 1.6 to 2.5. We will define the SAR RCS modulations for our results as (peak/background-1) so this value would go from 0.6 to 1.5. In (Kasischke et al., 1988) they claim that the uncertain of their modulations values is ±2.2 dB, which for a mean value of 3 dB gets us to 0.8 to 5.3 db (about the full range of the points in the bottom plot of Figure 12) which means in power from 1.2 to 3.3, and for our modulations from 0.2 to 2.3.

In (Lyzenga and Bennet, 1988) they put together a two-scale model very similar to what we have in this report and ran it for a subset of the internal wave surface currents in (Kasischke et al., 1988). They report RCS modulations of around 2 dB which gives modulations in power of 1.6, and in terms of our modulations 0.6.

So for our test case, we used a sech**2 current with the peak current of 0.42 m/s and half-width of 116m (this is the internal wave in (Kasischke et al., 1988) from SARSEX4, Pass5, Wave 3). Note that this gives us a du_{PEAK} value of 0.0064 and in Figure 12 the corresponding RCS modulations are circled in red. The RCS modulations vary from 2.7 – 3.2 dB which corresponds to 0.8 – 1.1 in linear RCS modulations. We assume that the current is constant in the y-direction and varies in the x-direction. We know the wind speed and direction, so we can map the direction into the current field x-, y-coordinate system. Finally, we used a SAR incidence angle of 45 degrees and a SAR look angle of 0 degrees (so looking in the same direction the internal wave is propagating). Based on the results in Section 3 we assume that the wave spectrum outside of the current field will be the Elfhouhailly wavenumber spectral model with the Romeiser et al. angular spectral model. At this point we do not know if there was a swell component to the wave field, so we will assume not. We will then generate a one-dimensional spatial grid of wave height spectra along the x-direction extending across the internal wave current field. We will then run our RCS model on each output spectrum and generate a plot of RCS across the current field.

We are using these data as a test of the WABE solver, so we want to run the solver using the range of possible input parameters. As mentioned in Section 4, the wind growth term has a significant impact on the resulting wave spectra, so we ran the WABE solver using the generally lowest model for the wind growth (the Kukula & Hara model, Eq. (67)) and the generally highest model (Plant & Wright, Eq. (63)). We also ran all three of the wind growth angular models. Finally, since we are using the perturbation model in Eq. (59) we ran it with and without the viscosity terms (since they have a significant effect on the energy being put into the waves) and

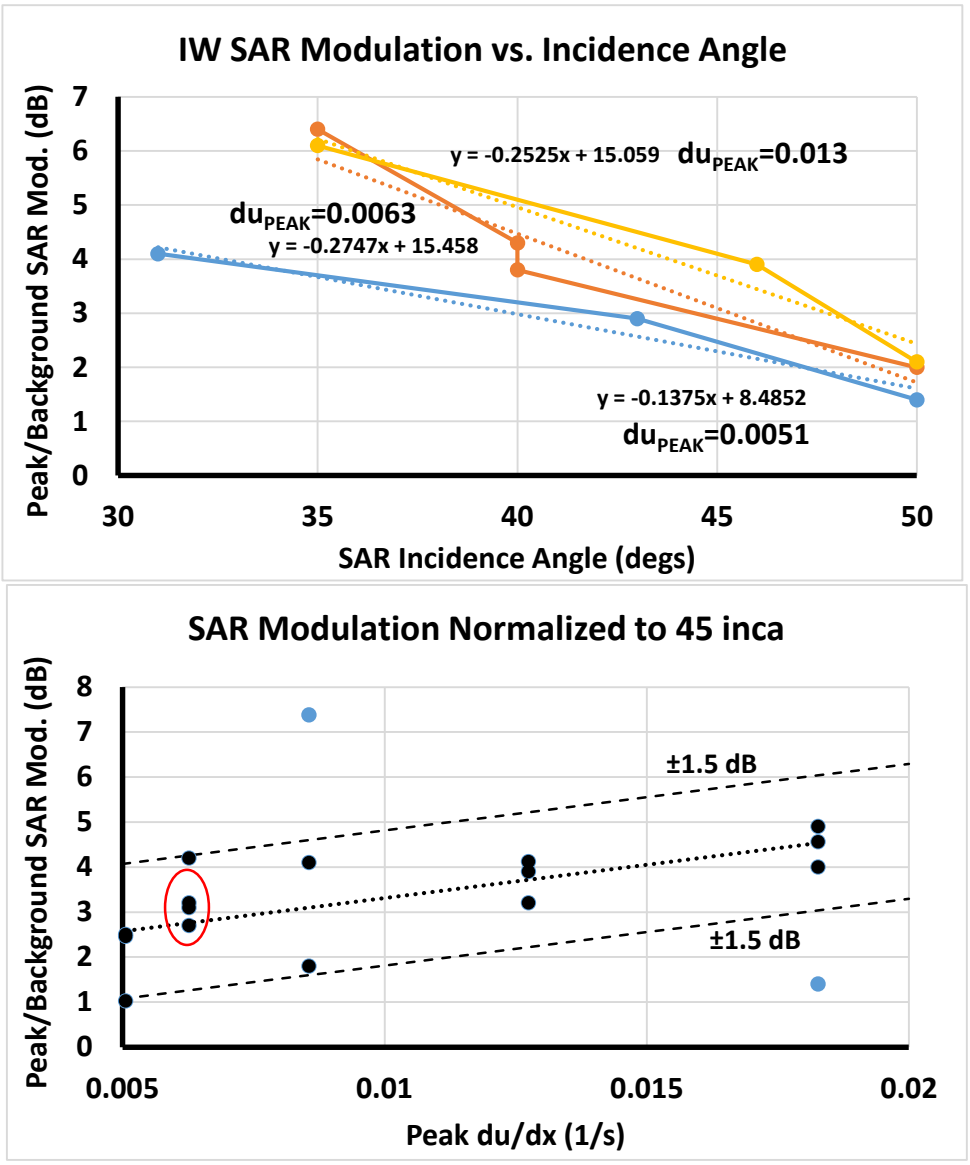

Figure 12: Top plot shows peak/background SAR modulations (in dB) from (Kasischke et al., 1988) as a function of incidence angle where each colored line comes from a different value of du_{PEAK} (i.e. a different internal wave), the value of which is indicated in the plot. These fits were used to normalize the SAR modulations to a 45 degree incidence angle; these are shown in the bottom plot as a function of du_{PEAK}. Dashed line is a linear fit (minus the blue dots). Points circled in red are for the peak du/dx value used in the validation.

with n=2 (we found that higher values of n removed too much energy from the waves). All of the RCS model parameters were set as described in Section 3 above.

Figure 13 shows the resulting RCS modulations using the V-Acc breaking model with a threshold on vertical acceleration for breaking of -0.3g; the lower range of threshold values that generated RCS values consistent with the CMOD5 model and the test set of observations (see Section 3). All 12 RCS plots using the various WABE parameters (low wind growth / high wind growth; RHS with / without viscosity term; three angular functions for wind growth) are shown. In the set of four plots, the upper, left plot shows the different components of the two-scale RCS model. One can see that the Physical Optics (PO) term (blue lines) is too low to make a contribution since the incidence angle is 45 degrees. One can also see that the breaking wave term (black lines) is approximately 6dB below the other terms unless we are near the peak of the internal wave current, in which case it is similar to the other terms. The upper, right plot shows the actual RCS modulates (defined as RCS/mean(RCS)-1.0) for each of the 12 plots. Note that they all have the exact same shape; the only difference is the value of the peak modulation. The lower, left plot shows the breaking fraction from the RCS model (colored lines) versus the high / low whitecapping models that are discussed in Section 3 (dashed lines). Finally, and most important, the bottom, right plot shows the peak RCS modulations as a function of the current derivative at the peak RCS value (which is essentially the same for all values (0.00488 1/s). We have circled with a red ellipse all the RCS modulations that came from one combination of low wind growth / high wind growth (wind growth is referred to as beta in the figure) and RHS with / without viscosity term (indicated as "Vis" or "No Vis"). The three points within each ellipse come from the three angular functions for the wind growth term; note that they are generally the same for each ellipse with no observable trend with respect to the angular function. For all the results, the highest modulations came from having no viscosity term in the RHS and using the low wind growth (beta). This generated RCS modulations around 1.4 using the -0.3g threshold. The middle modulations came from either using no viscosity terms with high wind growth, or using the viscosity terms with low wind growth. This generated around 1.0 for the -0.3g threshold. The lowest modulations came from using the RHS with viscosity terms and the higher wind growth. This generated RCS modulations around 0.4 and 0.6. The results from (Kasischke et al., 1988) for our peak du/dx are circled in red in Figure 12 go from 0.8 to 1.1 (using our definition of RCS modulation). This range is indicated in Figure 13, with the middle modulation results being pretty much right at the middle of the this range. One result using a threshold of -0.4g was calculated to model what was generated in (Lyzenga and Bennet, 1988) (no Vis, high beta, largest value) which generated a modulation of 0.76 versus the reported 0.6. So overall, if we use a threshold of -0.3g with the V-Acc breaking model, we are able to reproduce the range of modulations reported in (Kasischke et al., 1988), and the model when run with the same parameters seems consistent (if a little high) with what is reported in (Lyzenga and Bennet, 1988).

Figure 14 shows the same set of results but using the SWAN breaking model with a scale of 400; the high range of scales that generated RCS values consistent with the CMOD5 model and the test set of observations (see Section 3). The exact same trends of RCS modulations versus WABE parameters came out here (the top three from no viscosity terms and low wind growth, the bottom three from having viscosity terms with high wind growth, and the other two parameter sets generating the middle results); we did not put the ellipse around them. However,

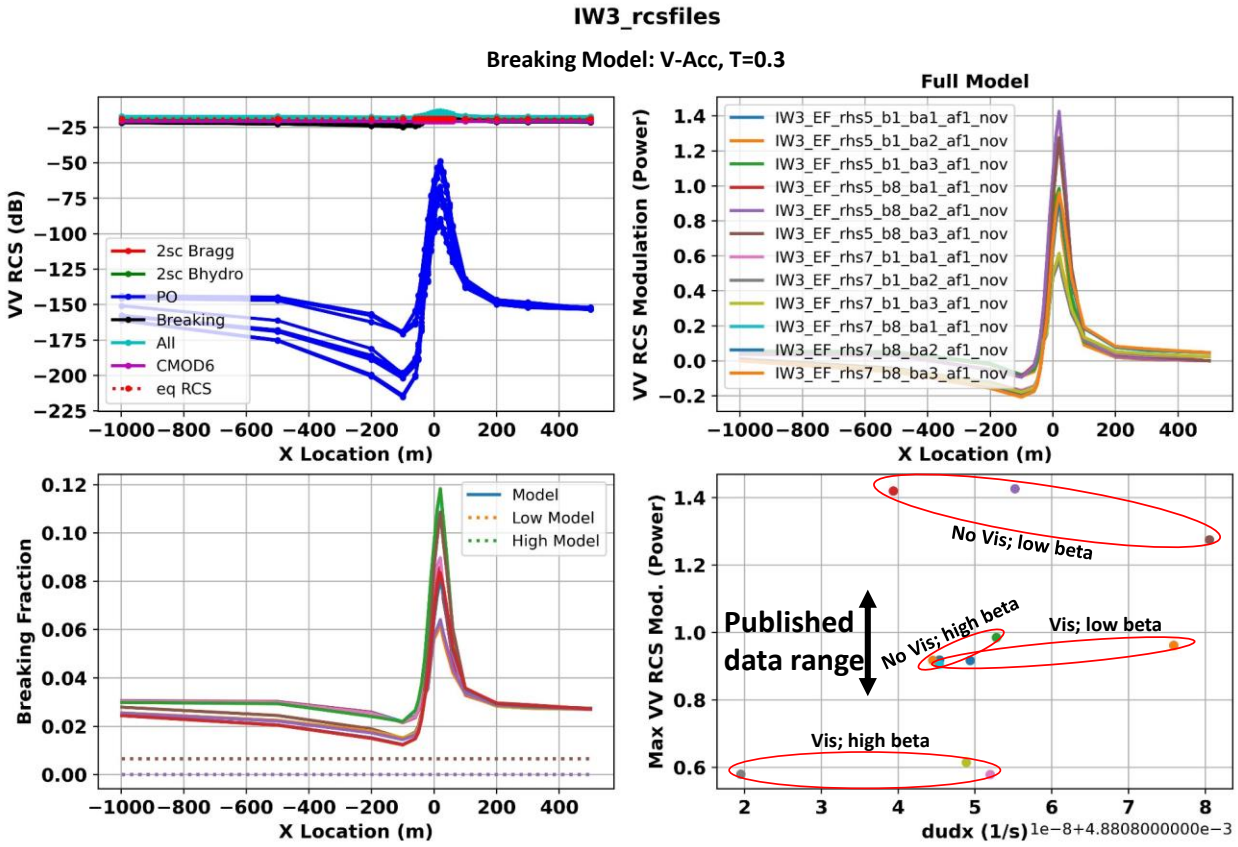

Figure 13: Model results for the internal wave validation test. Upper, left plot shows the individual RCS model components across the current field. Bottom, left plot shows the resulting breaking fractions (solid lines) compared to the low/high whitecapping modesl (dotted lines). Upper, right plot shows the RCS modulations across the current field for all the various WABE RHS combinations. Bottom, right plot shows the peak RCS modulation values for each WABE RHS combination. These results use the vertical acceleration breaking model with a threshold of -0.3g. Black arrow in the bottom, right plot shows the range of published RCS modulations for this current field.

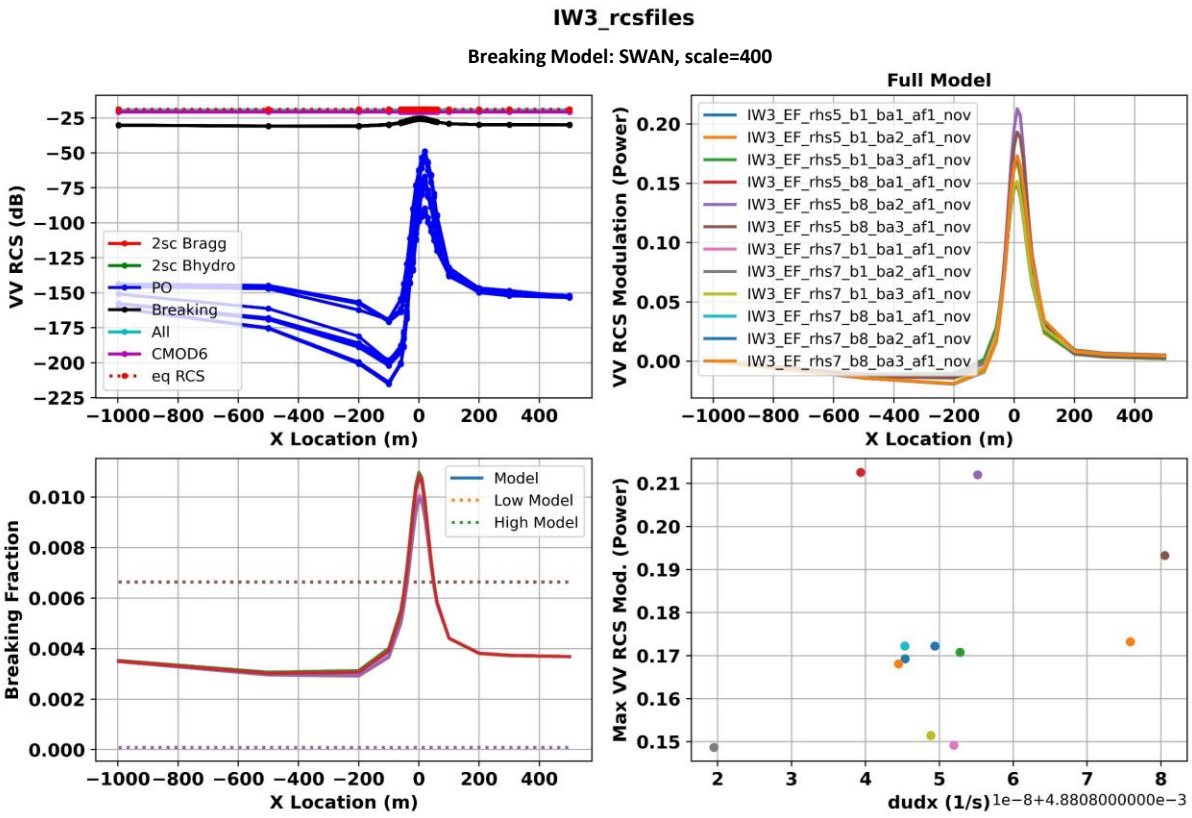

Figure 14: Same format as Figure 13, but with the SWAN breaking fraction model with a scale factor of 400. Note that the maximum RCS modulations (bottom, right, plot) are significantly lower than the results in Figure 13 and the published results.

the modulations here are significant smaller than in Figure 13, and much smaller than published in (Kasischke et al., 1988) and (Lyzenga and Bennet, 1988). This is dominantly due to the breaking term, which is significantly lower than the other terms using this breaking model, and does not approach the other terms in the peak modulation region. Without this larger breaking RCS term, the final modulations do not approach the published values.

Based on these comparisons, we should use the V-Acc breaking model with a threshold of -0.3g. This generates RCS values consistent with CMOD5n and published observations (see Section 3) and generates results consistent with the published internal wave modulations. We can achieve the mean result for the internal wave test (a modulation of ~1) by using either the RHS with no viscosity terms coupled with the higher wind growth term, or the RHS with viscosity terms coupled with the lower wind growth term.

However we need to keep in mind that this was not a direct test of the wave action solver, but required a combination of the solver with the RCS model. It could be that the wave action solver is not perturbing the wave spectra sufficiently for the given current and we have to compensate for that by using the larger breaking wave RCS model. We have not put in a component to transfer energy between spectral components, and in (Lyzenga, 2010) they claim that this term is important to generate higher RCS modulations, so this may be why we need higher breaking

terms. The addition of the energy transfer term is but complicated and not well developed, so it will have to wait for further development. For now, the model described above generates results consistent with our two validation studies, so we will use it in what follows under the assumption that even if the intermediate wave spectra perturbations are incorrect, the mapping from current to RCS modulations is still correct.

6. Comparing to Mobile Bay SAR Image Modulations

Our final analysis is to compare this model to what we observe in the SAR images collected during the Mobile Bay experiment in 2021. David Ralston of WHOI graciously provided model run outputs of the predicted surface currents coincident with the SAR image collections. Our goal is to use our RCS model to generate the surface currents consistent with the RCS modulations, and compare them to the model currents. We will look at two images: one collected on 09 June 2021 at 23:47:04 GMT and one collected on 10 June 2021 at 23:41:04. Both were collected close to mid-ebb tide. To get the open ocean METOC data we used the NDBC buoy #42012 which is approximately 30 km from shore. The parameters associated with each image are:

- For 09 June, the wind speed was ~5 m/s, the wind was blowing to 26° (all angles will be clockwise from North), the significant wave height was 0.80 m, the dominant wave was propagating to 328°, the dominant wave length was 54 m, the SAR incidence angle was 19° and the SAR was looking toward 279°;
- For 10 June, the wind speed was ~6 m/s, the wind was blowing to 25°, the significant wave height was 0.62 m, the dominant wave was propagating to 332°, the dominant wave length was 61 m, the SAR incidence angle was 32° and the SAR was looking toward 279° from North.

Note that the wind speed, wind direction, wave direction, wave length were essentially the same between the two images, though the significant wave height was slightly decreased for 10 June. The biggest different is the change in SAR incidence angle; 20° versus 32°.

From the buoy data the dominant wave direction and the wind direction are not the same, indicating that we have both a wind-wave and swell-wave component. The SAR imagery also clearly shows a swell-wave component propagating in the same direction as indicated by the buoy data. In order to separate the total significant wave height (which the buoy records) into its wind and swell components, we estimate the wave height variance of the dominant swell wave from the SAR image modulations (see (Wackerman, 2021) for details on how this is done). We got 0.023 m^2 for 09 June and 0.011 m^2 for 10 June. Since we are using the Elfhouhailly wind wave spectrum which has both wind speed and fetch as inputs, we use the buoy-measured wind speed and then adjust the fetch until the total significant wave height (from both wind and swell waves) matches the buoy-measured value. This gave a fetch of 50,000 m for 09 June and 38,000 m for 10 June.

Figure 15 shows the two SAR images. They have been re-mapped to a common latitude/longitude grid with North up. They have been median-flattened (i.e. a median filter is

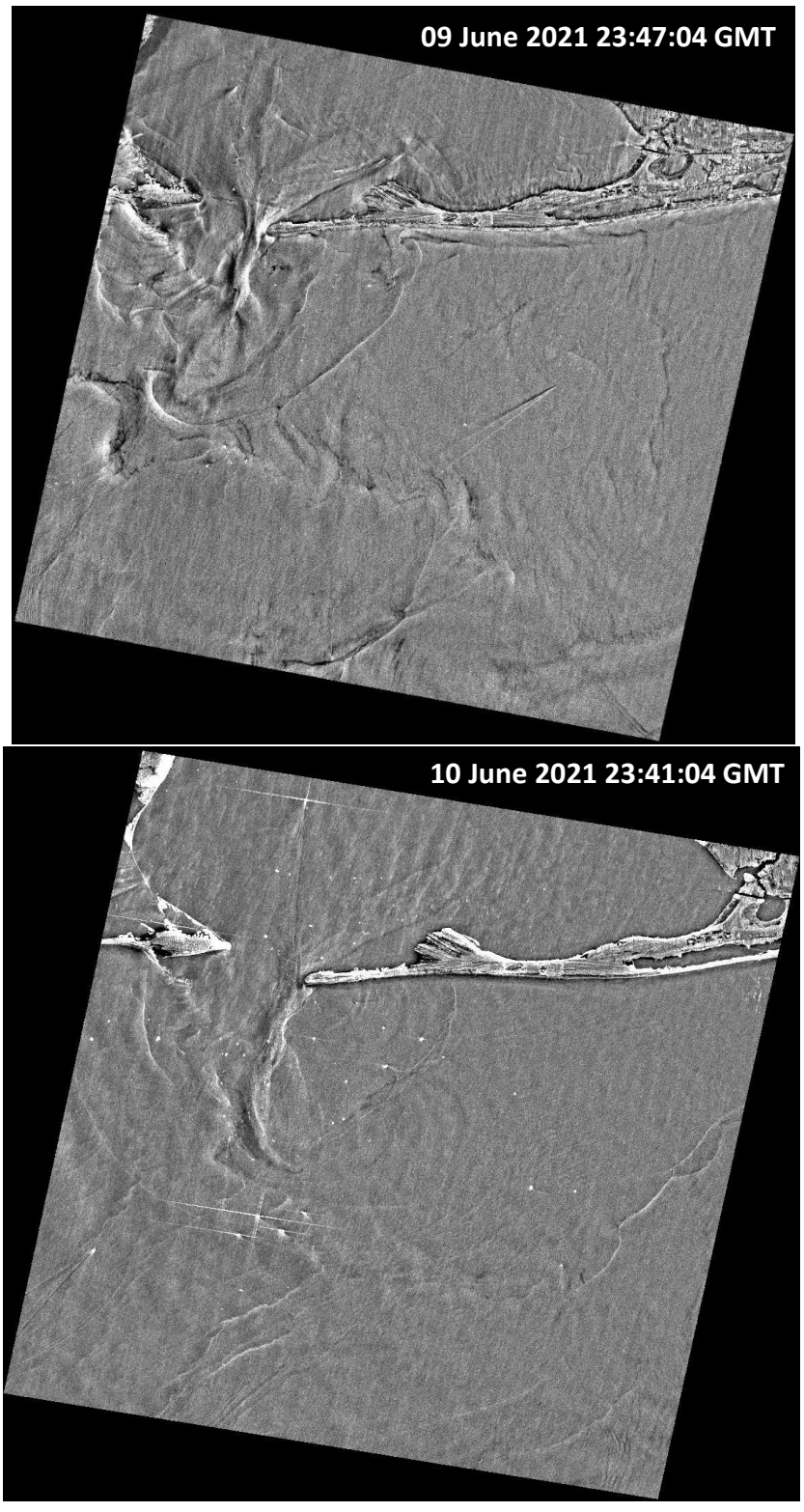

Figure 15: Two SAR image to be used in the analysis.

run over the image and at each location the image is divided by the local median) to bring out the modulation features. The top image is 09 June and the bottom image is 10 June.

Figure 16 shows the SAR images in red, with the model currents mapped to the SAR image in blue. The blue image is the model surface current gradient, and what we want to see is the locations of the model gradients line up with locations of frontal features in the SAR imagery. For the 09 June image (top) the two frontal features that are propagating to the South-East out of the bay are pretty well aligned with corresponding SAR frontal features. For the 10 June image (bottom), the long feature propagating to the South-East is somewhat further away from a SAR frontal feature further down in the image. In general we do not expect the model and SAR fronts to exactly align, since the propagation of the fronts in the model depend on environmental parameters that are not completely known. However, they appear to be close enough that we can assign a SAR feature to most of the major frontal features in the model results.

Figure 17 shows the RCS modulations that we extracted from the 09 June. We extracted cuts across the frontal features at various locations (marked as red lines in the figure) in the median-flattened image and normalized the mean value away from the feature to 1.0. For each plot we decreased the SAR speckle noise by averaging a short distance along the front. The resulting plots are shown as insets in the figure and labelled L1 through L4 corresponding to the same labels next to the red lines in the figure. The peak normalized RCS values range from 1.4 to 2.0 for the bright fronts (so 0.4 to 1.0 in modulation) and around 0.65 for the dark front (so -.35 in modulation). The figure also shows the SAR look direction (in these images it is always down; i.e. top to bottom) as an orange arrow, the direction the wind is blowing to as a yellow arrow, and the direction that the peak spectral wave is moving to as a pink arrow.

Figure 18 shows similar RCS data for the 10 June image. Here the bright signature peaks go from 1.2 to 1.4 (so 0.2 to 0.4 in modulation), within one of them (L1) going to 1.7 (0.7 in modulation). The dark signatures are generally around 0.7 (so -0.3 in modulation). The METOC conditions were essentially the same, so the same wind and wave arrows are shown on this figure along with the SAR look direction.

In the images in Figures 17 and 18, the SAR look direction is down (i.e. from top to bottom) so we can determine the SAR look direction with respect to being perpendicular to the front for each of the plots. The peak RCS versus SAR look angle from being perpendicular is shown in Figure 19. For this figure an angle of 0 degrees means that the SAR is looking orthogonal to the front orientation into the Bay. For both of these images the wind direction is approximately 106 degree rotated from the SAR look direction and the dominant wave direction is approximately 55 degrees rotated from the SAR look direction. We can see from Figure 19 that there is not much difference in the modulations from the two images when considering the SAR look direction for each cut. The larger modulations from the 09 June image are coming from cuts which are much closer to the SAR look being perpendicular than we have in 10 June. We do have a very large modulation (~1) from 09 June that appears to be different than the others. We performed a least-squared fit of a quadratic polynomial on all the RCS modulations other than the large 1.0 modulation. That fit is shown as the black dashed line and it fits the data well.

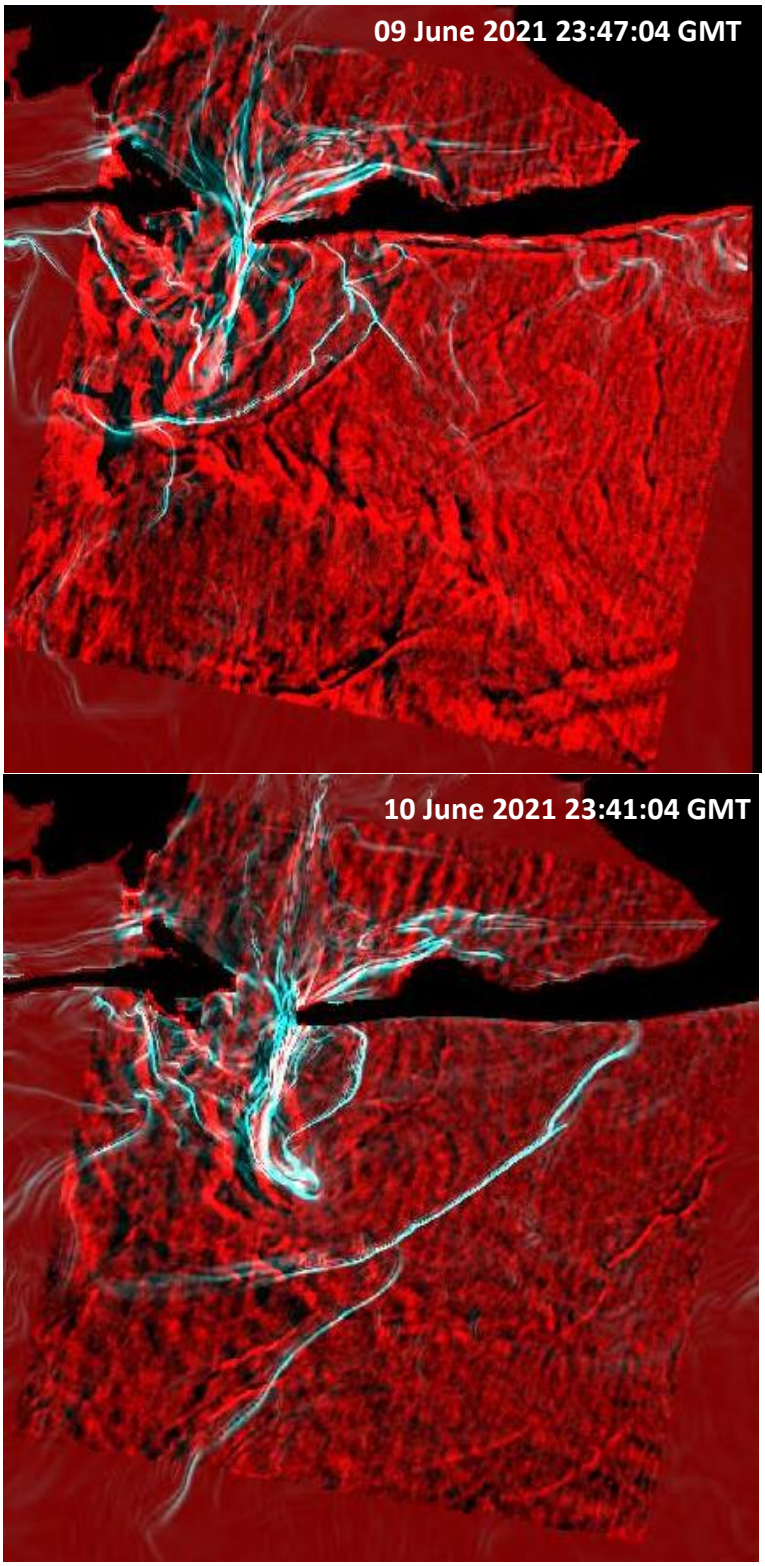

Figure 16: SAR images (red) and WHOI surface current model gradients (blue).

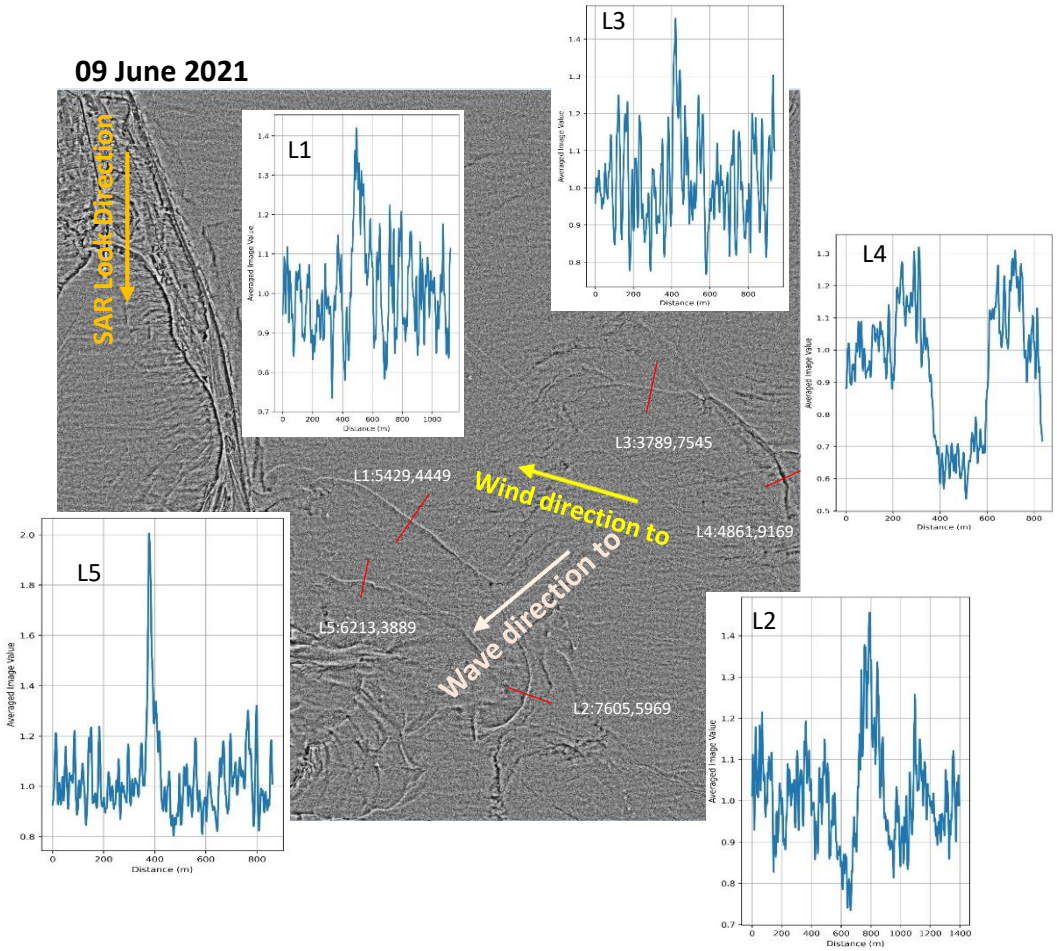

Figure 17: Plots across frontal features from 09 June SAR image. Each cut plot is labelled with L# and in the SAR image the location of the cuts is shown with a red line and labelled with its associated L# value. The numbers that follow this are the line, column value in the image for the middle of the plot. The SAR look direction, wind direction to, and wave direction to are shown in the image.

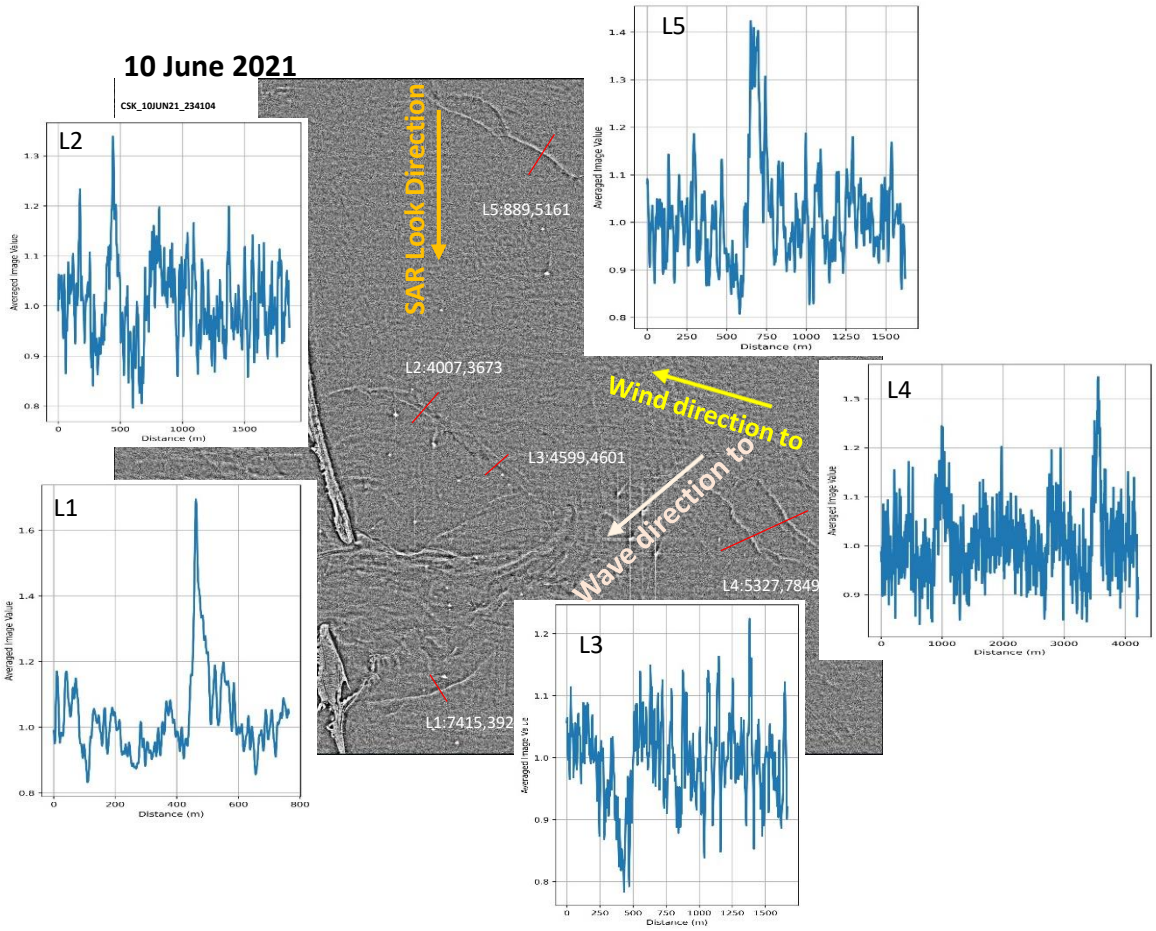

Figure 18: Plots across frontal features from 10 June SAR image. Each cut plot is labelled with L# and in the SAR image the location of the cuts is shown with a red line and labelled with its associated L# value. The numbers that follow this are the line, column value in the image for the middle of the plot. The SAR look direction, wind direction to, and wave direction to are shown in the image.

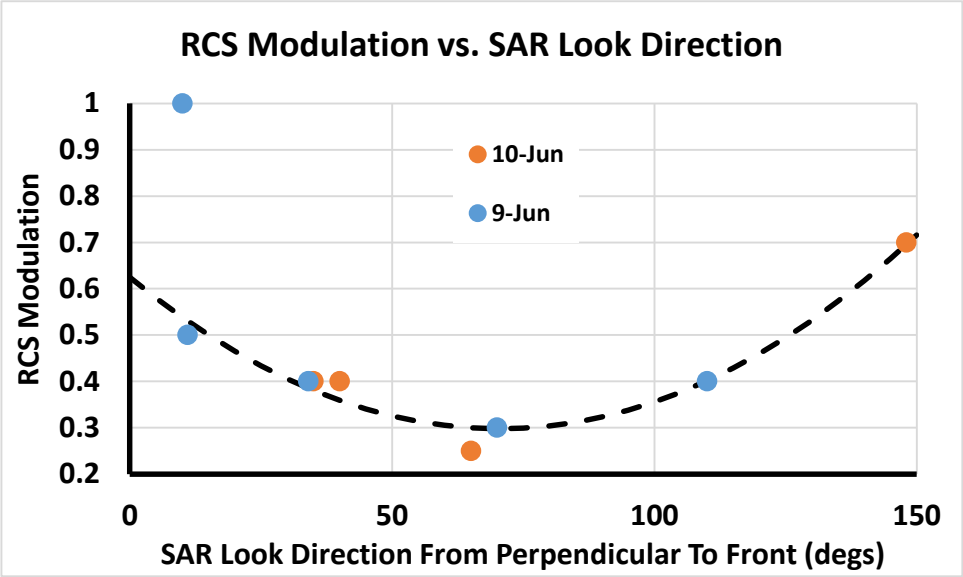

Figure 19: Summary of RCS modulations from the two SAR images, plotted as a function of the angle of the front with respect to the SAR look direction. Dashed line is a quadratic fit to the data without the large value of 1 in the upper, left.

To get a sense of what the currents are across these fronts from the models, we performed a similar extraction on the model current data. Since the model and current fronts are not in the same place (see Figure 16) we extracted the current data strictly from the model current files. From Figure 16 the SAR/model comparisons on 09 June are the closest, and it seems clear which model current front should be mapped to which SAR frontal signature. Figure 20 shows the resulting plots across the fronts. The upper image shows the model current magnitude for the 09 June model data coincident with the SAR image collection and the red lines show the location of the cuts (with a label for each). The plots below the image are the currents along the cuts. In each case, the currents were rotated to be the current orthogonal to the local orientation of the front (we called this the u current and is the left plot for each cut) and the current in the direction of the local front orientation (we called this the v current and is the right plot for each cut). For each current cut we calculated the mean and standard deviation for a short distance along the front. In each current plot in Figure 20 the solid line is the mean current and the dotted lines are ± one standard deviation from the mean. We wanted to test that the model currents were the same with respect to the frontal orientation locally for each cut; which means that we wanted the ± one standard deviation curves to lie on top of the mean curves. Note that for the u-current they do, and for the v-current they are close. Generally, the u-currents in Figure 20 have approximately a 0.1 – 0.2 m/s change across the front (with a decrease as we head toward the Gulf). If we use the change in the u-current to define the location of the front (i.e. the front is where the u-currents in the left plots have the essentially vertical drop), then for the L5 and L1 cuts the v-current is much smaller across the front than the u-current. For the L5 cut it is essentially zero and for the L1 cut it is around .02 m/s. So for these cuts to first order the model is indicating a surface current that is constant along the front, has a u-current across the front that changes by ~0.1 – 0.2 m/s, and has a v-current of zero. The L2 cut is a little different since the

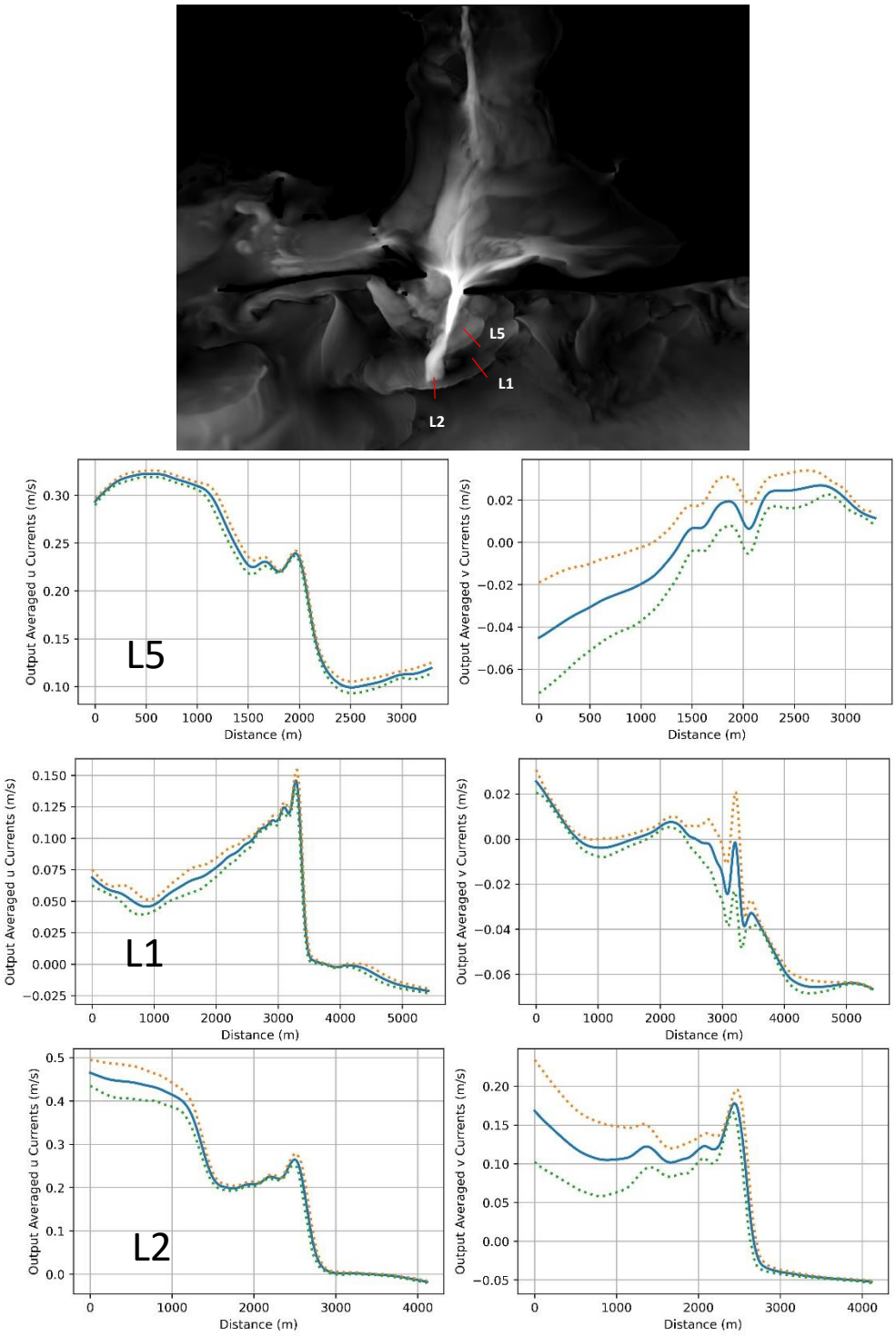

Figure 20: Cuts through the surface current model results from the WHO model for 09 June. Top image is the current magnitude and shows the location of the plots. For each plot the left plot is the u-velocity defined as the velocity in the direction of the cut, and the right plot is the v-velocity defined as the velocity in the orthogonal direction.

v-current changes by 0.1 m/s across the front while the u-current changes by 0.2 m/s. But note that in the top image, the L2 cut is right where the shipping channel is emptying into the Gulf, so this may not be characteristic of the other fronts (such as the L1 and L5 cuts).

Figure 21 shows similar plots for the 10 June image. Cuts L1 and L3 are very similar to the 09 June currents; a u-current change around 0.2 m/s and a v-current change very close to zero. However cuts L2 and L4 across the further front are different. The change in the u- and v-velocities are about the same magnitude, indicating that the current was not moving orthogonal to the front orientation, but at approximately a 45 degree angle. The is borne out if one looks at the model current vectors; they point approximately horizontally to the right at this location. Note that the SAR frontal signature is approximately mid-way between these two current fronts (Figure 16) so it is not clear which model front to map the SAR signature to.

As we have noted above, the current gradient is very important in estimating the RCS modulations, not just the change in current. Based on the cuts in Figures 20 and 21, the change in u-current (i.e. from 0.2 m/s to 0 m/s) appears to occur over approximately a 300 meter distance (give or take 100 meters or so).

Based on these results we built a simplified generic frontal model to determine the relationship between RCS modulation and frontal current changes. Figure 22 shows the geometries for the front. The positive x-axis goes to the right, the positive y-axis points upward. The u-velocity is the velocity along the x-axis and the v-velocity is the velocity along the y-axis. We will set all the v-velocities to zero. The u-velocity has a constant value, u_0, for $x>d_0$, and is zero for $x<-d_0$. Within the range $x=[-d_0,d_0]$ the u-velocity changes linearly from u_0 to zero. This is meant to model the frontal signatures moving out of the Bay, so as noted in the figure the Bay is considered to be on the right side of the figure (positive x) and the Gulf is on the left side (negative x). Below we will introduce a swell wave component into the model; this will be a wave coming from the Gulf (coming from negative-x). Thus this model has two parameters: u_0 and d_0. Note that d_0 is the half-width of the front; the u-velocity goes from u_0 m/s to 0 m/2 over a distance of $2*d_0$. Based on the cuts in Figure 20, we set $u_0=-0.2$ (note that it has to be a negative value since the u-velocity is coming out of the Bay) and generated RCS modulations across the front for values of d0 of 50m, 100m, 200m, 300m, 400m. As noted above the wind and wave directions are rotated from the SAR look direction by approximately 106 and 55 degrees respectively for both images, so we need to rotate them by the same amount in order to simulate fronts at different angles within the SAR image. We indicate this in the figure by showing three sets of arrow triplets for three different rotations. In the simulations below we wet the wind direction to 0, -30 and -60 degrees (with the wave and SAR look directions rotated appropriately). We looked at incidence angles of 20 degrees for the 09 June case (with its associated wind-wave and swell-wave parameters) and 32 degrees for the 10 June case (with its associated wind-wave and swell-wave parameters). Based on the results from Section 5 (validations against the historical internal wave data) we ran WABE in three different modes: (1) RHS with viscosity terms using the high beta; (2) RHS with viscosity terms using the low beta; and (3) RHS without viscosity terms using the high beta. Remember that for the internal wave validation, both options (2) and (3) generated RCS modulations consistent with the published values.

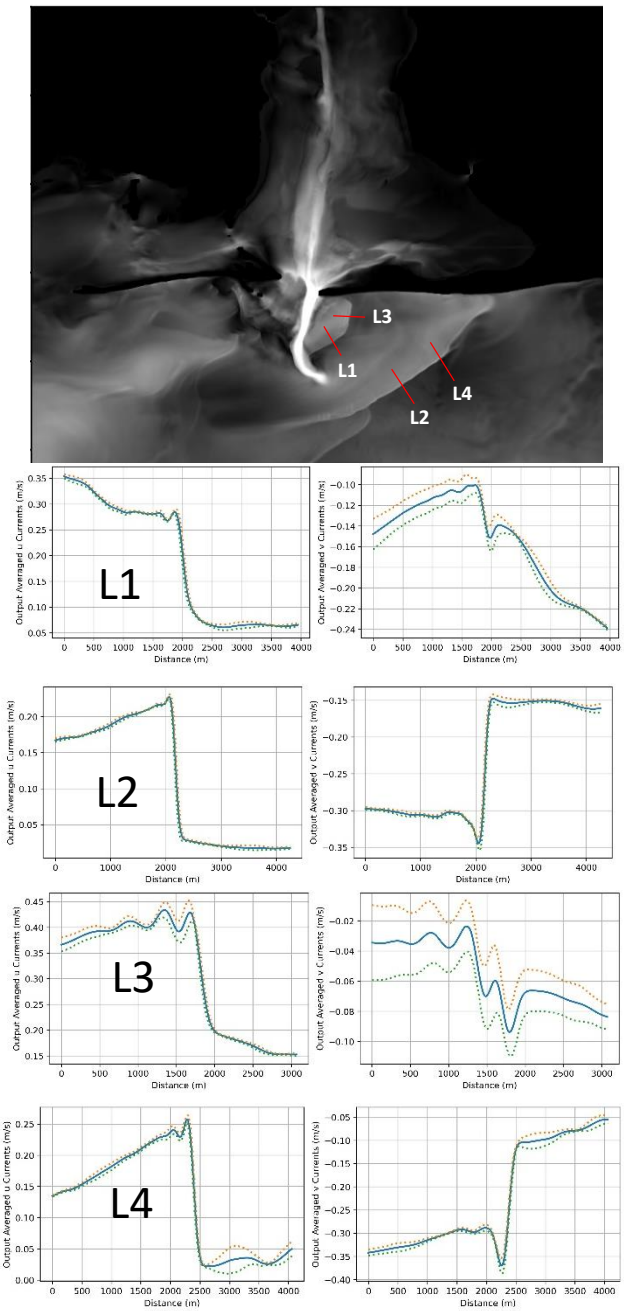

Figure 21: Cuts through the surface current model results from the WHO model for 10 June. Top image is the current magnitude and shows the location of the plots. For each plot the left plot is the u-velocity defined as the velocity in the direction of the cut, and the right plot is the v-velocity defined as the velocity in the orthogonal direction.

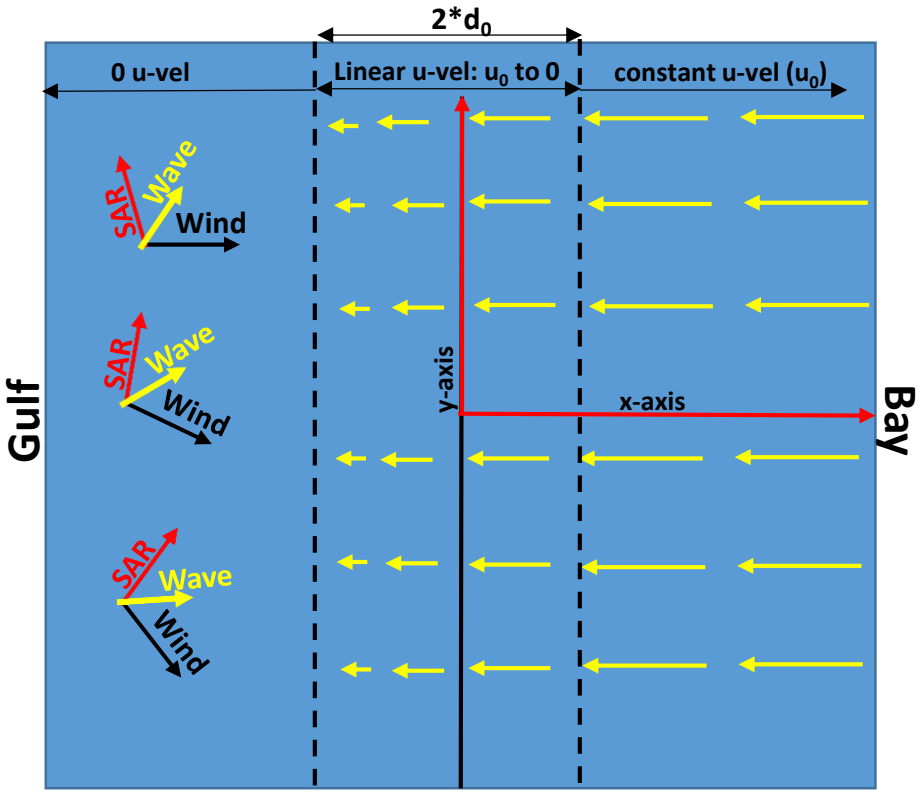

Figure 22: Schematic showing the geometry for our generic front model.

Figure 23 shows the results for an incidence angle of 32 degrees (the value for 10June) using the V-Acc breaking wave model with a threshold of -0.3g (this was the model that gave the best results compared to the internal wave validation study in Section 5). For this comparison we did not include a swell wave component. The plots in Figure 23 are similar in format to what was shown above in Section 5 with the changes that the legend is no longer shown in the upper,right plot (so the plots can be seen), and in the lower, right plot we are plotting RCS peak modulation versus file number instead of du/dx. The different file numbers correspond to the difference WABE runs and d_0 values. In the top plots in Figure 23 we have circled the RCS modulations that came from the three different WABE runs: file number 0-4 use the RHS with the viscosity terms and the high wind growth (Beta) model; file numbers 5-9 use the RHS with the viscosity terms and the low wind growth model; file numbers 10-14 use the RHS without the viscosity terms and the high wind growth model. Within each ellipse, the results are in the order of d_0=50, 100, 200, 300, 400 meters so that as d_0 increases the RCS modulations decrease (which makes sense since the current gradient is decreasing). One interesting result from Figure 23 is that including or removing the viscosity terms in the RHS make no difference in the output RCS modulations. This is different than what we saw with the internal wave cases. This may be due to the fact that for these frontal simulations the spatial extent of the current change is significantly smaller than for the internal wave simulation and so there is not enough time for the viscosity terms to have significant effects. However note that the low beta case provides

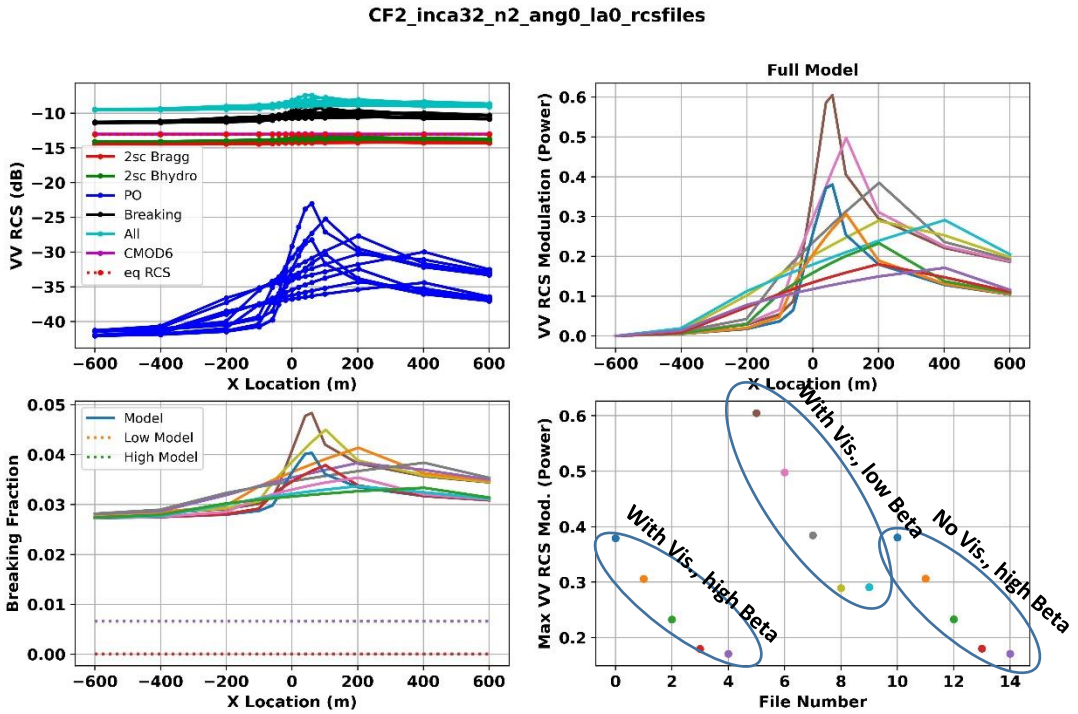

Figure 23: RCS model results for the generic front model and for various WABE RHS values. For these results u0=-0.2 m/s and d0 had values of 50, 100, 200, 300, 400 meters (these are the 5 results within each ellipse in the lower, right plot). Format of the plots is the same as in previous figures.

significantly higher RCS modulations (as we also saw with the internal wave simulation) that is more consistent with what we extracted from the SAR imagery. Also note that the last two RCS modulations are essentially the same. These correspond to frontal half-widths of 300m and 400m respectively and we found in general that the RCS modulations do not change after a half-width of 300m.

Figure 24 shows the final simulations for 09 June (top set of plots) and 10 June (bottom set of plots). These have both wind and swell wave components (estimated as discussed above) using the WABE solution with the low beta case and viscosity terms in the RHS. The RCS model parameters come from the validation in Section 3: the wind wave spectrum uses the Elfhouhailly et al. wavenumber model with the Romeiser et al. angular model; the scale factors are s_H=2.0, s_{PO}=1.3, s_{Br}=0.8; the breaking wave model is the V-Acc model with a threshold of -0.3g. Results are shown for three different wind directions (0°, -30°, -60°) where the wave and SAR look directions were rotated accordingly. Thus these should represent RCS modulations across frontal features in the SAR image where the front orientation is such that the wind direction is orthogonal to the front (wind direction of 0°, which is approximately L2 in Figure 17), or the front orientation is rotated 30° from this counter-clockwise (in terms of the images shown in Figures 15-18), or rotated 60° (which is around L1, L3, and L5 in Figure 17). The RCS peak

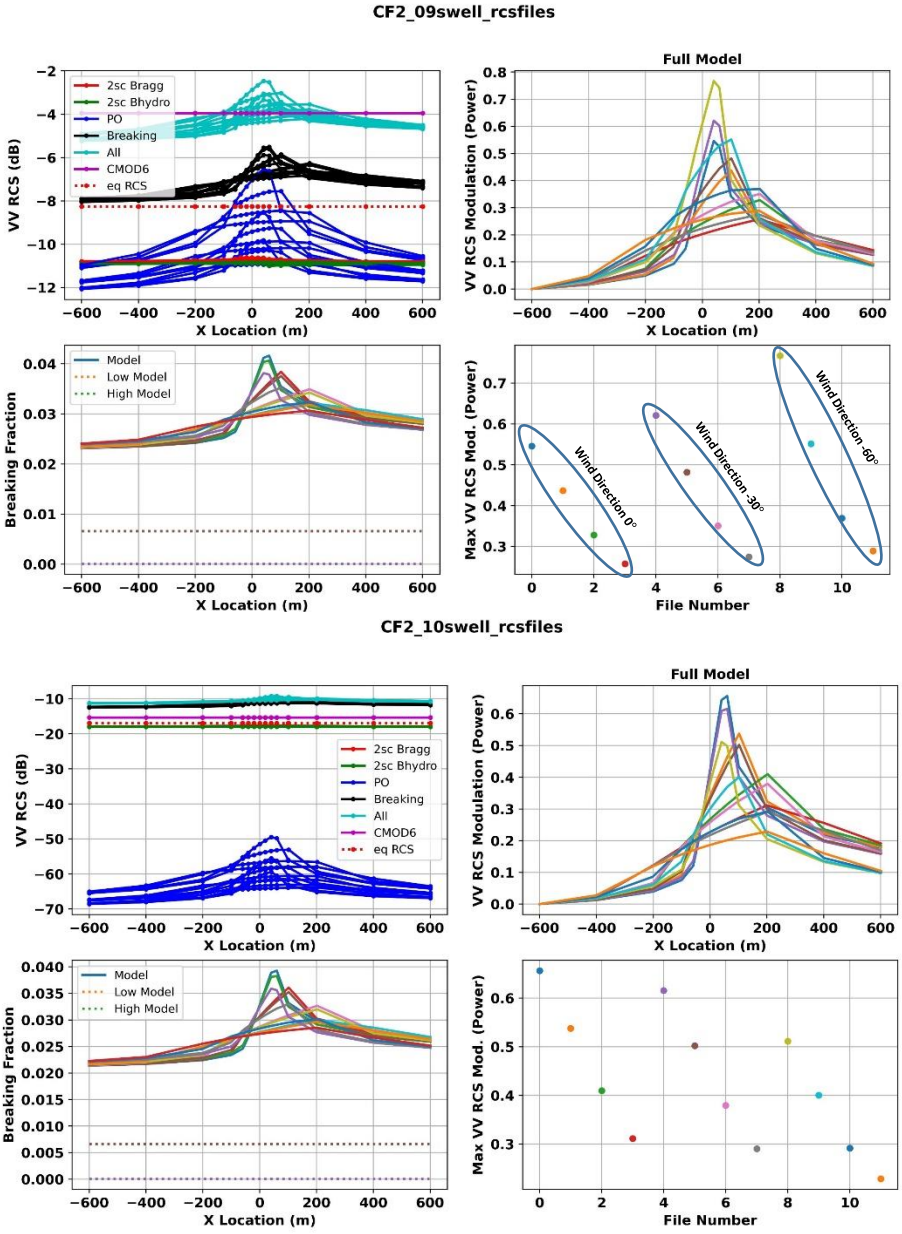

Figure 24: Final simulation results for 09 June (top set of plots) and 10 June (bottom set of plots) for various values of d0 (50,100,200,300 meters, results within each ellipse) and different directions for the wind with respect to the front orientation (0°, -30°, -60°). Format for each set of plots is the same as in previous figures.

modulations are shown in the bottom, right plot of each set, and the top set (for 09 June) has the RCS modulations from each wind direction circled and labelled. Within the wind direction ellipses the different RCS modulations come from different values of the front half-width, d_0; 50m, 100m, 200m, 300m, respectively.

For 09 June, the low incidence angle (20 degrees) means that the Physical Optics (PO) term is important (the blue component lines in the upper, left plot). This is why the RCS modulations increase as the wind direction rotates more negative; more negative wind direction means the SAR look direction is becoming more orthogonal to the front, which is the angle that causes the PO term to be largest. For 10 June the RCS modulations decrease as the wind direction becomes more negative because the PO term is too small to have any contribution.

The plots of RCS modulations (upper, right plots for each date) for the larger frontal widths have the wrong shape. It is much wider than what we see in the SAR image plots in Figures 17 and 18 where the RCS modulation peak has a width of 100 – 200 meters. Thus from the shape of the RCS modulations alone it appears that we need a small frontal width. So we start with d0=50m and u0=-0.20 and make runs for each of the cuts from the 09 and 10 June images. We then modify the frontal parameters until we get a good fit. Figure 25 shows the comparisons between the image cuts and the model outputs for the best sets of parameters derived visually, with the frontal parameters listed at the top of each plot. All of the RCS modulation plots (both data and model) are normalized by subtracting the local minimum value so that they go to zero on one side of the modulation plot.

The fits are pretty good between the model and the data for the results in Figure 25; both the peak RCS and the general shape of the main lobe. Thus it appears that this model is able to reproduce the RCS modulations well given the correct frontal parameters. But that is probably true of any reasonable model, so the question is whether the resulting frontal characteristics are correct. Although we do not have in situ ground truth of the surface current change across the fronts, note that the current change in the fronts that generate the best fit are all between 0.1 and 0.2 m/s; which is exactly the range that the WHOI surface current model results were within. In other words, our model generates the same current gradients that the WHOI model generates, so the two models are very consistent. However, our model generates frontal widths that are significantly smaller than the WHOI model results. Our full-widths vary between 50m and 100m whereas the WHOI model results had front full-widths around 300m. However, as mentioned above, this is probably an erroneous comparison since the WHOI model was run with a coarse resolution which limited how small the front could be.

For two locations of the SAR cuts in the 09 June image (labelled L1 and L2 in both the SAR image cuts in Figure 17 and the WHOI model velocity cuts in Figure 20), and one location for the 10 June cuts (The L2 cut in the SAR image in Figure 18 and the L3 cut in the WHOI currents plots in Figure 21) we can make a reasonable assumption to connect the SAR frontal feature to the model frontal features. For these three locations, Figure 26 shows the WHOI model currents across the fronts versus the SAR-derived current. Our current model has the v-velocity (the velocity along the front orientation) set to zero, and the SAR RCS modulations are independent

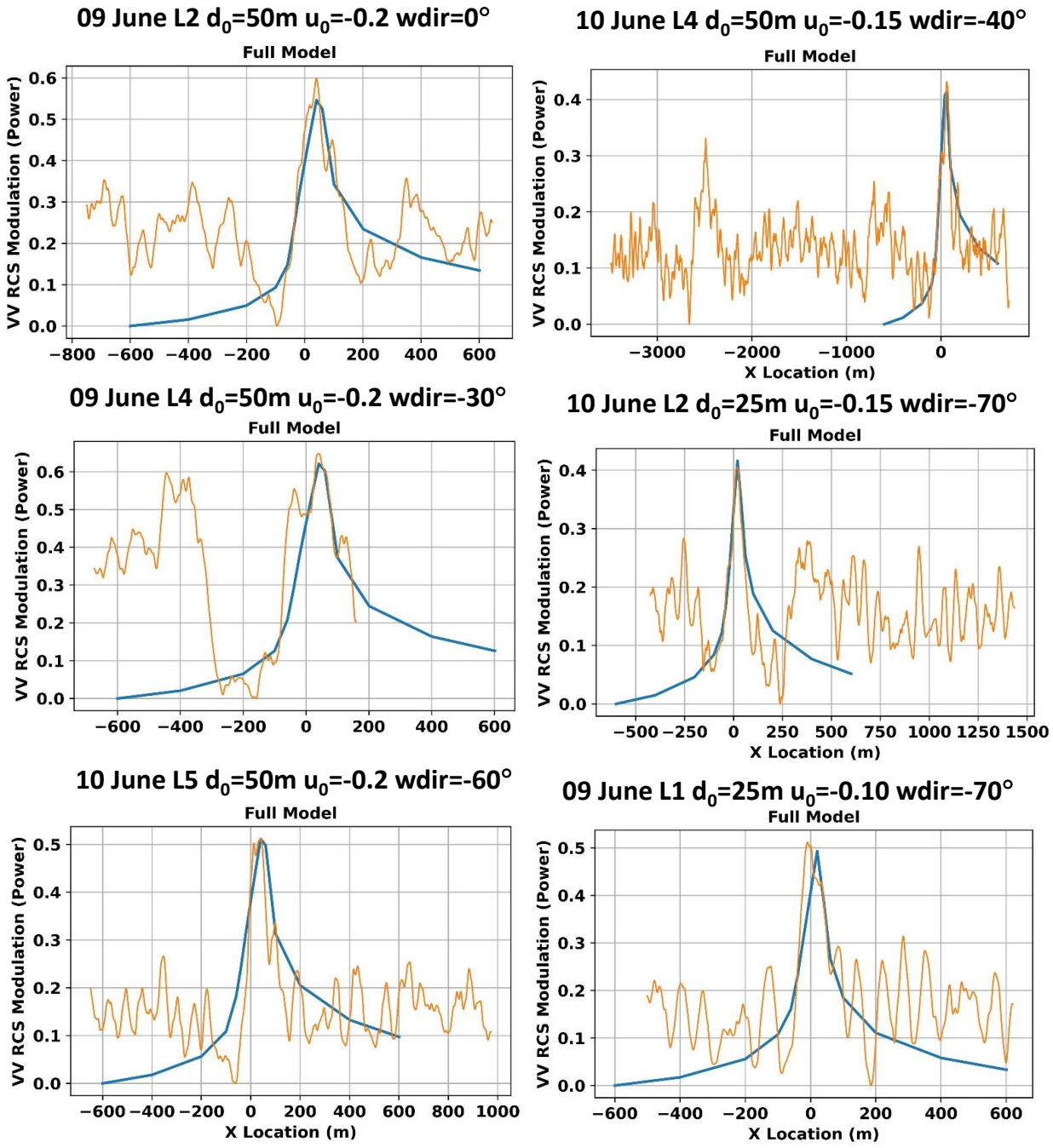

Figure 25: Final model results finding frontal parameters that allowed the model RCS modulation (blue line) to match the SAR image data RCS modulation (orange line). Six plots are for six of the cuts taken from the 09 June and 10 June SAR image; the cut label is indicated in the title of each plot. The resulting frontal parameters that generated the best fit are also indicated in the title. All of these results are normalized by setting the minimum value to zero

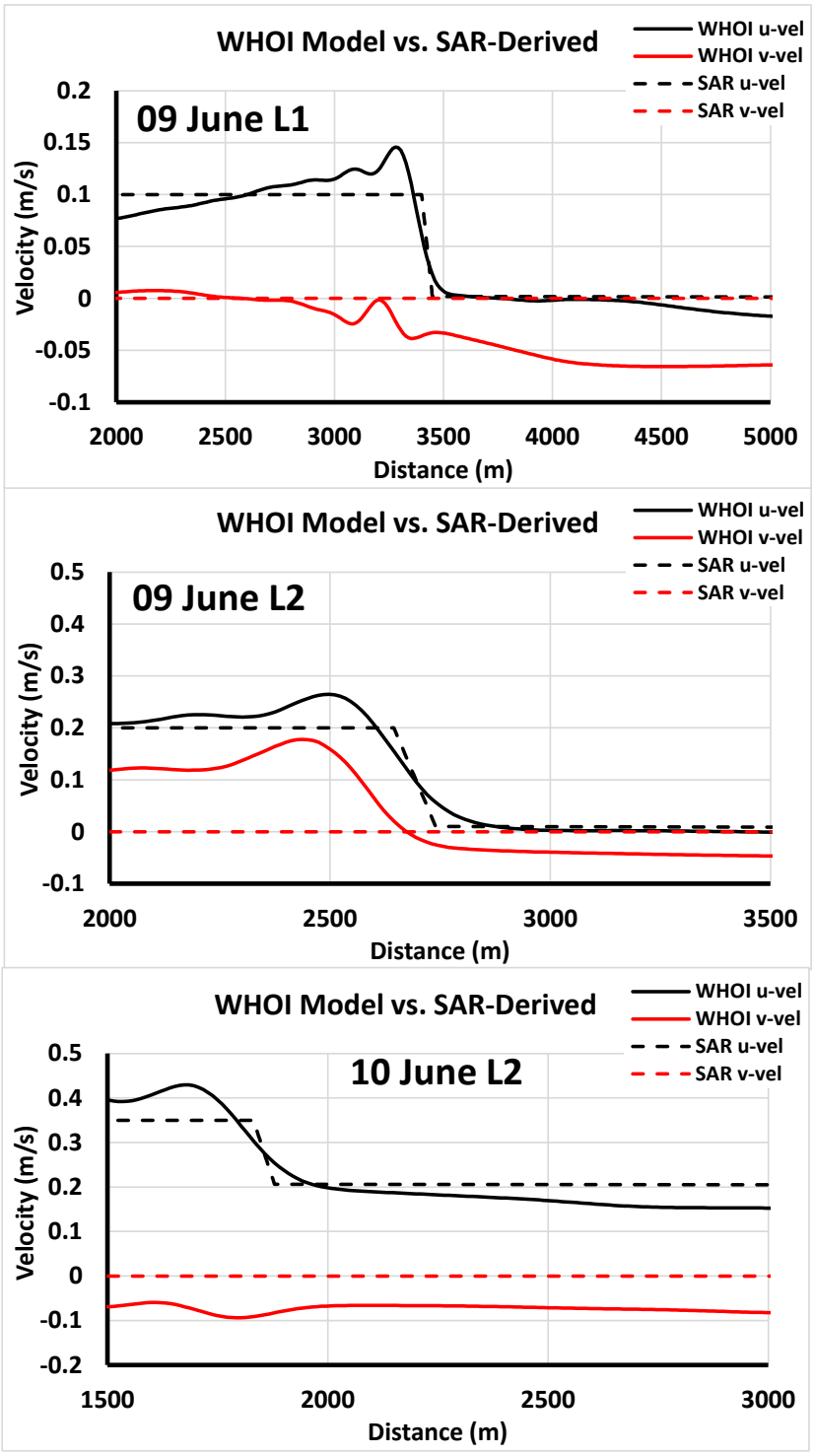

Figure 26: Comparison of the WHOI model currents (black and red solid lines) to the SAR-derived currents (black and red dashed line). The SAR current model has the v-velocity set to zero and is independent of a constant velocity bias, so this is a comparison of the u-velocity gradients. They agree to within 0.05 m/s.

of a constant velocity bias across the entire scene, so these comparisons are only for the u-velocity (the velocity orthogonal to the frontal orientation) change across the front. For all three cases the match between the WHOI and SAR results is very close; within 0.05 m/s. Thus to the extent that the WHOI model is "truth", the SAR frontal signatures appear to be able to generate accurate estimates of the current gradient across the front.

The normalization used for the results in Figure 25 can introduce some noise into the outputs since the location of a minimum point in the data cuts is a random process. Another normalization method is to make the mean of the data cuts outside of the frontal signature hover around zero (not that by construction the model result goes to zero on the left side of the plot; i.e. where the waves are coming from and the current is zero). Figure 27 shows the resulting fits with this normalization for three of the cuts in Figure 25, and shows that with this normalization there is a slight decrease in the frontal parameters: for 09 June L2 (top plot) d_0 stayed at 50m but u_0 decreased from -0.20 to -0.15 m/s; for 10 June L5 (middle plot) d_0 decreased from 50m to 25m and u_0 decreased from -0.20 to -0.13 m/s; and for 09 June L1 (bottom plot)) d_0 stayed at 25m but u_0 decreased from -0.10 to -0.08 m/s. But generally between the two normalizations we still have current gradients between 0.20 and 0.10 m/s and current full-widths between 50m and 100m, so the changes are minor. However the first normalization does appear to fit the WHOI model results better (Figure 26) since the second normalization decreases the u-velocity gradient.

7. Discussion and Next Steps

Under the current version of the tool we need to assume a functional form for the current field that has some set of parameters that determine the final currents. We then modify the parameters until we get a good fit with the data. Thus we get the best fit for that functional form; we are not finding the current field in general that minimizes the error with the imagery. To the degree that the function form we choose mimics reality we will get a good current output, but if it does not then we may still get a good fit to the imagery but not be retrieving the real current field. For the results shown in Section 6, our assumption that the v-velocity is zero is probably incorrect based on the WHOI model results so we are not generating the most accurate output currents with the model we assumed. We should add either a constant v-velocity (and thus another parameter) or some changing v-velocity field (and potential more additional parameters). In addition, since we are changing the parameters manually to determine the best fit, we also really need a functional form with a small number of parameters where each parameter controls an aspect of the signature. For the results discussed in this report, we only had two parameters for our current model; one essentially determined the width of the RCS modulation (the frontal width) and the other the peak of the RCS modulation (the current gradient). Thus it was relatively easy to find the best fit parameters. To be able to move to more complicated functional forms with more parameters we will need to implement an automated process to search for minima, and we would have to include the option of finding a family of solutions since the more parameters we have the more of a chance that different values will generate the same RCS modulations; i.e. the error function has multiple minimum of similar depth. Of course one end of this spectrum is just to have the parameters be the current values themselves at each spatial location, in which case we are directly estimating the current field, but have probably maximized the problem of multiple minima and a large family of solutions.

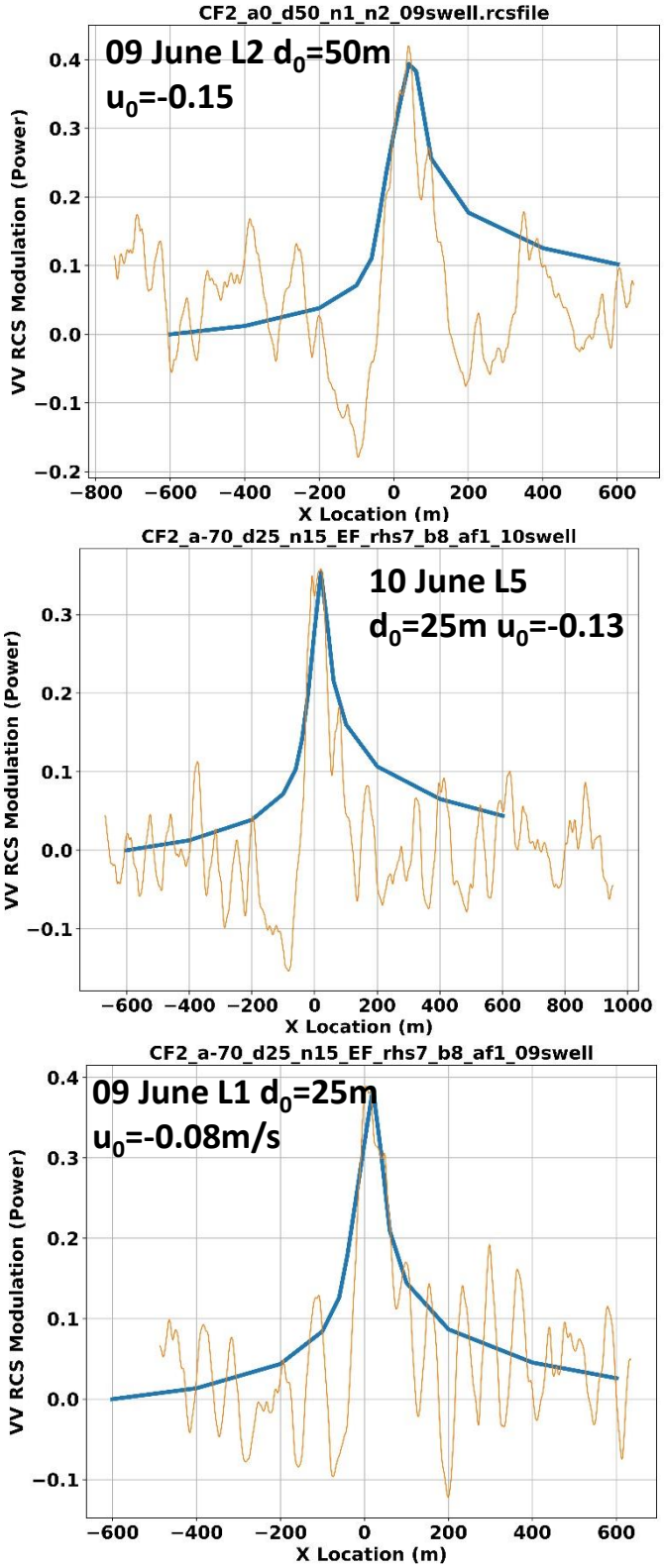

Figure 27: Final results for three of the image cuts from Figure 26, but normalized by setting the data background mean to zero. The resulting frontal parameters changed only slightly.

In examining the RCS modulations from the model in Figures 25 and 26, it does appear that we are dissipating energy as quickly as we should. The model RCS modulations have tails into the positive x-axis that are too high compared to the data. Note that the tail coming from the negative x-axis appears to be close to being correct; this is where the waves are first encountering the current. There are a number of reasons this could be happening. It may be that the perturbation model that we have adopted for the RHS of the WABE equations is not dissipating sufficient energy. To solve this we would have to move to the physics-based form of the RHS and directly incorporate energy dissipation from breaking during the solution of the WABE. To do this with the ray-trace solver will take some research since we do not have the full wave spectrum available at each wavenumber/time step. We anticipate requiring some form of an iterative solution that estimates the wave spectra, then uses those full spectra in the next iteration to derive the required parameters and re-estimates the spectra, and continue this until we reach some stopping criteria. In addition, it has been shown (Lyzenga, 2010) that the non-linear transfer of energy, particularly from long waves to shorter waves, can significantly change the RCS modulations across a current front. Thus we may need to incorporate that term into the WABE solver. Overall, there is some more research for the WABE solver in order to understand how to increase energy dissipation across the current field. However, it is not clear how this will affect the peak value of the RCS modulation, which is what we are essentially using to fit to the data. If it does not affect the peak value, it may not be worth the effort since what we are going for is an accurate current field.

The WABE solver we currently have takes a long time to run; generation of the wave spectra for one set of current parameters can take around 3 hours. For the results in this report, the simple current model allowed us to quickly find a set of parameters that fit the SAR imagery with only a few runs. If we implement a more complicated model with a minima search (and/or implement the physics-based RHS with an iterative algorithm for energy dissipation) then we will significantly increase the number of WABE runs required to get to the solution. This will rapidly become untenable, so we need to find a way to decrease the run time for the WABE solver. We already have parallelized the solver so that it uses a different CPU for each spatial location, so we will need to look more carefully at the computational implementation and see if we can provide any significant speed-up.

REFERENCES

Alpers, W.R., "Theory of radar imaging of internal waves," Nature, 314,245-247, 1985.

Anguelova, M.D., F. Webster," Whitecap coverage from satellite measurements: a first step toward modeling the variability of oceanic whitecaps," J. Geophys. Res., 111, doi:1029/2005JC003158, 2006.

Apel, J.R., "An improved model of the ocean surface wave vector spectrum and its effect on radar backscatter", J. Geophys. Res., **99**, 16269-16291, 1994.

Baldock, T.E., P. Holmes, S. Bunker, P.Van Weert, "Cross-shore hydrodynamics within an unsaturated surf zone," Coastal Engineering, **34**, 173-196, 1998.

Battjes, J.A., J.P.F.M. Janssen, "Energy loss and set-up dues to breaking of random waves," Proc. Sixteenth Coastal Eng Conf., Vol. 1, 569-587, 1978.

Battjes, J.A., M.J.F. Stive, "Calibration and verification of a dissipation model for random breaking waves," J. Geophy. Res., **90**, 9159-9167, 1985.

Collins, J.I., "Prediction of shallow-water spectra," J. Geophy. Res., **77**, 2693-2707, 1972.

Cox, C., W. Munk, "Statistics of the sea surface derived from sun glitter," J. Mar. Res., vol. 13, no. 2, 198-227, 1954a.

Cox, C., W. Munk, "Measurements of the roughness of the sea surface from photograms of sun;s glitter," J. Opt. Soc. Am., 44(11), 1954b.

Dally, W.R., R.G. Dean, R.A. Dalrymple, "Wave height variation across beaches of arbitrary profile," J. Geophy. Res., **90**, 11917-11927, 1985.

Donelan, M., W. Pierson, "Radar scattering and equilibrium ranges in wind-generated waves with application to scatterometry," J. Geophys. Res., **92**, 4971-5029, 1987.

Elfouhily, T., B.Chapron, K.Katsaro, D. Vandermark, "Uunified directional spectrum for long and short wind driven waves," J. GEophys., Res., 102, 15,781-15,796, 1997.

Ericson, E.A., D.R. Lyzenga, D.T. Walker,"Radar backscattering from stationary breaking waves," J. Geophys. Res., 104, 29,679-29,695, 1999.

Feindt, F., V. Wismann, W. Alpers, W.C. Keller, "Airborne measurements of the ocean radar cross section at 5.3 GHz as a function of wind speed," Radio Science, **21**, 845-856, 1986.

Fu, L.L. and B. Holt, "Some examples of detection of ocean mesoscale eddies by the Seasat synthetic aperture radar," J. Geophy. Res., 88, 1844-1852, 1983.

Gellert, W., H. Kustner, M. Hellwich, H. Kastner, The VNR Concise Encyclopedia of Mathematics, Van Nostrand Reinhold Company, New York, New York, 1975.

Haller, M.C., D.R. Lyzenga," Comparison of radar and video observations of shallow water breaking waves," IEEE Trans. Geosc. Remote Sens., 41, 832-844, 2003.

Hasselmann K., T.P. Barnett, E. Bouws, H. Carlson, D.E. Cartwright, K. Enke, J.A. Ewing, H. Gienapp, D.E. Hasselmann, P. Kruseman, A. Meerburg, P. Mller, D.J. Olbers, K. Richter, W. Sell, and H. Walden., "Measurements of wind-wave growth and swell decay during the Joint North Sea Wave Project (JONSWAP)", *Ergnzungsheft zur Deutschen Hydrographischen Zeitschrift Reihe*, A(8) (Nr. 12), p.95, 1973.

Hasselmann, K., R.K. Raney, W. Plant, W. Alpers, R.A. Shuchman, D. Lyzenga, C.L. Rufenach, and M.F. Tucker,"Theory of synthetic aperture radar ocean imaging: a MARSEN view," J. Geophys. Res., 90, 4659-4686, 1985.

Hauser, D., G. Caudal, "Combined analysis of the radar cross section modulation due to the long ocean waves around 14° and 34° incidence: Implication for the hydrodynamic modulations," Journal Geophy. Res., **101**, 25833-25846, 1996.

Hayes, R.M., "SAR detection of the Gulf Stream", in Spaceborne Synthetic Aperture Radar for Oceanography, edited by R.C. Beal, P.DeLeonibus, and I. Katz, 146-160, John Hopkins Press, Baltimore, Md., 1981

Hersbach, H., "CMOD5 an improved geophysical model function for ERS C-band scatterometry," Technical Memorandum, European Centre for Medium-Range Weather Forecasts, Jan. 2003.

Janssen, P.A.E.M., "Quasi-linear theory of wind-wave generation applied to wave forecasting," J. Phys. Oceanogr., **21**,1631-1642, 1991.

Johannessen, J.A., R.A. Shuchman, O.M. Johannessen, K.L. Davidson, and D.R. Lyzenga,"Synthetic aperture radar imaging of upper ocean circulation features and wind fronts," J. Geophys. Res., 96, 10411-10422, 1991.

Johannessen, J.A., R.A. Shuchman, G. Digranes, D.R. Lyzenga, C. Wackerman, O.M. Johannessen, P.W. Vachon, "Coastal ocean fronts and eddies imaged with ERS 1 synthetic aperture radar," J. Geophys. Res., 101, N0. C3, 6651-6667, 1996.

Kasischke, E.S., D.R. Lyzenga, R.A. Shuchman, C.C. Wackerman, "Contrast ratios of internal waves in synthetic aperture radar imagery: a comparison of SAR internal wave signature experiment observations with theory," , J. Geophys. Res., 93, C10, 12355-12369, 1988.

Keller, W.C., V. Wismann, W. Alpers, "Tower-based measurements of the ocean C band radar backscattering cross section," J. Geophys. Res., **94**, 924-930, 1989.

Komen, G.J., S. Hasselmann, K. Hasselmann, “On the existence of a fully developed wind-sea spectrum,” J. Phys. Oceanogr., 14, 1271-1285, 1984.

Kudryavtsev, V.N., V.K. Makin, B. Chapron, “Coupled sea surface-atmosphere model: 2. Spectrum of short waves,” J. Geophy. Res., **104**, 7625-7639, 1999.

Kudryavtsev V.N., V.K. Makin, “Coupled dynamics of short waves and the airflow over long surface waves,” J. Geophys. Res., **107**, 3209, 2002.

Kudryavtsev, V., D. Hauser, G. Caudal, B. Chapron,” A semiempirical model of the normalized radar cross-section of the sea surface,” J. Geophy. Res., 108, doi:10.1029/2001JC001003, 2003.

Kukulka T., T. Hara, “Momentum flux budget analysis of wind-driven air-water interfaces,” J. Geophys. Res., **110**, C12020, 2005.

Larson, T.R., L.I.Moskowitz, and J.W. Wright, “A note on SAR imagery of the ocean”, IEEE Trans. Atennas Propag., Ap-24, 393-394, 1976.

Lyzenga, D.R., J.R. Bennett, “Full-spectrum modeling of synthetic aperture radar internal wave signatures,” J. Geophys. Res., 93, C10, 12345-12354, 1988.

Lyzenga, D.R., “Interaction of short surface and electromagnetic waves with ocean fronts,” J. Geophys. Res., 96, C6, 10765-10772, 1991

Lyzenga, D.R., “Ocean wave spectrum and dissipation rate derived from CMOD4 model function,” J. Geophys. Res., 109, C07019, 2004.

Lyzenga, D.R., “Effects of nonlinear energy transfer on short surface waves,” J. Geophys. Res., 115, C10001, 2010.

Makin, V.K., V.N. Kudryavtsev, “Coupled sea surface-atmosphere model: 1. Wind over waves coupling,” J. Geophys. Res., **104**, 7613-7623, 1999.

Masuko, H., K. Okamoto, M. Shimada, S. Niwa,”Measurement of microwave backscattering signatures of the ocean surface using X-band and Ka-band airborne scatterometers,” J. Geophys. Res. (Oceans), 91, 13065-13084, 1986

Mattie, M.G., D.E. Lichy, R.C. Beal,”Seasat detection of waves, currents, and inlet discharge,” Int. J. Remote Sens., 1, 377-398, 1980.

McCowan, J., “On the solitary wave,” Philos. Mag. J. Sci., **32**, 45-58, 1891.

Miche. R., “Mouvements ondulatoires des mer en profondeur constant ou decroissante,” Ser. 3, Issue 363, 1954.

Monaldo, F.M., D.R. Lyzenga, “On the estimation of wave slope and height-variance spectra from SAR imagery,” IEEE Trans. Geosci. Remote Sens., **GE-24**, 542-551, 1986.

O’Dea, A., M. Haller, G. Wilson, “Sea surface roughness changes induced by rip currents and nearshore eddies,” submitted to J. Geophys. Res. Oceans, 2022.

Phillips, O.M., “On the response of short ocean wave components at a fixed wave number to ocean current variations,” J. Phys. Oceanogr., 14, 1425-1433, 1984

Phillips, O.M., “Radar returns from the sea surface – Bragg scattering and breaking waves,” J. Phys. Oceanogr., 18, 1065-1074, 1988.

Pierson, W.J., L. Moskowitz,” A proposed spectral form for fully developed wind sea based on similarity theory of S.A. Kitaigorodskii,” J. Geophys., Res., 69, 5181-5190, 1964.

Plant, W.J., J.W. Wright, “Growth and equilibrium of short gravity waves in a wind-wave tank,” J. Fluid Mech., **82**, 767-793, 1977.

Plant, W.J. “A two-scale model of short wind-generated waves and scatterometry,” J. Geophy. Res., 91, C9, m10735-10749, 1986.

Plant, W.J.,” A stochastic, multiscale model of microwave backscatter from the ocean,” J. Geophys. Res., 107, C9, 2130, 2002

Rascle, N., B. Chapron, A. Ponte, F. Ardhuin, P. Klein, “Surface roughness imaging of currents shows divergence and strain in wind direction.” J. Physical Oceanogr., 44, 2153-2163, 2014.

Romeiser R., W. Alpers, V. Wismann, “An improved composite surface model for the radar backscattering cross section of the ocean surface; 1. Theory of the model and optimization/validation by scatterometer data,” J. Geophys. Res., **102,** 25237-25250, 1997.

Synder, R.L., F.W. Dobson, J.A. Elliot, R.B. Long,”Array measurements of atmospheric pressure fluctuations above surface gravity waves,” J. Fluid. Mech., 102, 1-59, 1981.

SWAN Team, SWAN Technical Documentation, Delft University of Technology, 2007

Thompson, D.R., “Calculation of radar backscatter modulations from internal waves, ,” J. Geophys. Res., 93, C10, 1988.

Thornton, E.B., R.T. Guza, “Transformation of wave height distribution,” J. Geophy. Res., **88**, 5925-2938, July 1983.

Unal, C.M.H., P. Snoeij, P.J.F. Swart, “The polarization-dependent relation between radar backscatter from the ocean surface and surface wind vector at frequencies between 1 and 18 GHz,” IEEE Trans. Geosci. Remote Sens., **29**, 621-626, 1991.

Valenzuela, G.R., 1978: Theories for the interaction of electromagnetic and oceanic waves – a review, *Boundary-Layer Meteorology*, **13**, 61-85

Verhoef, A., M. Portabella, A. Stoffelen, H. Hersbach," CMOD5.n – the CMOD5 GMF for neutral winds," Technical Note SAF/OSI/CDOP/KNMI/TEC/TN/165, EUMENSAT, May 2008.

Verspeek, J., A. Stoffelen," CMOD7", Technical Note SAF/OSI/CDOP2/KNMI/TEC/RP/237, Royal Netherland Meteorological Institute (KNMI), Nov. 2015.

Vesecky, J.F., and R.H. Stewart, "The observation of ocean surface phenomena using imagery from the Seasat synthetic aperture radar: An assessment," J. Geophy. Res., 87, 3397-3430, 1982.

Wackerman C.C., P.Clemente-Colon, W.G. Pichel, X. Li, "A two-scale model to predict C-band VV and HH normalized radar cross section ofver the ocean," Can. J. Remote Sens., 28, no. 3, 367-384, 2002.

Wackerman, C. "Reconstruction of wave fields from SAR imagery: linear wave theory, non-linear SAR, non-linear RCS," NRL Technical Report: Revision 1, 01 July 2021.

Wright, J.W., 1968: A new model for sea clutter, *IEEE Trans. Antennas and Propagation.*, **AP-16**, 217-223

Wu, J., "Sea-surface slope and equilibrium wind-wave spectra," Phys. Fluids, 15, 741-747, 1972

Wu, J., "Mean squared slopes of the wind-disturbed water surface, their magnitude, directionality, and composition," Radio Sci., 25, 37-48, 1990.

Zurk, L.M. and W.J. Plant, "Comparison of actual and simulated synthetic aperture radar image spectra of ocean waves," J. Geophys. Res., **101**, 8913-8931, 1996.